LBNL-42589

Ernest Orlando Lawrence Berkeley National Laboratory

Fourier Transform Photoelectron Diffraction and Its Application to Molecular Orbitals and Surface Structure

Xin Zhou

Advanced Light Source Division

December 1998

Ph.D. Thesis

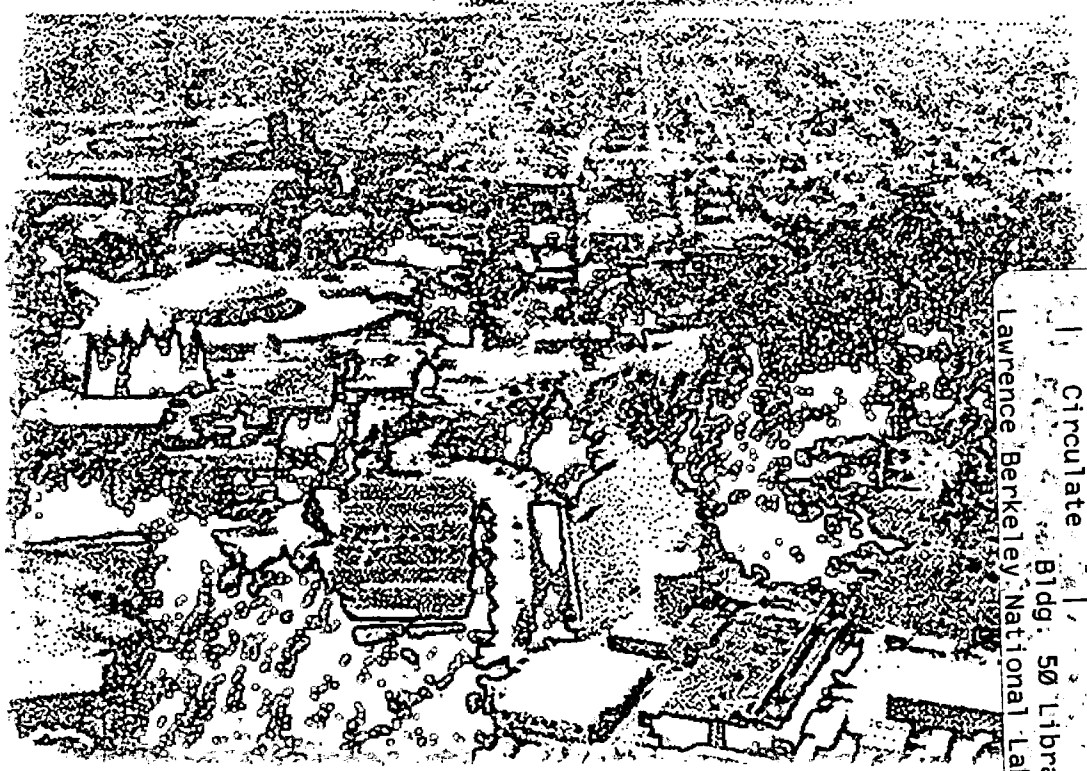

REFERENCE COPY
Does Not
Circulate
Bldg. 50 Library - Ref.
Lawrence Berkeley National Laboratory
Copy 1
LBNL-42589

DISCLAIMER

This document was prepared as an account of work sponsored by the United States Government. While this document is believed to contain correct information, neither the United States Government nor any agency thereof, nor the Regents of the University of California, nor any of their employees, makes any warranty, express or implied, or assumes any legal responsibility for the accuracy, completeness, or usefulness of any information, apparatus, product, or process disclosed, or represents that its use would not infringe privately owned rights. Reference herein to any specific commercial product, process, or service by its trade name, trademark, manufacturer, or otherwise, does not necessarily constitute or imply its endorsement, recommendation, or favoring by the United States Government or any agency thereof, or the Regents of the University of California. The views and opinions of authors expressed herein do not necessarily state or reflect those of the United States Government or any agency thereof or the Regents of the University of California.

LBNL-42589

FOURIER TRANSFORM PHOTOELECTRON DIFFRACTION AND ITS APPLICATION TO MOLECULAR ORBITALS AND SURFACE STRUCTURE

Xin Zhou
Ph.D. Thesis

Department of Physics
The Pennsylvania State University

and

Advanced Light Source
Lawrence Berkeley National Laboratory
University of California
Berkeley, CA 94720

December 1998

This work was supported by the Director, Office of Energy Research, Office of Basic Energy Sciences, of the U.S. Department of Energy under Contract No. DE-AC03-76SF00098.

The Pennsylvania State University

The Graduate School

Eberly College of Science

FOURIER TRANSFORM PHOTOELECTRON DIFFRACTION AND ITS APPLICATION TO MOLECULAR ORBITALS AND SURFACE STRUCTURE

A Thesis in

Physics

by

Xin Zhou

Copyright 1998 Xin Zhou

Submitted in Partial Fulfillment
of the Requirements
for the degree of

Doctor of Philosophy

December 1998

Abstract

Photoemission intensities from the molecular orbitals of c(2×2)CO/Pt(111) over a wide photon energy range were measured and analyzed by the same methods developed for structural studies using core levels. The 4σ orbital center of gravity is found to be concentrated between the C and O atoms, while that of the 5σ orbital lies between the C atom and the Pt surface. The C 1s photoelectron diffraction was used to determine the adsorption geometry.

The earlier ambiguity that multiple scattering is needed to correctly model a χ curve while single scattering is sufficient for understanding major peaks in the ARPEFS-FTs is clarified by studying the clean Ni(111) surface. In the normal emission case, several different combinations of scattering events have similar path length differences (PLDs), and can either cancel each other or enhance the corresponding FT peak. In the off-normal case the degeneracy is greatly reduced due to the lower degree of symmetry. In normal emission ARPEFS, up to third order multiple scattering is needed to describe fully both the χ curve and its FT spectrum.

To improve the spectral resolution in the ARPEFS-FT analysis, several new spectral analysis methods are introduced. With both autocorrelation autoregression (ACAR) and autocorrelation eigenvector (ACE), we can produce a reliable power spectrum by following the order-closing procedure. The best spectra are usually obtained when the autocorrelation sequence is computed with lags up to half the data range.

A simple way of determining surface adsorption sites is proposed as follows: First use a single scattering cluster for possible adsorption sites to construct the geometrical PLDs from the strong backscattering events; then compare these PLDs with those obtained from the ARPEFS-FT analysis of the experimental data. After the preferred adsorption site is determined, fine tune the interlayer distances according to the positional R-factor.

Table of Contents

List of Figures viii

List of Tables xi

Acknowledgements xii

Chapter 1. Introduction 1

References 3

Chapter 2. Bond Lengths and Molecular Orbitals of CO on the Pt(111) Surface 5

Abstract 5

I. Introduction 5

II. Experiment 7

III. Geometric structure 9

IV. The 4σ and $5\sigma+1\pi$ molecular orbitals 12

Conclusion 15

Acknowledgements 15

References 23

Chapter 3. An Angle-Resolved Photoemission Extended Fine Structure Study of the Clean Ni(111) Surface 28

Abstract 28

I. Introduction 28

II. Experiment 30

III. Data analysis 30

IV. Fourier analysis 32

A Ni 3p normal emission 32

B Ni 3s normal emission 33

C More refinements 34

V. Conclusion 36

Acknowledgements 37

References 38

Chapter 4. Modern Spectral Analysis of Angle-Resolved Photoemission Extended Fine Structure 52

Abstract 52

I. Introduction 52

II. Basic concepts and relations in modern spectral analysis 53

III. Comparison of implemented methods 59

Acknowledgements 63

References 66

Chapter 5. Simple Surface Structure Determination by Angle-Resolved Photoemission Extended Fine Structure - Fourier Transform Using Modern Spectral Analysis Techniques 67

I. Introduction 67

II. The physical basis of the FT method 69

A Off-normal emission 70

B Normal emission 71

III. The procedure of appying the FT method 72

IV. Discussion and conclusions 74

Acknowledgements 75

References 76

Chapter 6. Conclusions 94

Appendix A. Applied Materials Chamber 98

References 99

Appendix B. Source Code for Calculating the Voigt Function and the Shirley Background 101

I. Introduction 101

II. Voigt.h 101

III. Voigt.cpp 101

References 104

List of Figures

FIG. 1.1 Single scattering cluster approximation of photoelectron diffraction. $A_j(k)$ is a slow-varying function that includes transition matrix element, various attenuation effects, etc. $\phi_j(k)$ is the electron-atom scattering phase shift that is also slow-varying. Schematic: courtesy of S.A. Kellar. 4

FIG. 2.1 Surface pattern of c(4×2) CO/Pt(111). Here black circles stand for CO with C closer to Pt and O out, white circles stand for Pt on the (111) surface. 16

FIG. 2.2 Best fit of the C 1s normal emisson χ curve. The units of the horizontal axis are $Å^{-1}$ in top panel, and Å in the bottom panel. 17

FIG. 2.3 photoemssion spectrum of the valence electrons of CO/Pt(111). 18

FIG. 2.4 Top panel shows the best fit of CO 4σ molecular orbital normal emisson χ curves, achieved by optimizing coeffients of atomic orbitals according to the R-factor. Bottom panel shows their FTs. 19

FIG. 2.5 Best fit of CO 5σ molecular orbital normal emisson χ curve and their FTs. 20

FIG. 2.6 FT peaks of experimental χ curves lined up against the atoms in real space. 21

FIG. 2.7 The contour plots of the molecular orbitals obtained through the best fits. The top panel shows the 4σ orbital, and the bottom panel the 5σ orbital. 22

FIG. 3.1 The top panel shows a unit cell of fcc Ni. The bottom panel shows a top view in the [111] direction. Atoms are labeled A,B,C and D to identify atomic layers. 40

FIG. 3.2 Ni crystal in a perspective view in the top panel, and again in a top view in the [111] direction in the bottom panel. 41

FIG. 3.3 Top panel shows a synchrotron X-ray photoemission spectrum of Ni 3s and 3p peaks and satellites. Bottom panel shows Ni3d band and satellite. 42

FIG. 3.4 Ni 3s ARPEFS in normal and off-normal emission geometries with best fits... 43

FIG. 3.5 Ni 3p ARPEFS in normal and off-normal emission geometries with best fits. . 44

FIG. 3.6 FT of Ni 3p normal emission χ curves calculated with model clusters of increasing sizes. Only top layer atoms are emitters, and only single scattering is considered, except that the last panel shows the FT of the experimental data. 45

FIG. 3.7 FT of Ni 3s normal emission χ curves calculated with model clusters of increasing sizes, as in Fig. 3.6. 46

FIG. 3.8 FT of Ni 3p χ curves calculated with increasing emission angles. The model cluster consists of (13+3) atoms, ie. 13 atoms on the top layer and 3 atoms on the second layer of the [111] surface. 47

FIG. 3.9 Simplified geometry for our model calculation in Fig. 3.8, where δ is the varied angle from 0° to 5°, and θ the fixed angle between the surface normal direction and a certain scatterer-emitter direction. 48

FIG. 3.10 Double scattering reduces the peak around 8.2Å. The cluster used here has 104 atoms in 5 layers. 49

FIG. 3.11 Ni3d valence band normal emission ARPEFS and FT. 50

FIG. 3.12 Ni3d satellite normal emission ARPEFS and FT. 51

FIG. 4.1 Flow Chart comparing four modern spectral analysis methods. 64

FIG. 4.2 Power spectral density functions of P 2s ARPEFS. The sample is *c*(2×2)P/Fe(100), with emission angle 45° off-normal along the [011] direction. The various spectral analysis methods show varying degrees of resolution. The x-axis is Path Length Difference (PLD) in Å. 65

FIG. 5.1 c(2×2)S/Ni(001) off-normal emission ARPEFS-FT. 83

FIG. 5.2 p(2×2)S/Cu(001) off-normal emission ARPEFS-FT. 84

FIG. 5.3 c(2×2)Cl/Cu(001) off-normal emission ARPEFS-FT. 85

FIG. 5.4 c(2×2)P/Fe(001) off-normal emission ARPEFS-FT. 86

FIG. 5.5 c(2×2)S/Cr(001) off-normal emission ARPEFS-FT. 87

FIG. 5.6 Normal emission ARPEFS of c(2×2)S/Ni(001). 88

FIG. 5.7 c(2×2)S/Ni(001) normal emission ARPEFS-FT. 89

FIG. 5.8 p(2×2)S/Cu(001) normal emission ARPEFS-FT. 90

FIG. 5.9 c(2×2)Cl/Cu(001) normal emission ARPEFS-FT. 91

FIG. 5.10 c(2×2)P/Fe(001) normal emission ARPEFS-FT. 92

FIG. 5.11 c(2×2)S/Cr(001) normal emission ARPEFS-FT. 93

FIG. A.1 Applied Materials Chamber 100

List of Tables

Table 3.1 Path length differences (PLD) for clean Ni(111) in normal emission geometry. 39

Table 5.1 Experimental and calculated PLDs in the off-normal emission ARPEFS-FTs. 80

Table 5.2 Experimental and calculated PLDs in the normal emission ARPEFS-FTs 81

Table 5.3 Interplanar distances between the adsorbate layer and the substrate layers 82

Acknowledgements

From Happy Valley to Wildcat Canyon, Professor David Shirley has provided me indispensable guidance about science and invaluable words of truth about life. I can not imagine a better advisor, and I feel extremely lucky to have had Dave's advice.

The first person I want to thank at PennState is Ginny Imboden, whose effective handling of administrative matters made my graduate school experiance much easier. Zhang Chao, Lu Zhou, Xie Chen, and Agni Mitra, all shared enjoyable moments with me at State College. I am sure I will drive a U-Haul with Gao Lei trailing me again.

At Berkeley, Zahid Hussain is simply the best. His enthusiasm infects everybody, and his attention to experimental details profoundly educated me. Scot Kellar taught me everything about pumping and tightening UHV chambers. Eddie Moler revealed for me the secrets of data reduction. Chen Yufeng is a most versatile programmer and he patiently showed me a lot of the intricacies of his diffraction code. Tony Huff's thesis was the most helpful for me to understand Beamline 9.3.2. They all helped me take data. Wu Huasheng explained very clearly the physics of photoelectron holography to me. Barry Petersen warned me early on about all the possible future pitfalls, of which I eventually managed to fall into each and every one. Many other people at the Berkeley Lab helped me with the experiments or the equipment, especially Zhou Xingjiang, Vera Zhuang, M.Zahid Hasan, Jae K. Lee, Noel Kellogg, Dennis Hull, Bruce Rude, Frank Zucca, Neal

Hartman, and Greg Andronaco. Mike Press taught me a lot about circuit boards as well as the methodical approach of a good engineer. John Spring wasted many hours chatting with me. Scott Locklin helped proofread the thesis. Thanks, guys!

My parents have always loved me unconditionally. As their only child, I realize that my wellbeing has become their ultimate source of happiness. I promise to myself that I won't let them down.

I dedicate this Thesis to my wife, Wang Jue.

Chapter 1. Introduction

Photoelectron diffraction as a surface structural probe actually started before 1978, which is generally recognized as the year when three groups independently demonstrated the phenomenon with core level photoelectrons in either the angle-scan or the energy-scan mode. When Liebsch predicted the diffraction effect in 1974 [1], he proposed the use of valence electrons. In 1976, Apai *et al* [2] accomplished a beautiful experiment on CO/Pt(111), and solved the mystery of CO orientation on the Pt surface by doing what Davenport [3] and Liebsch had suggested: measuring the molecular orbital (MO) photoemission intensity and looking for its angular dependence due to the diffraction effect. The energy dependence of the MO photoemission from the same system was also observed and reported a year later. However, the MO ground state of a molecule adsorbed on a metal surface is a mystery in itself, and people did not understand the relevant electron scattering process very well. Naturally attention was shifted away toward the core level photoelectron experiments, because core orbitals are much easier to handle in a theoretical treatment. Core level photoelectron diffraction theory has flourished ever since, generating more interest in experimental activities. A simplified version of the cluster model is shown is Fig. 1.1.

Now history repeats itself. Chapter 2 reports a new experiment on the MOs of CO/Pt(111) done at the Advanced Light Source, Beamline 9.3.2. Thanks to the superior performance of this third generation synchrotron x-ray source, we were able to collect photoemission data over a wide photon energy range for the 4σ and $5\sigma+1\pi$ orbitals.

Since much of the diffraction theory has been developed, we can now study the properties of the MO ground state by measuring the photoelectron final state with our electron analyzer. The main analysis method we use here is the Fourier transform (FT) of our angle-resolved photoemission extended fine structure (ARPEFS) data, as the FT peak positions are directly related to physical distances on the surface.

Another direction in which we push the limit of existing techniques is the study of core level photoelectron diffraction from more complicated systems. Most of the early ARPEFS experiments were done on adsorbate systems, using the s initial state core electron of an adatom. Later, people studied systems of p, d and f initial states and the their satellites, and systems with metal-metal interface. We have studied Ni 3s, 3p, and 3d electrons from a pure Ni(111) sample, a great challenge for the existing theoretical framework, which was developed with adsorbate system in mind. Chapter 3 details our findings, especially our current new understanding of the ARPEFS-FT peaks, from this system of many layers of identical emitters and densely packed scatterers.

To further understand the FT peaks, we need a better tool than the plain "taper-and-transform". Chapter 4 introduces several of modern spectral analysis methods, which have already been used by scientists and engineers in other fields for decades. We find that the autocorrelation autoregression (ACAR) or the autocorrelation eigenvector (ACE) algorithm produces much better resolution and is less liable to produce spurious peaks, than direct FT, while it remains stable through a substantial range of the input parameters.

The next chapter basically applies our newfound technique to the FT analysis of ten sets of experimental ARPEFS data collected in our group over the years, and proposes a simple way of determining surface atomic structures. This approach requires fewer data points than photoelectron holography, and yet may give fairly accurate results without doing any full-fledged multiple-scattering calculations.

The concluding chapter reviews what I have accomplished in my thesis research, and offers my opinion on the current status and the future development of photoelectron diffraction.

REFERENCES

1. Ansgar Liebsch, Phys. Rev. Lett. **32**, 1203 (1974).
2. G. Apai, P.S. Wehner, R.S. Williams, J. Stöhr, and D.A. Shirley, Phys. Rev. Lett. **37**, 1497 (1976).
3. J.W. Davenport, Phys. Rev. Lett. **36**, 945 (1976).

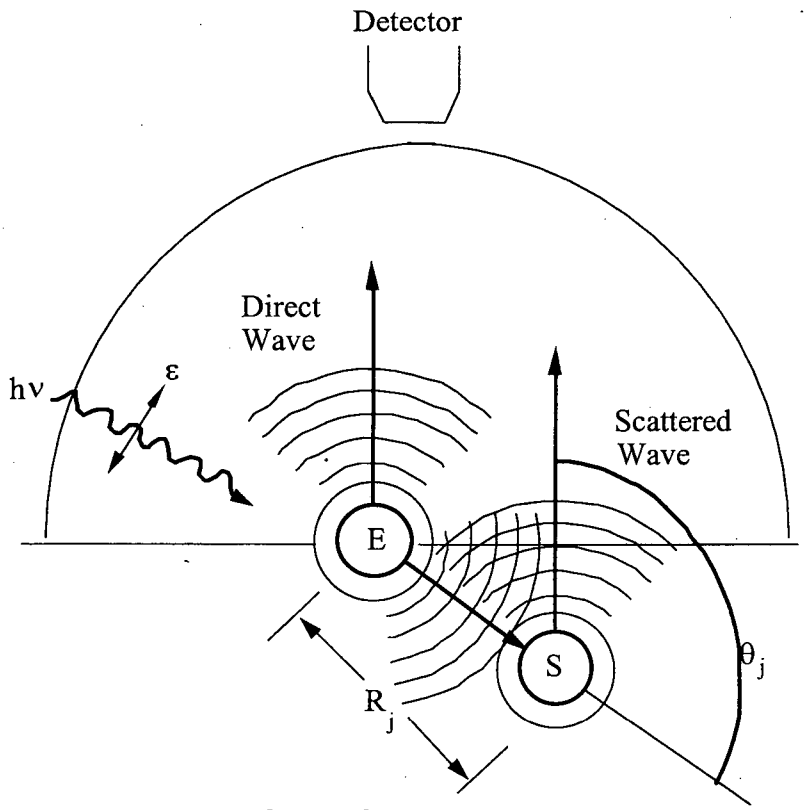

$$\chi(k) = \frac{I - I_0}{I_0} = \frac{(\psi_0 + \psi_S)^2 - \psi_0^{\,2}}{\psi_0^{\,2}} = 2\,\mathrm{Re}(\frac{\psi_S}{\psi_0})$$

$$= \sum_j A_j(k)\cos[kR_j(1-\cos\theta_j) + \phi_j(k)]$$

FIG. 1.1 Single scattering cluster approximation of photoelectron diffraction. $A_j(k)$ is a slow-varying function that includes transition matrix element, various attenuation effects, etc. $\phi_j(k)$ is the electron-atom scattering phase shift that is also slow-varying. Schematic: courtesy of S.A. Kellar.

Chapter 2. Bond Lengths and Molecular Orbitals of CO on the Pt(111) Surface

ABSTRACT

Large intensity oscillations with energy were observed for photoelectrons emitted in the normal direction from the 4σ and $5\sigma+1\pi$ molecular orbitals of CO adsorbed on a Pt(111) surface. The molecular orbital photoemission intensity variations over a wide energy range are interpreted by the same methods developed for structural studies using core levels, i.e. Angle-Resolved Photoemission Extended Fine Structure, yielding effective mean positions for the molecular orbital electron distributions. With Fourier transform analysis, the mean position of the 4σ orbital is found to lie mainly between the carbon and oxygen atom, while that of the 5σ orbital falls between the carbon atom and the platinum atom, contributing to the chemisorption bond. The diffraction pattern of the C 1s photoelectrons was used to confirm the adsorbate structure in c(4×2)CO/Pt(111) and the carbon-platinum interplanar distance is found to be 1.828Å at the top site and 1.452Å at the bridge site, translating to a bond length of 2.008Å.

I. INTRODUCTION

Carbon monoxide chemisorbed on a platinum surface has been an intensely studied system for many years [1]. Besides the applied aspects of this system, e.g. catalytic oxidation [2,3], it is an ideal prototype for studying the nature of the surface chemical

bond [4], adsorption [5,6] and desorption [7], also such fascinating topics as phase transitions [8], site conversion [9], lateral interactions [10]. Froitzheim, Hopster, Ibach and Lehwald [11] were the first to correctly identify the adsorption sites of half coverage c(4×2)CO on Pt(111) to be half-top and half-bridge-site using electron energy loss spectroscopy (EELS), and their results were quickly confirmed by Krebs and Lüth [12] with infrared reflection absorption spectroscopy (IRAS). The upright orientation of CO molecules on the Pt(111) surface with oxygen out was established by an angle-resolved photoemission experiment [13] combined with Davenport's calculation [14] of the angular dependence of the CO photoemission cross section. Until recently, the only published results on the distances between the carbon atoms and the platinum surface at those two different adsorption sites were obtained in a low energy electron diffraction (LEED) experiment by Ogletree, Van Hove and Somorjai [15]. This information is very important to the theoretical investigation of CO adsorption energy, vibration frequency and electronic properties.

Photoelectron diffraction is a very powerful tool to determine the geometry of solid surfaces [16,17]. We present here our Angle-Resolved Photoelectron Extended Fine Structure (ARPEFS) [18] results on the carbon-platinum distances at both adsorption sites, using carbon 1s photoelectron peaks in our spectra. Every ARPEFS curve is reduced from a series of photoemission spectra, with each spectrum taken with photon energies chosen to provide equal steps in terms of the photoelectron wavevector.

Once we have determined the geometry of the atoms in the c(4×2)CO/Pt(111) adsorbate system, we ask the further question: what is the geometry of the bond; in other words, where do the electrons come from when we are looking at a particular molecular orbital peak in a photoemission spectrum? For this, we apply the same ARPEFS technique to the valence orbital peaks instead of the carbon 1s core level, and take advantage of its unique capability of interpreting the Fourier transform peaks in real space as the path length differences (PLD) of the scattering electrons. The molecular orbitals of free CO were calculated and depicted by Jorgensen and Salem [19], and by Johnson and Klemperer [20], but the wavefunctions for this adsorbate system have not been explicitly plotted out, except for some simple sketches similar to those given by Rhodin and Gadzuk [21]. The discrepancy between recent theoretical calculations of the chemisorption energy also reveals the difficulty of correctly modeling molecules on a metal surface. Earlier efforts of X-ray or ultraviolet photoelectron spectroscopy (XPS or UPS) concentrated on the photoemission peak position or cross-section [22,23]. The recent work of X-ray emission spectroscopy (XES) by Nilsson *et al* [24,25] provids another way to study surface chemical bonds. Our photoelectron diffraction technique is totally independent of XES and thus affords us a different way of approaching this problem.

II. EXPERIMENT

The experiment was performed in an ultra-high vacuum chamber (base pressure 3×10^{-10} torr), equipped with a PHI hemispherical electron energy analyzer and a liquid-nitrogen-cooled 5-degrees-of-freedom sample manipulator, on beamline 9.3.2 at the Advanced

Light Source of Lawrence Berkeley National Laboratory [26]. The platinum crystal was previously carefully prepared by oxygen roasting and argon ion sputtering procedures monitored by STM and XPS in a separate study [27], and was easily cleaned during this experiment by sputtering and annealing cycles. The surface cleanliness and order were periodically checked with synchrotron XPS and LEED. The CO gas was introduced into the chamber by a gas doser regulated by a leak valve. Various dosing and cooling sequences were practiced according to the literature [28], and we were able to consistently reproduce the desired c(4×2) LEED pattern by backfilling the chamber at room temperature with CO at 1×10^{-6} torr for 10 seconds followed by simultaneous pumping and cooling down to experimental conditions. The sample surface temperature was kept at 110K throughout the data collection. The photon polarization vector was oriented 30° from the electron analyzer direction, which was also the sample surface normal. The total experimental energy resolution, including photon monochromator resolution and electron analyzer resolution, was ~ 0.9 eV and it varied in a 20% range as photon energy changed. Each C1s core-level spectrum was fitted with a Voigt peak, an inelastic tail represented by an integration of the Voigt, and a smooth background. The intensity I of the peak is the Voigt area normalized against the background. The position of the peak in photoelectron kinetic energy was converted to wavevector k. Thus we obtained the intensity curve $I(k)$ of our ARPEFS experiment. The intensity curve was then interpolated by a low-order polynomial to obtain a rather featureless background $I_0(k)$. Finally the coveted χ curve is given as

$$\chi(k) = \frac{I(k) - I_0(k)}{I_0(k)}.$$

For valence spectra, we first fix an energy range relative to the Fermi edge that encompasses both 4σ and 5σ+1π, then use Gaussians to fit the peaks, under which we fit a smooth background. In order to get high enough count rate we had to compromise the energy resolution of our spectrometer such that we did not resolve the 5σ and 1π. The Gaussian area was normalized against the photon flux measured by a gold grid upstream of our experimental chamber. Once the data were reduced to an intensity curve, the $\chi(k)$ curves for molecular orbitals were obtained the same way as for a core level. When we take a series of photoemission spectra in our ARPEFS experiment by changing the monochromator, we space the photon energies such that the final $\chi(k)$ consists of data points roughly evenly spaced in k. This facilitates further Fourier transform analysis [29].

III. GEOMETRIC STRUCTURE

The c(4×2) LEED pattern is also termed ($\sqrt{3} \times 2$)rect by Biberian and Van Hove [30]. An early misconception was that the information in this LEED pattern at half monolayer coverage alone would mandate a surface unit mesh the same as the currently accepted model for CO on Pt(111), i.e. the mesh formed with half bridge and half top site adsorption. In fact the LEED pattern only implies that 1/4 monolayer adsorbate forms a rectangular surface unit mesh with sides of $\sqrt{3} \times 2$ substrate unit, and the other 1/4 monolayer adsorbate can be anywhere inside the rectangle [31].

We computed the ARPEFS theoretical χ curves with a cluster-model multiple-scattering code [32,33] using the Rehr-Albers separable propagator [34], and the phase shifts for electrons scattering Pt atoms are calculated with FEFF 7.0 [35,36] which considers relativistic effects, important for heavy elements like Pt. The Pt lattice constant was fixed at 3.923Å. The C-O bond length was fixed at 1.130Å, as it should not be affected much by the platinum surface and since our C1s photoelectron scattering effects are not sensitive to the forward-positioned oxygen atoms in the fixed-angle-scanned-energy mode [37]. All symmetry-allowed adsorption sites were considered in the simulation and indeed the accepted model gives the smallest R-factor,

$$R = \frac{\sum(\chi_E - \chi_T)^2}{\sum \chi_E{}^2 + \chi_T{}^2},$$

where χ_E and χ_T are the experimental χ curve and the theoretical χ curve respectively. Upon minimization of the R-factor, the C-Pt interplanar distances were found to be 1.452Å ± 0.002Å at the bridge site and 1.828Å ± 0.001Å at the top site. The LEED result by Ogletree, Van Hove and Somojai gave the C-Pt interplanar distances of 1.85Å and 1.45Å at the top and bridge site respectively, compatible with our result.

Our statistical errors were estimated using a method described elsewhere [38]. The extremely small values of the statistical error in atomic positions are the same order of magnitude as the thermal vibrations of the atoms, which exemplifies the very high precision of ARPEFS in measuring atomic structures. However, other systematic errors dominate our overall accuracy. These errors are not unique to ARPEFS, but are indeed

associated with LEED and all other structural methods that depend on electron scattering. They are reviewed briefly below.

The primary source of error is the set of electron-scattering partial-wave phase shifts, which are calculated with a separate computer program before the photoelectron diffraction calculation. Although every effort has been made to increase the accuracy of the phase shifts we use, some physical processes are still disregarded or approximated in order for a practical calculation to be carried out. The first obvious pitfall for the phase shifts is that the muffin tin potential does not really model the surface very well, as we don't know the true inner potential of the muffin tin, and we cannot distinguish between a surface atom and a bulk atom. Secondly, the photoemitting atom has one extra hole: because of the screening effect, the real scattering process around the emitter can differ for each different atom. Once we obtain a phase shifts file, we introduce it into our photoelectron diffraction simulation code without subsequently being able to varying it. At the same time, every other parameter we use as input can be varied independently. Because the whole fitting process can be viewed as a variation method, the unvaried part of the theory becomes an ultimate source of systematic error. In Zheng, Hussain, and Shirley 's study [39] of the influence of phase shifts on the structural results, a range of 0.02Å difference could come from choosing differently computed phase shifts.

Other theoretical simplifications may also affect the final result. For example, the electron propagation attenuation is modeled with an inelastic mean free path. The thermal averaging effect is treated by a Debye-Waller factor. Neither accounts for the anisotropy involved in a real sample. There are also practical limitations imposed on any scientific

computing project, e.g. we have to stop at a certain expansion order of the Green's function, we have to stop at a certain multiple scattering order, we have to use a finite size for the atomic cluster, and of course, the experimental spectral data always have noise, and the data reduction procedure can always be reasonably varied to obtain a slightly different χ curve.

All things considered, even with an excellent fit to the data as depicted in Fig. 2.2, and the very high precision of ±0.001Å to ±0.002Å which this implies, systematic errors in the theoretical modeling, common to all electron-scattering methods, limit the ultimate accuracy to no better than ±0.01 – 0.02Å.

IV. THE 4σ AND 5σ+1π MOLECULAR ORBITALS

Interestingly the photoelectron diffraction effect in both the scanned-angle mode [40] and the scanned-energy mode [41] was first observed for valence electrons. When Plummer and Gustafsson promoted angle-resolved photoemission as a powerful tool for obtaining structural information of adsorbates, they had chemical bonds in mind [42]. However, it was core-level photoelectron diffraction that gained early acceptance as a structure-probing technique due to its relative ease of interpretation and simulation, and using it, many adsorbate geometric structures have been solved. Only recently have people attempted to venture beyond core-levels [43,44].

Our normal emission data in the form of an intensity ratio compare favorably with similar, but much more limited, measurements done over twenty years ago [41]. The molecular orbital χ curves oscillate by nearly 100%, much more than the C1s core-level χ curve. The Fourier transform of the 4σ χ curve shows predominantly one peak at 4.8Å, a larger path length difference than the main peak of C1s FT at 4.0Å, while the $5\sigma+1\pi$ FT shows predominantly one peak at 3.3Å, a smaller PLD than C1s FT. We also note this: even by simple visual inspection of the three χ curves, there is in each case one dominant periodicity, with frequencies in the order $4\sigma > 1s > 5\sigma+1\pi$.

Since half of the CO molecules adsorb directly on top of Pt atoms, which scatter much more strongly than the bridge-site Pt atoms in our normal emission experimental setup, the main FT peak in a χ curve should reflect the distance between the photoemission source and the top-site Pt atoms immediately underneath. Combining our past experience of Fourier Transforming core-level ARPEFS with the current FT of a χ curve from a chemical bonding orbital, we infer that the 4σ bond is located mainly between C and O atoms, and the $5\sigma+1\pi$ mostly between C atoms and the Pt surface. This picture is consistent with the Blyholder model [45] of chemisorption in which CO 5σ orbital interacts with metal valence states and CO $2\pi^*$ receives electron density through back-donation.

We note here that these results will be compared with recent X-ray emission spectroscopy work on similar samples by A. Nilsson et al, which was interpreted in a different way [25,46]. In their interpretation, the 4σ is described as being pulled inward

closer to the metal, while the 5σ orbital is pushed outward and more concentrated on the O atoms. An argument for "a balanced distribution of charge density" is presented. If we believe that FT peaks indicate locations of high electron density, our FT plots cannot be reconciled with their proposed picture. However, the two methods are not really comparable. ARPEFS studies photoelectrons from orbitals in the neutral ground state, while the X-ray emission originates from a highly excited 1s core-hole state.

Since there is no valence photoelectron diffraction computer code available, we used a linear combination of atomic orbitals (LCAO) model of the CO molecular orbitals and approximated the Pt valence band on a large surface with atomic levels of just one Pt atom. This atomic approach should give us qualitatively correct picture without doing a full band structure calculation or a large cluster model calculation [47,48,49]. We calculated separately the final state wavefunctions of diffracted photoelectrons from Pt 6s, Pt 6p, Pt 5d, C 2s, C 2p, O 2s and O 2p atomic orbitals, and linearly added together these wavefunctions to simulate the observed final state that originated from the true molecular orbitals. As the data points vastly outnumber the linear coefficients, solving this non-linear equation system implies minimizing some form of a merit function. We used the same data reduction process as for core-level photoemission to produce χ_E and χ_T, and varied the atomic orbital coefficients in our LCAO model to minimize the R-factor. Obviously this kind of coefficient determination is totally independent of any regular theoretical calculation of LCAO based on cluster models; thus it provides a good check against the *ab initio* approach. The prospect of using photoelectron diffraction from molecular orbitals to study chemical bonds in this way poses a challenge for

theoretical advances in seriously modeling the surface chemical bond, as well as photoemission from that bond.

CONCLUSION

We have demonstrated photoelectron diffraction from molecular orbitals. The C-Pt interplanar distances of c(4×2)CO/Pt(111) are precisely determined: 1.83Å at the top site and 1.45Å at the bridge site, with systematic uncertainties of ca. 0.01-0.02Å. The bond lengths are 1.83Å at the top site and 2.01Å at the bridge site. The 4σ orbital has a high electron density distribution between the C and O atoms, while the 5σ orbital has a high density between the C atom and the Pt surface. This experiment demonstrated the capability of photoelectron diffraction for studying the surface chemical bond.

ACKNOWLEDGEMENTS

We thank Dr. J.J. Rehr of University of Washington for generously providing platinum phase shifts calculated with the FEFF code, Dr. P.H.T. Philipsen of Vrije Universiteit, The Netherlands, for LCAO calculation of free CO molecule, Dr. A. McLean of Queen's University, Canada, for providing a fast algorithm for calculating Voigt function. This work was supported by the Director, Office of Energy Research, Office of Basic Energy Sciences of the U.S. Department of Energy under Contract No. DE-AC03-76SF00098.

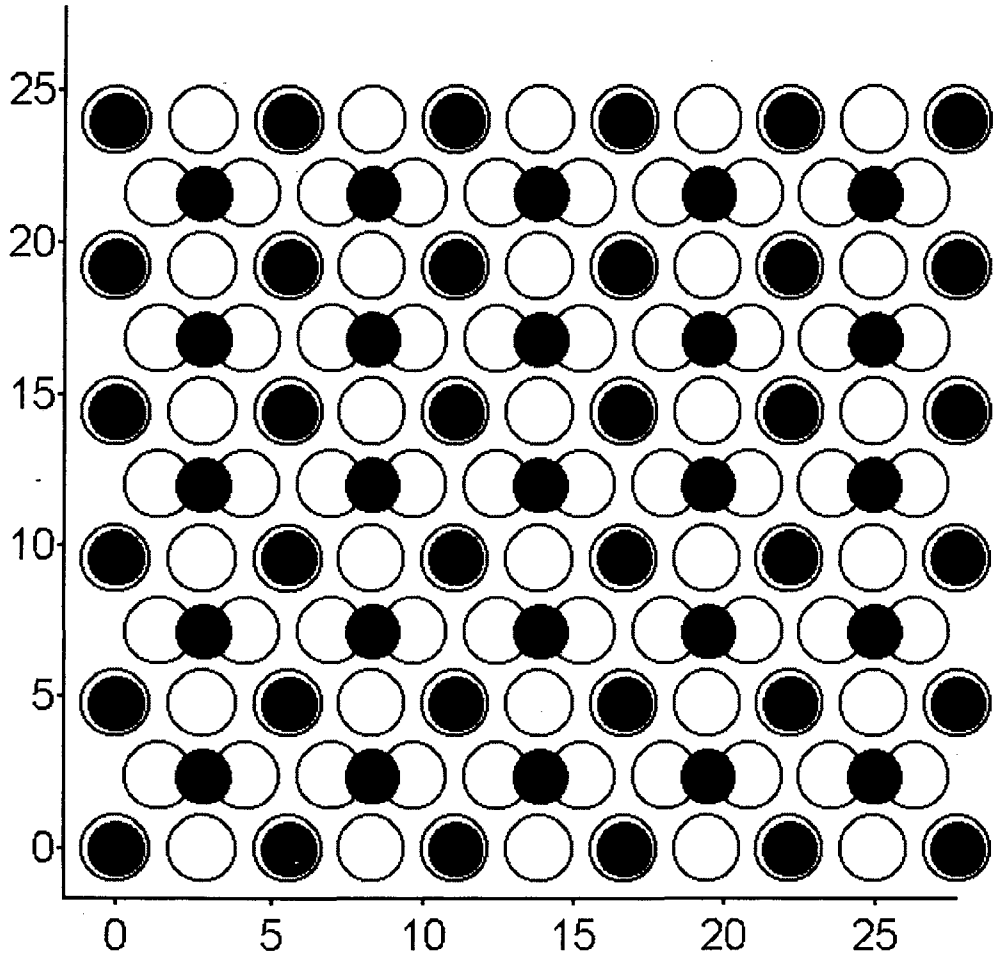

FIG. 2.1 Surface pattern of c(4×2) CO/Pt(111). Here black circles stand for CO with C closer to Pt and O out, white circles stand for Pt on the (111) surface.

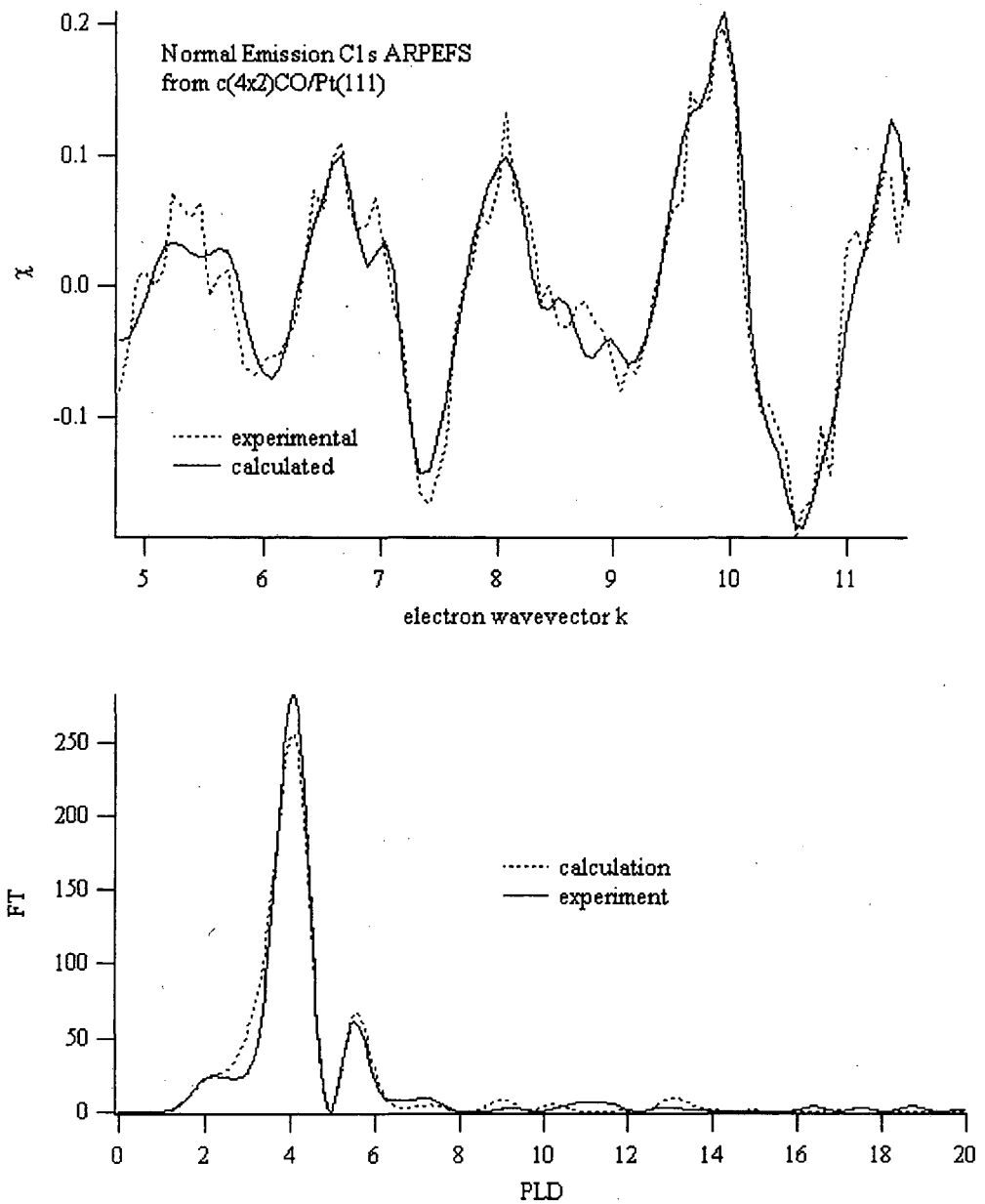

FIG. 2.2 Best fit of the C 1s normal emisson χ curve. The units of the horizontal axis are $Å^{-1}$ in top panel, and Å in the bottom panel.

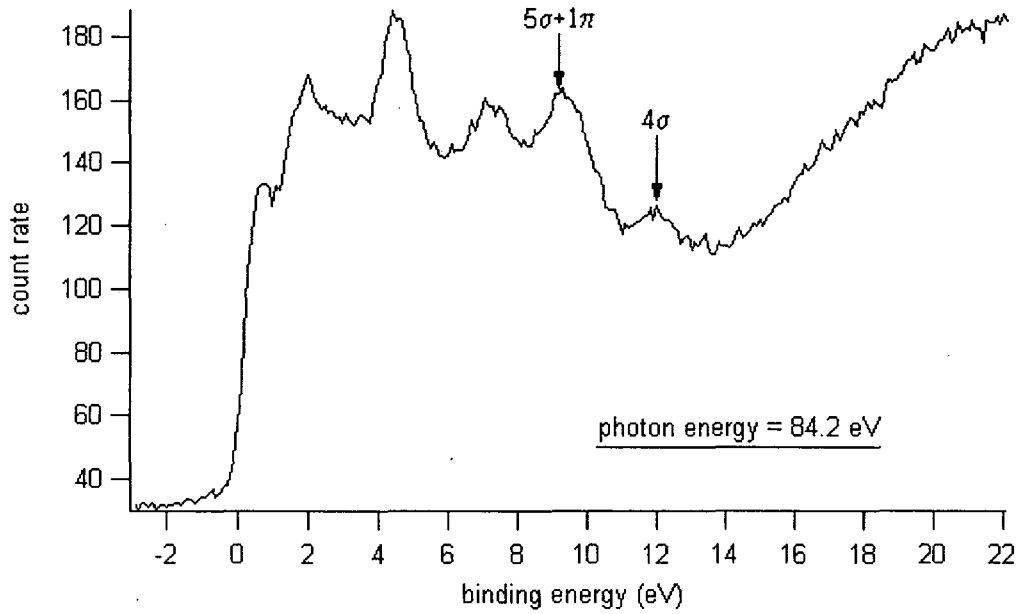

FIG. 2.3 photoemssion spectrum of the valence electrons of CO/Pt(111).

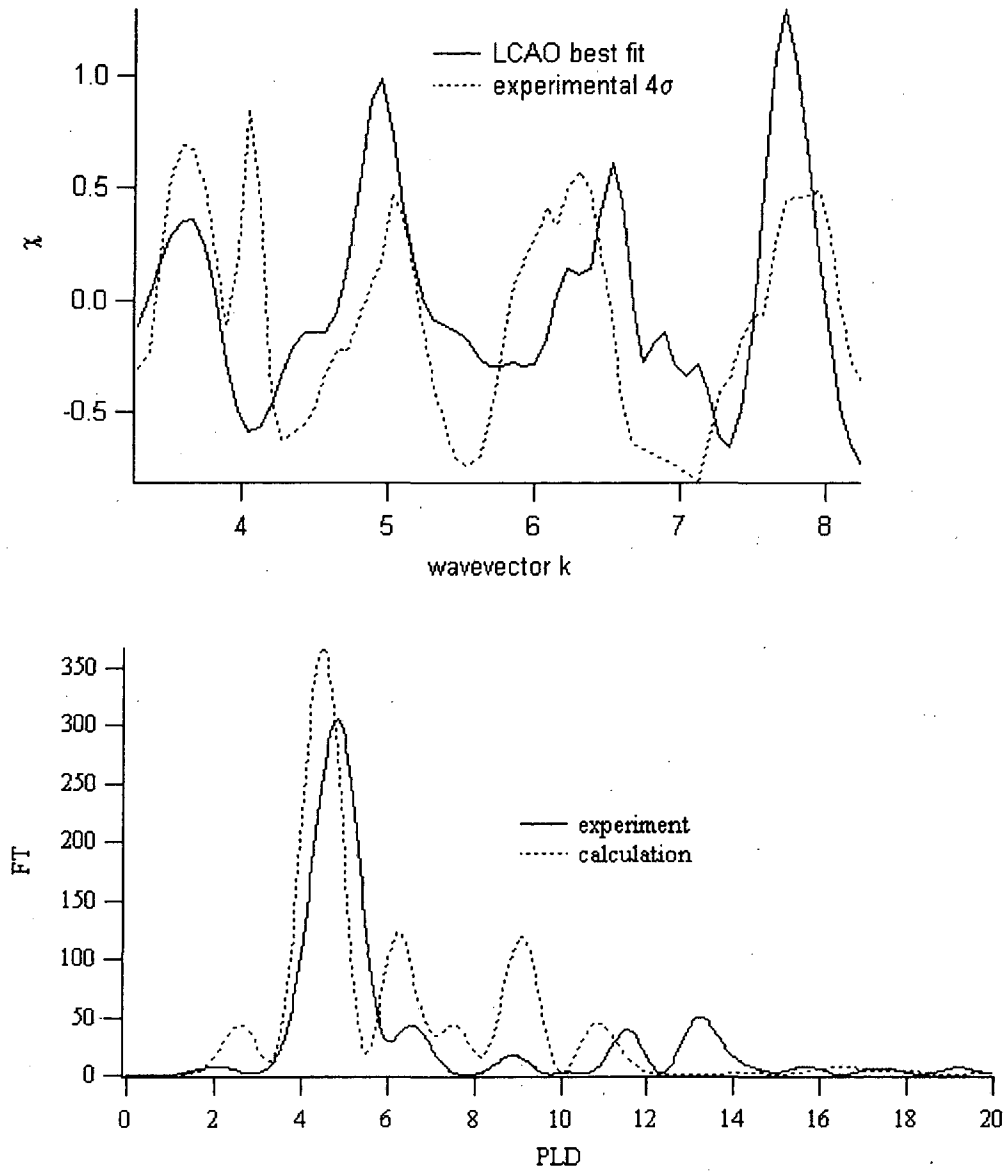

FIG. 2.4 Top panel shows the best fit of CO 4σ molecular orbital normal emisson χ curves, achieved by optimizing coeffients of atomic orbitals according to the R-factor. Bottom panel shows their FTs.

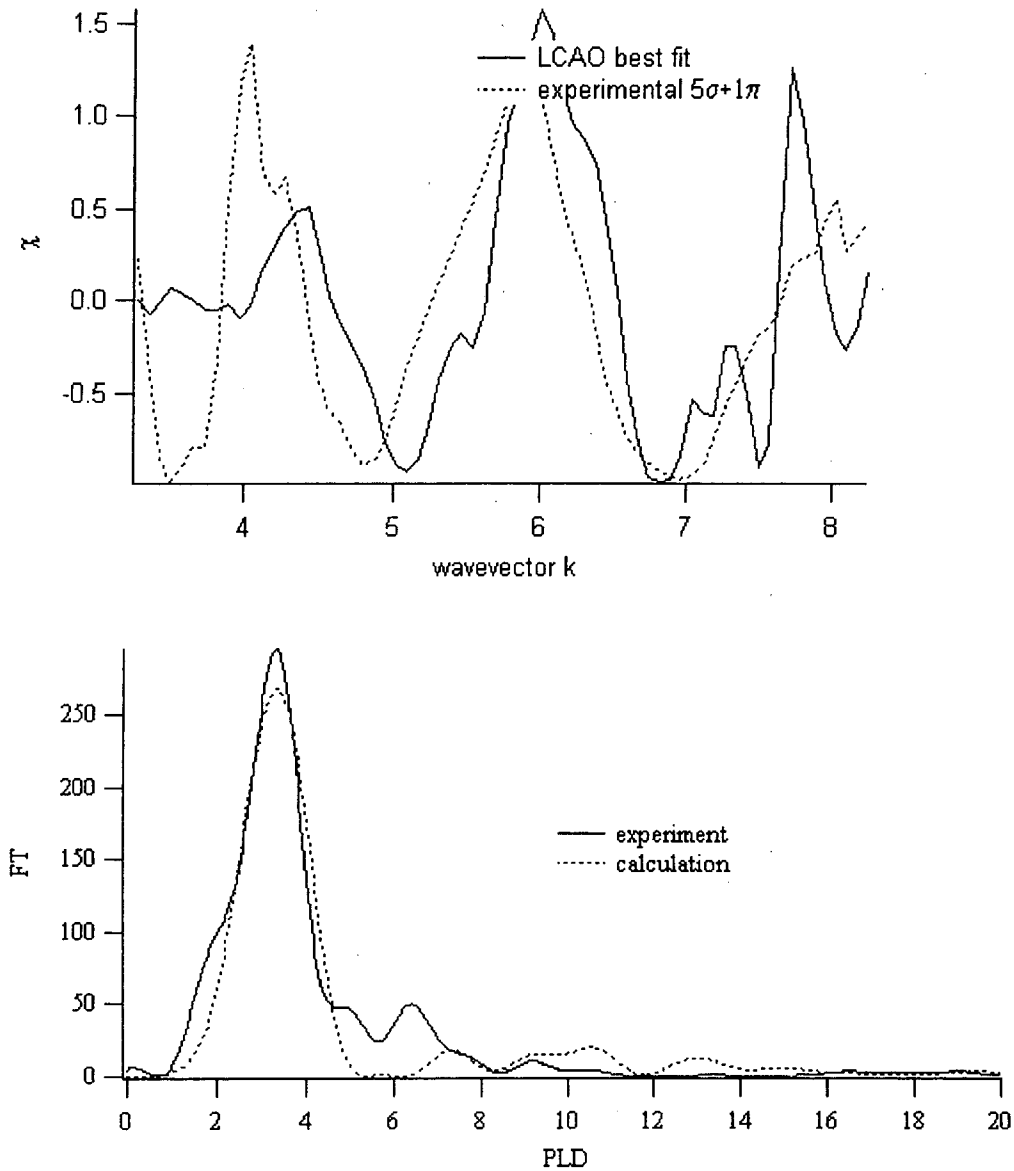

FIG. 2.5 Best fit of CO 5σ molecular orbital normal emisson χ curve and their FTs.

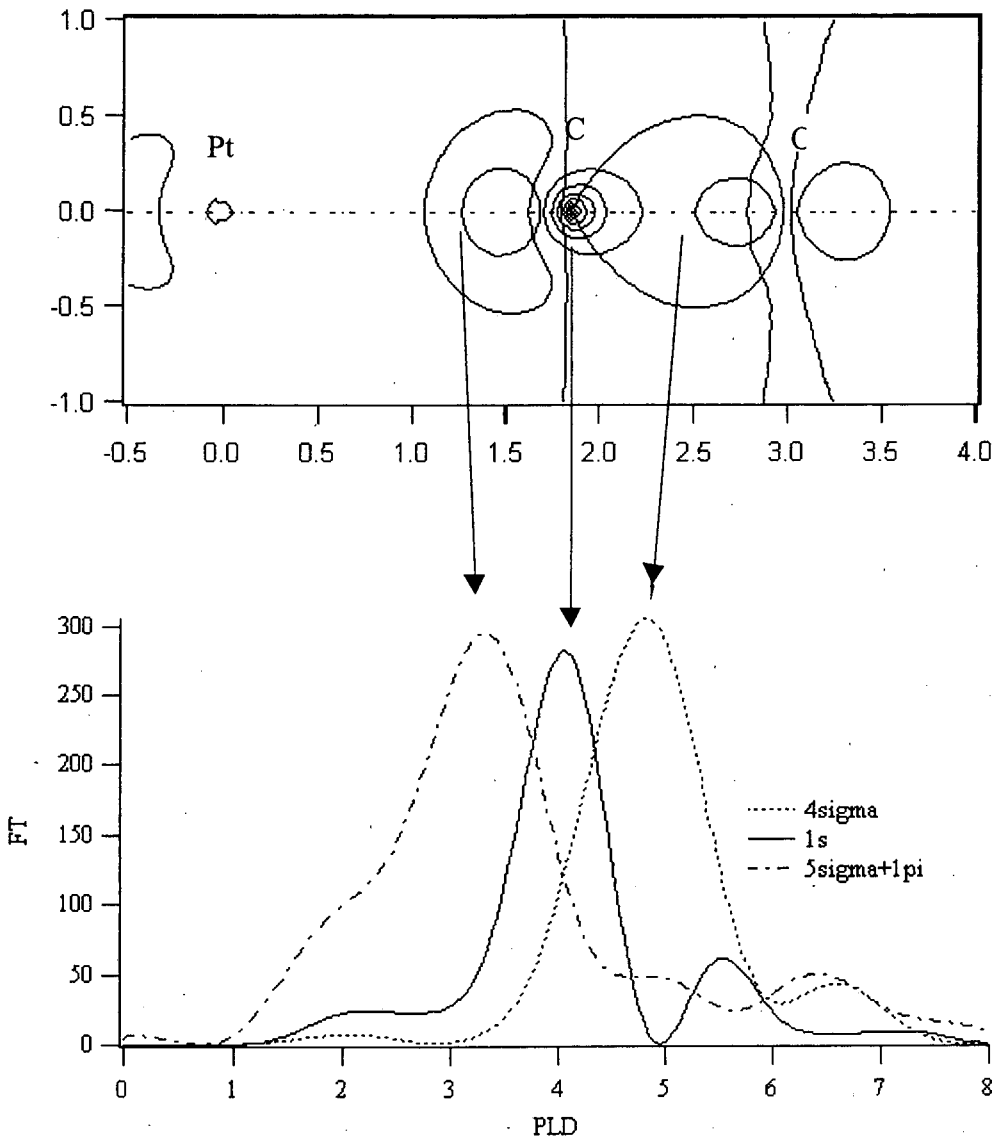

FIG. 2.6 FT peaks of experimental χ curves lined up against the atoms in real space.

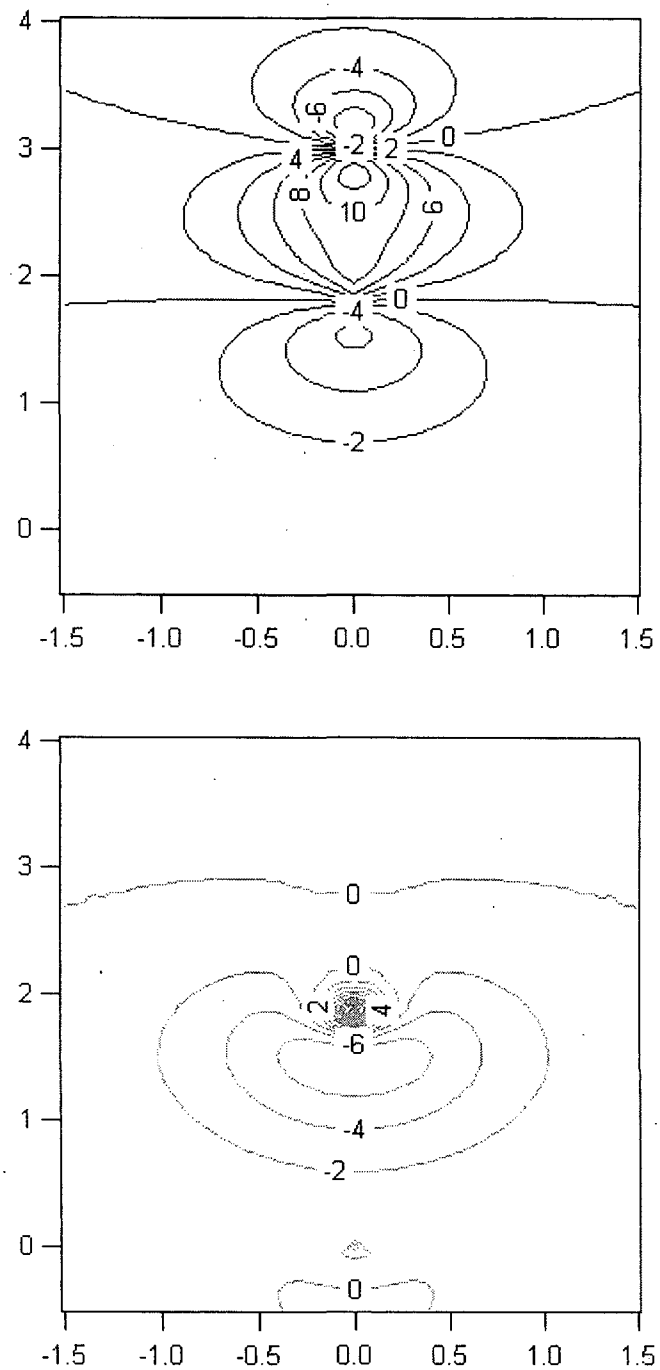

FIG. 2.7 The contour plots of the molecular orbitals obtained through the best fits. The top panel shows the 4σ orbital, and the bottom panel the 5σ orbital.

REFERENCES

[1] S. Hüfner, *Photoelectron Spectroscopy*, 2nd ed. (Springer, Berlin, 1996).

[2] J. Wintterlin, S. Völkening, T.V.W. Janssens, T. Zambelli, and G. Ertl, Science **278**, 1931 (1997).

[3] Ali Alavi, Peijun Hu, Thierry Deutsch, Pier Luigi Silvestrelli, and Jürg Hutter, Phys. Rev. Lett. **80**, 3650 (1998).

[4] B. Hammer, Y. Morikawa, and J.K. Nørskov, Phys. Rev. Lett. **76**, 2141 (1996).

[5] P.H.T. Philipsen, E. van Lenthe, J.G. Snijders, and E.J. Baerends, Phys. Rev. B **56**, 13556 (1997).

[6] John A. Jensen, Keith B. Rider, Miquel Salmeron, and Gabor A. Somorjai, Phys. Rev. Lett. **80**, 1228 (1998).

[7] A.R. Burns, E.B. Stechel, D.R. Jennison, Phys. Rev. Lett. **58**, 250 (1987).

[8] B.N.J. Persson, M Tüshaus, and A.M. Bradshaw, J. Chem. Phys. **92**, 5034 (1990).

[9] A. Cudok, H. Froitzheim, and M. Schulze, Phys. Rev. B **47**,13682 (1993).

[10] D.R. Jennison, P.A. Schultz, and M.P. Sears, Phys. Rev. Lett. **77**, 4828 (1996).

[11] H. Froitzheim, H. Hopster, H. Ibach, and S. Lehwald, Appl. Phys. **13**, 147 (1977).

[12] H.-J. Krebs and H. Lüth, Appl. Phys. **14**, 337 (1977).

[13] G. Apai, P.S. Wehner, R.S. Williams, J. Stöhr, and D.A. Shirley, Phys. Rev. Lett. **37**, 1497 (1976).

[14] J.W. Davenport, Phys. Rev. Lett. **36**, 945 (1976).

[15] D.F. Ogletree, M.A. Van Hove, and G.A. Somorjai, Surf. Sci. **173**, 351 (1986).

[16] Ansgar Liebsch, Phys. Rev. Lett. **32**, 1203 (1974); **38**, 248 (1977).

[17] S. Kono, C.S. Fadley, N.F.T. Hall, and Z. Hussain, Phys. Rev. Lett. **41**, 117 (1978); D.P. Woodruff, D. Norman, B.W. Holland, N.V. Smith, H.H. Farrell, and M.M. Traum, *ibid.* **41**, 1130 (1978); S.D. Kevan, D.H. Rosenblatt, D.R. Denley, B.-C. Lu, and D.A. Shirley, *ibid.* **41**, 1505 (1978).

[18] J.J. Barton, C.C. Bahr, Z. Hussain, S.W. Robey, J.G. Tobin, L.E. Klebanoff, and D.A. Shirley, Phys. Rev. Lett. **51**, 272 (1983).

[19] W.L. Jorgensen and L. Salem, *The Organic Chemist's Book of Orbitals* (Academic, New York, 1973).

[20] J.B. Johnson and W.G. Klemperer, J. Am. Chem. Soc. **99**, 7132 (1977).

[21] T.N. Rhodin and J.W. Gadzuk, in *The Nature of the Surface Chemical Bond*, edited by T.N. Rhodin and G. Ertl (North-Holland, Amsterdam, 1979), Chap. 3.

[22] J.N. Miller, D.T. Ling, P.M. Stephan, D.L. Weissman, M.L. Shek, I. Lindau, and W.E. Spicer, Phys. Rev. B **24**, 1917 (1981).

[23] J.N. Miller, I. Lindau, and W.E. Spicer, Surf. Sci. **111**, 595 (1981); M. Trenary, S.L. Tang, R.J. Simonson, and F.R. McFeely, *ibid.* **124**, 555 (1983).

[24] A. Nilsson, M. Weinelt, T. Wiell, P. Bennich, O. Karis, N. Wassdahl, J. Stöhr, and M.G. Samant, Phys. Rev. Lett. **78**, 2847 (1997).

[25] A. Nilsson and A. Föhlisch (private communication).

[26] Z. Hussain, W.R.A. Huff, S.A. Kellar, E.J. Moler, P.A. Heimann, W. McKinney, H.A. Padmore, C.S. Fadley, and D.A. Shirley, J. Elec. Spec. and Rel. Phen. **80**, 401 (1996).

[27] Yong-Joo Kim, Ph.D. Thesis, University of Hawaii, 1995, and Lawrence Berkeley National Laboratory Report No. LBL-37449.

[28] G. Ertl, M. Neumann, and K.M. Streit, Surf. Sci. **64**, 393 (1977); H. Hopster and H. Ibach, *ibid.* **77**, 109 (1978); H. Steininger, S. Lehwald, and H. Ibach, *ibid.* **123**, 264 (1982); B.E. Hayden and A.M. Bradshaw, *ibid.* **125**, 787 (1983); R.G. Tobin and P.L. Richards, *ibid.* **179**, 387 (1987); E. Schweizer, B.N.J. Persson, M Tüshaus, D. Hoge, and A.M. Bradshaw *ibid.* **213**, 49 (1989); I.J. Malik and M. Trenary, *ibid.* **214**, L237 (1989).

[29] Z. Hussain, D.A. Shirley, C.H. Li, and S.Y. Tong, Proc. Natl. Acad. Sci. USA 78, 5293 (1981).

[30] J.P. Biberian and M.A. Van Hove, Surf. Sci. 138, 361 (1984).

[31] C.S. Fadley and M.A. Van Hove (private communication).

[32] Huasheng Wu, Yufeng Chen, and D.A. Shirley (unpublished).

[33] Yufeng Chen and M.A. Van Hove, computer code MSCD, Lawrence Berkeley National Laboratory, 1998.

[34] J.J. Rehr and R.C. Albers, Phys. Rev. B 41, 8139 (1990).

[35] J.J. Rehr, J. Mustre de Leon, S. I. Zabinsky, and R. C. Albers, J. Am. Chem. Soc. 113, 5135 (1991).

[36] S.I. Zabinsky, J.J. Rehr, A. Ankudinov, R.C. Albers and M.J. Eller, Phys. Rev. B 52, 2995 (1995).

[37] Edward J. Moler, Scot A. Kellar, W.R.A. Huff, Zahid Hussain, Yufeng Chen, and David A. Shirley, Phys. Rev. B 54, 10862 (1996).

[38] Zhengqing Huang, Z. Hussain, W. Huff, E.J. Moler, and D.A. Shirley, Phys. Rev. B 48, 1696 (1993).

[39] Y. Zheng, Z. Hussain, and D.A. Shirley, Chem. Phys. Lett. **206**, 161 (1993).

[40] K. Siegbahn, U. Gelius, H. Siegbahn, and E. Olson, Phys. Lett. 32A, 221 (1970); Physica Scripta, 1, 272 (1970).

[41] D.A. Shirley, J. Stöhr, P.S. Wehner, R.S. Williams, and G. Apai, Physica Scripta 16, 398 (1977).

[42] E.W. Plummer and T. Gustafsson, Science 198, 165 (1977).

[43] J. Osterwalder, T. Greber, S. Hüfner, and L. Schlapbach, Phys. Rev. Lett. 64, 2683 (1990).

[44] Edward J. Moler, Scot A. Kellar, Zahid Hussain, Yufeng Chen, David A. Shirley, W.R.A. Huff, and Zhengqing Huang, Phys. Rev. B 56, 16016 (1997).

[45] G. Blyholder, J. Chem. Phys. 68, 2772 (1964).

[46] A. Nilsson, N. Wassdahl, M. Weinelt, O. Karis, T. Wiell, P. Bennich, J. Hasselström, A. Föhlisch, J. Stöhr, and M. Samant, Appl. Phys. A 65, 147 (1997).

[47] R.P. Messmer, in The Nature of the Surface Chemical Bond, edited by T.N. Rhodin and G. Ertl (North-Holland, Amsterdam, 1979), Chap. 2.

[48] Itai Panas and Per E.M. Siegbahn, J. Chem. Phys. 92, 4625 (1990).

[49] A.C. Pavão, M. Braga, C.A. Taft, B.L. Hammond, and W.A. Lester, Jr., Phys. Rev. B 43, 6962 (1991).

Chapter 3. An Angle-Resolved Photoemission Extended Fine Structure Study of the Clean Ni(111) Surface

ABSTRACT

We report a study of the clean Ni(111) surface structure with the purpose of further understanding the quantum mechanical phenomenon of photoelectron diffraction in solids in general and the technique of Angle-Resolved Photoemission Extended Fine Structure (ARPEFS) in particular. We measured the Ni 3p and 3s photoemission intensity as a function of final state wavevector in normal emission and 60 degree off-normal emission configurations using a third generation synchrotron radiation source. A Fourier transform applied to the k-space ARPEFS data reveals peaks in real space that correspond to path length differences of the scattering electrons. We also modeled the ARPEFS data with an improved version of multiple-scattering simulation program. The modeling was successful for this many-layer system, and detailed conclusions were drawn about the scattering processes that produce both the χ curve and each peak in the FT spectrum. The best-fit calculation shows a bulk terminated Ni(111) surface.

I. INTRODUCTION

Angle-Resolved Photoemission Extended Fine Structure (ARPEFS) has been successfully applied to various adsorbate systems since its inception in 1983 [1]. It

generally yields very precise bond length and inter-layer distance information, with accuracy in the neighborhood of 0.02-0.05Å or better. When applying the Fourier transform to ARPEFS data, strong peaks emerge at photoelectron Path Length Differences (PLD) which can be derived from geometrical parameters of the experimental system. Most of these peaks can be understood using single backscattering and a cluster model [2].

However, when we measure photoemission from the adatoms, which are usually sparsely placed on a surface, the scattering between the emitter atoms themselves is weak, and there is no forward focusing/defocusing phenomenon involved. When we turn to a clean metal surface, like Ni(111), we are presented with a unique opportunity to look at the photoelectron diffraction process within a densely packed top layer itself, as well as the complication of many layers of emitter atoms, in one experiment [3]. Both single-scattering and multiple-scattering contribute significantly to the whole effect, as evidenced by the Power Spectral Density function generated by the autocorrelation autoregression (ACAR) method, discussed in chapter 4, and further confirmed by a full-fledged multiple-scattering simulation program using Rehr-Albers separable representation propagator [4]. In fact, for this densely packed, multiple source layer system, in the high symmetry normal emission geometry, some peaks are strongly affected by, or arise from, multiple scattering and/or multiple paths. These peaks are modeled in detail. It is shown that certain peaks can be assigned to specific source layers. This could facilitate the study of multilayer and interface systems. At the end of our data analysis, we also confirm earlier LEED work on the Ni(111) surface structure [5].

II. EXPERIMENT

The experiment was performed in an ultra-high vacuum chamber (base pressure of 4×10^{-11} torr), equipped with a PHI hemispherical electron energy analyzer and a liquid-Nitrogen-cooled 5-degrees-of-freedom sample manipulator, on beamline 9.3.2 at the Advanced Light Source in Lawrence Berkeley National Laboratory [6]. The Ni crystal was cleaned by argon ion sputtering and electron beam bombardment annealing cycles. The surface cleanliness and order were periodically monitored with synchrotron XPS and LEED. The sample surface temperature was kept at 120K throughout the data collection. The photon polarization vector was oriented 30° from electron analyzer lens axis. The total experimental energy resolution, including photon monochromator resolution and electron analyzer resolution, was ~1.5 eV for the Ni 3s measurements and ~0.7 eV for the Ni 3p measurements, and it varied in a 20% range as the photon energy was varied. Every ARPEFS curve is reduced from a series of photoemission spectra, with each spectrum looking at a constant initial state peak with a particular photon energy, to provide equal $0.05 Å^{-1}$ steps in the photoelectron wavevector.

III. DATA ANALYSIS

We fit every photoemission peak with a Voigt function, along with its own inelastic tail modeled by a Voigt-convoluted step function, and a single background function for the whole spectrum [7].

The area of the Voigt function divided by background height gives the photoemission intensity at the electron kinetic energy obtained as the center of that Voigt. This intensity curve is then spline-fit through five points to yield the oscillating χ curve, the final experimental ARPEFS,

$$\chi(k) = \frac{I(k) - I0(k)}{I0(k)}.$$

A computer program based on a cluster model and the Rehr-Albers formalism has been developed to simulate the photoelectron diffraction process inside a solid. Up to eighth-order scattering, fourth-order electron propagator and two hundred atoms can be accounted for in the simulation [8,9]. In our analysis of this experiment, we used a bowl-shaped cluster of atoms, with a parabolic cross section profile. For normal emission geometry, 104 atoms in 5 layers were used in a 6.6Å radius, 9.8Å depth setting; for off-normal emission, 83 atoms in 4 layers were used in a 7.5Å radius, 6.2 Å depth setting, with the bowl axis pointing to the electron detector aperture. In fitting the experimental curve with a theoretical simulation, only one structural parameter, the interlayer distance between the first and the second monolayer, and some non-structural parameters were varied to achieve the minimum R-factor, defined as follows:

$$R = \frac{\sum(\chi_{\exp} - \chi_{cal})^2}{\sum(\chi_{\exp}{}^2 + \chi_{cal}{}^2)}.$$

The varying non-structural parameters are the Debye temperature, the inner potential, the two electron-detector-direction angles, θ_e and ϕ_e, the two photon-polarization angles, $\theta_{h\nu}$ and $\phi_{h\nu}$, all within 2° of laser-calibrated experimental values. The sample temperature is

measured to be 120K, the detector aperture is set at 2°, and the inelastic mean free path (IMFP) is calculated with the Tanuma-Powell-Penn formula [10]. The electron-atom scattering partial-wave phase shifts are calculated to the 20th order using the tabulated atomic potentials by Moruzzi, Janak and Williams [11].

IV. FOURIER ANALYSIS

If we think of the photoelectrons coming from the photoexcited atom directly into the analyzer aperture as the reference wave, and the electrons elastically scattered off nearby atoms into the aperture as the object wave, then their path-length difference (PLD) contributes to a phase term in the final wavefunction, which is mainly responsible for the interference phenomenon, described here by the χ curve

$$\chi(k) = \sum_j A_j(k)\cos[k(R_j - R_j\cos\theta_j) + \phi_j] \ .$$

The Fourier transform of the ARPEFS into real space thus yields discrete peaks that reveal these path length differences, (R_j-$R_j \cos\theta_j$).

A Ni 3p normal emission

To model the FT peaks separately, we performed a series of calculations on model clusters of Ni atoms. We first consider seven atoms in the (111) surface layer, with the central atom as the only photoelectron emitter, which we label as "7 atoms = 7" in FIG. 3.6. We add 3 atoms in the second layer that are closest to the [111] axis normal through the same emitter, which we label as "10 atoms = 7+3" in FIG. 3.6. Then we expand the

cluster to 7 atoms in the top, 6 atoms in the second, and 3 atoms in the third layer, which we label as "16 atoms = 7+6+3" in FIG. 3.6. The next case is a cluster of 31 atoms with 13 in the top layer, 12 in the second, and six in the third, labeled as "31 atoms = 13+12+6" in FIG. 3.6. The last model cluster consists of 32 atoms in an arrangement similar to the previous 31 atoms case but one more atom in the fourth layer. In these five model clusters, we use only the central atom on the top surface layer as the emitter and calculate only single scattering events for the χ curves. Afterwards, we perform FT on the χ curves and show them in FIG. 3.6. It is quite evident by looking at the FT peaks in our cluster series that the 2.8Å peak come from in-plane scattering off the six nearest neighbor atoms, the 4.3Å peak from scattering off the three second layer atoms plus six next nearest neighbor atoms in the first layer, the 8.2Å peak from backscattering off the three third layer atoms, and the 12.0Å peak from backscattering off the fourth layer atom directly beneath the top layer emitter.

B Ni 3s normal emission

The same calculations are performed for the Ni 3s initial states. Those FT peaks in the Ni 3p cases are mostly present in the Ni 3s cases, while the relative intensities are different, particularly for the 2.8Å peak. This difference is only natural in that the 3s initial state transitions into an odd-parity p-like final state before being scattered, which make the scattered waves off the six top-layer nearest neighbor atoms cancel each other. However, the 3p initial state transitions into an even-parity s-and-d-like pre-scattering state, and

subsequently produces a large FT peak for that same 2.8Å path length difference, because the nearest neighbor scattering amplitudes add up rather than cancel out.

C More refinements

If we want to understand the height of each FT peak a little better, we need to go beyond single scattering, single emitter simulations. For example, the 8.2Å peak in our cluster model calculations is stronger than the 2.8Å peak for Ni 3p initial state, while the experimental data show similar strengths in comparing these two peaks. The reduction in strength for the 8.2Å peak is the effect of double scattering as shown in FIG. 3.10, as the backscattered wave off the third layer atoms can also be scattered off the second layer atoms on its way out to the detector, shifting the phase with little change in the path length difference to produce cancellation; hence the smaller but unmoved FT peak.

In a previous study of clean Ni surface structure by Huff *et al* [3], a 4.3Å peak in the Ni 3p FT is very strong, and the clean Cu 3p ARPEFS also showed a strong peak at a similar PLD. This is contradictory to our experimental result on Ni. The reason is surprisingly simple. In the earlier experiment, the samples were mounted 4° off-normal, instead of perfectly normal, with respect to the electron analyzer, due to practical constraints involved in the alignment process. In our experiment, the sample was mounted 1.5° off-normal, mostly due to a slightly bent manipulator that we could not straighten sufficiently. This small change in electron emission angle induces a perhaps surprisingly large change in the intensity associated with the 4.3Å peak, and shifts the peak position to below 4Å. The simulations for varying the emission angle are vividly shown in FIG. 3.8.

We can also explain it with a little trigonometry here. Suppose we start with the normal emission of a two-atom system, as shown in FIG. 3.9. Then we tilt the emission angle for a small angle δ. The change induced for the path length difference is

$$\begin{aligned}\Delta PLD &= R[1+\cos(\theta-\delta)] - R(1+\cos\theta) \\ &= 2R\sin\frac{2\theta-\delta}{2}\sin\frac{\delta}{2} \\ &\approx R\delta\sin\theta,\end{aligned}$$

where R is the bond length between the scatterer and the emitter, θ is the fixed angle between the surface normal direction and the bond. In a truly normal emission setup of a Ni(111) crystal, the PLD is 4.5Å for scattering off the three second layer atoms, and 4.3Å for in-plane scattering off the six next nearest neighbors. Although the scattering factor is small for the 90° scattering required for these surface scatterers, the multiplication factor of six is big enough to add up against the contribution from the three atoms down below on the second layer. In the case of δ = 4°, if the scatter is one of the second layer atoms, the PLD change is around ±0.1Å. However, if the scatterer is one of the next nearest neighbor atoms on the top layer, the PLD change would be + 0.3Å or -0.3Å, depending on which side the scatter is at relative to the emission direction. Even though the normal emission scattered wave off the six next nearest neighbor atoms on the top layer may partially cancel the scattered wave off the second layer atoms as shown by the middle panels in FIG. 3.6, a mere 3° misalignment could derail the constructive summation of contributions from the six surface atoms and dissolve the cancellation effect, thus produce a big peak from the strong backscattering off the second layer atoms.

The cancellation effect for the 4.3Å peak in the case of the Ni 3p does not happen for the Ni 3s as evidenced by FIG. 3.7, since the 3s initial state has a stronger cancellation effect already for all the top layer atoms, so that the scattered wave off the second layer atoms cannot be affected much. This symmetry-related phenomenon was discussed in the previous section for the 2.8Å peak in the Ni 3s case.

The fact that the 2.8Å peak in the Ni 3s FT is not identically zero is worth a few more words. Although the electron emission direction is perfectly normal to the sample surface in our model calculations, the photon polarization direction is not symmetrical with respect to the surface normal. The two lobes of the p-like final state protrude into the vacuum and the crystal bulk by different weights; thus, the scattered waves have different propagation experiences in different directions on the surface. Now we can understand that the normal emission from an s initial state can still give us a FT peak related to the scattering among symmetrically arranged surface atoms. The root of this problem is that the existence of a surface breaks the symmetry of the crystal bulk.

V. CONCLUSION

We have successfully assigned the Fourier transform peaks from our ARPEFS χ curves to specific electron scattering events, and related the intensities of some peaks to multiple scattering and symmetry. The Ni(111) single crystal surface is determined to be a bulk-terminated structure.

ACKNOWLEDGEMENTS

Special thanks to Professor A. McLean of Queen's University for his Voigt function C code. We thank G. Andronaco, N. Hartman, N. Kellogg, J.K. Lee and J. Spring for their help in the experiment. This work was supported by the Director, Office of Energy Research, Office of Basic Energy Sciences of the U.S. Department of Energy under Contract No. DE-AC03-76SF00098.

REFERENCES

4. J.J. Barton, C.C. Bahr, Z. Hussain, S.W. Robey, J.G. Tobin, L.E. Klebanoff, and D.A. Shirley, Phys. Rev. Lett. **51**, 272 (1983).

5. J.J. Barton and D.A. Shirley, Phys. Rev. B **34**, 778 (1986).

6. W.R.A. Huff, Y. Chen, S.A. Kellar, E.J. Moler, Z. Hussain, Z.Q. Huang, Y. Zheng, and D.A. Shirley, Phys. Rev. B **56**, 1540 (1997).

7. S.I. Zabinsky, J.J. Rehr, A. Ankudinov, R.C. Albers and M.J. Eller, Phys. Rev. B 52, 2995 (1995).

8. P. Kaukasoina, M. Lindroos, R.D. Diehl, D. Fisher, S. Chandavarkar, and I.R. Collins, J. Phys.: Cond. Matt. **5**, 2875 (1993).

9. Z. Hussain, W.R.A. Huff, S.A. Kellar, E.J. Moler, P.A. Heimann, W. McKinney, H.A. Padmore, C.S. Fadley, and D.A. Shirley, J. Elec. Spec. Rel. Phen. **80**, 401 (1996).

10. L.Q. Wang, A.E. Schach von Wittenau, Z.G. Ji, Z.Q. Huang, and D.A. Shirley, Phys. Rev. B **44**, 1292 (1991).

11. Huasheng Wu, Yufeng Chen, and D.A. Shirley, computer code SCAT, Lawrence Berkeley National Laboratory, 1995.

12. Yufeng Chen and M.A. Van Hove, computer code MSCD, Lawrence Berkeley National Laboratory, 1998.

13. S. Tanuma, C.J. Powell, and D.R. Penn, J. Elec. Spec. Rel. Phen. **52**, 285 (1989).

14. V.L. Moruzzi, J.F. Janak, and A.R. Williams, *Calculated Electronic Properties of Metals* (Pergamon, New York, 1978).

Table 3.1 Path length differences (PLD) for clean Ni(111) in normal emission geometry.

Emitter	First Scatterer	Second Scatterer	Third Scatterer	PLD in lattice constant a = 3.52Å	PLD in Å
B0	A0			$1/\sqrt{2}-1/\sqrt{3}$	0.46
B1	A0			$1-1/\sqrt{3}$	1.49
A0	A1			$1/\sqrt{2}$	2.49
A0	A3			$3/\sqrt{6}$	4.31
A0	B0			$1/\sqrt{2}+1/\sqrt{3}$	4.52
A0	A2			$\sqrt{2}$	4.98
A0	B1			$1+1/\sqrt{3}$	5.55
A0	C1			$\sqrt{(1/\sqrt{6})^2+(2/\sqrt{3})^2}+2/\sqrt{3}$	8.38
A0	C0			$\sqrt{2}+2/\sqrt{3}$	9.04
A0	D0			$2\sqrt{3}$	12.19
A0	D1			$\sqrt{(\sqrt{3})^2+(1/\sqrt{2})^2}+\sqrt{3}$	12.68
A0	E0			$\sqrt{(1/\sqrt{6})^2+(4/\sqrt{3})^2}+4/\sqrt{3}$	16.38
A0	A1	A3		$\sqrt{2}$	4.98
A0	B1	A3		$1+1/\sqrt{2}$	6.01
A0	B1	A0		2	7.04
A0	C1	A1		$2\sqrt{(1/\sqrt{6})^2+(2/\sqrt{3})^2}$	8.62
A0	C1	B0		$\sqrt{(1/\sqrt{6})^2+(2/\sqrt{3})^2}$ $+1/\sqrt{2}+1/\sqrt{3}$	8.83
A0	B0	C0		$2/\sqrt{2}+2/\sqrt{3}$	9.04
A0	C0	B0		$\sqrt{2}+1/\sqrt{2}+1/\sqrt{3}$	9.50
A0	C0	A2		$2\sqrt{2}$	9.96
A0	C0	B0	A0	$2\sqrt{2}$	9.96
A0	B0	C0	A0	$2\sqrt{2}$	9.96
A0	B0	C1	A3	$2\sqrt{2}$	9.96

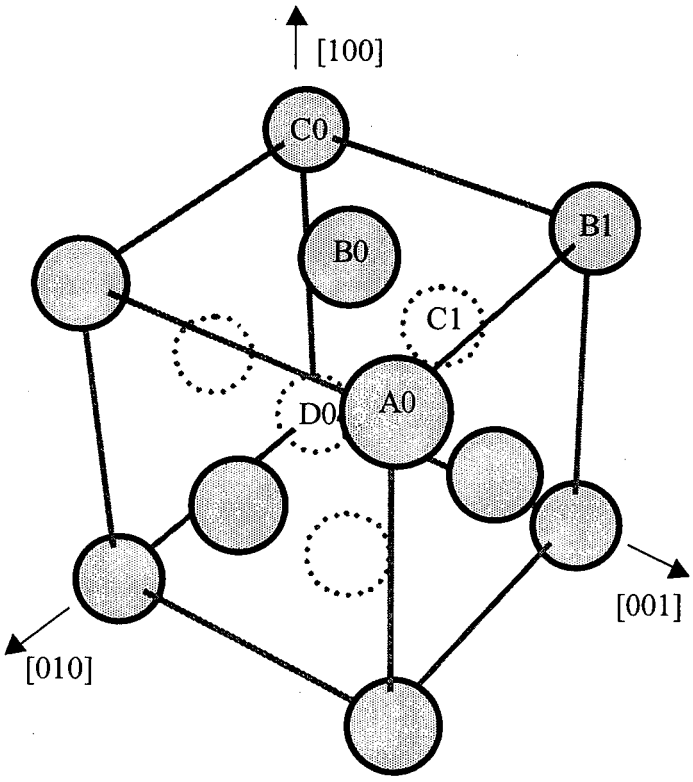

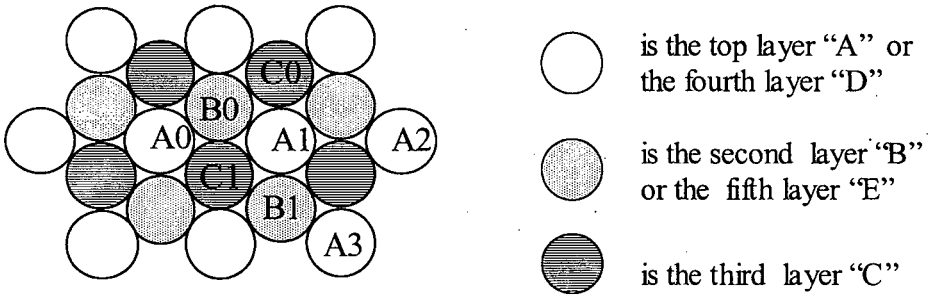

FIG. 3.1 The top panel shows a unit cell of fcc Ni. The bottom panel shows a top view in the [111] direction. Atoms are labeled A,B,C and D to identify atomic layers.

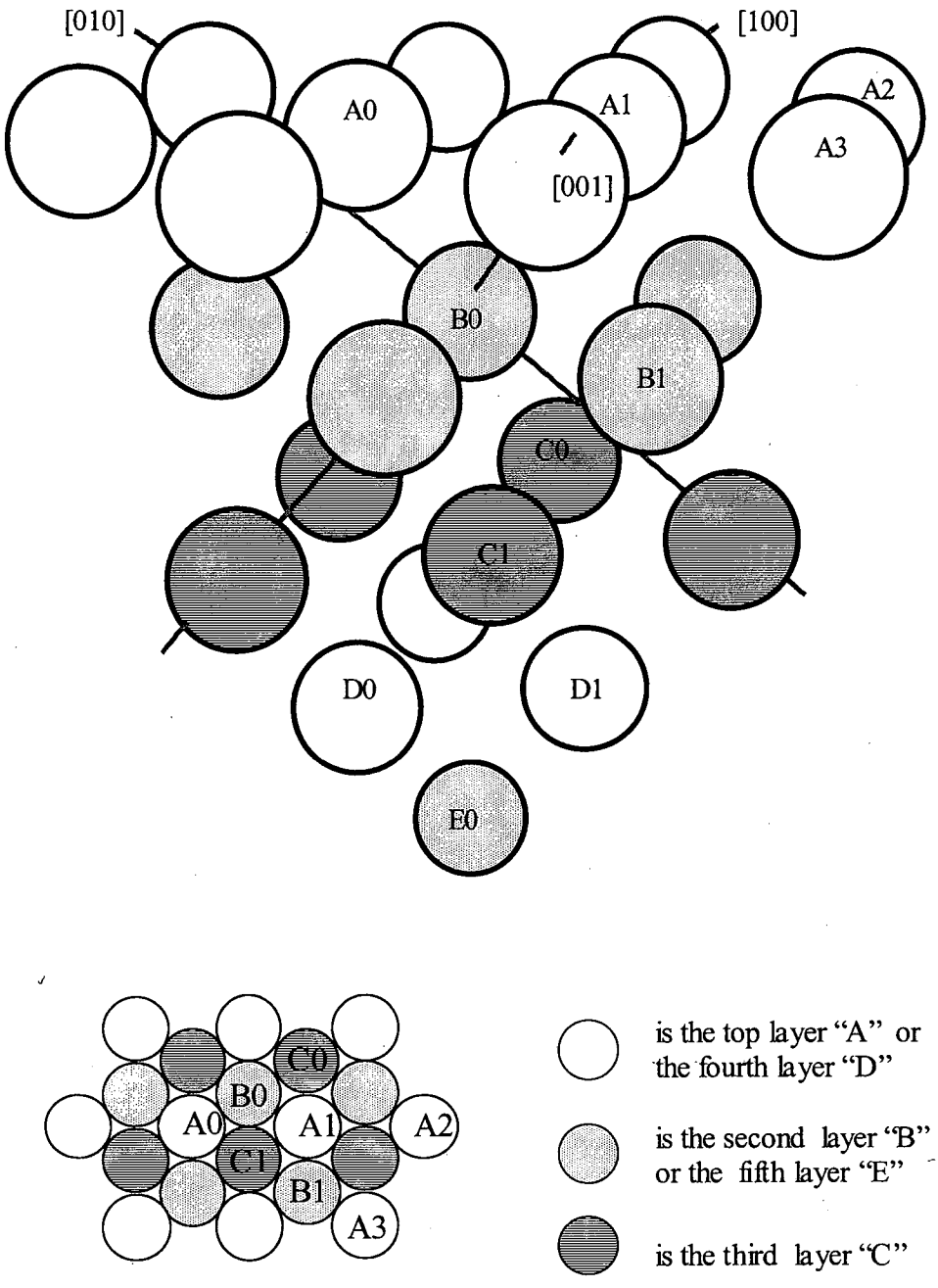

FIG. 3.2 Ni crystal in a perspective view in the top panel, and again in a top view in the [111] direction in the bottom panel.

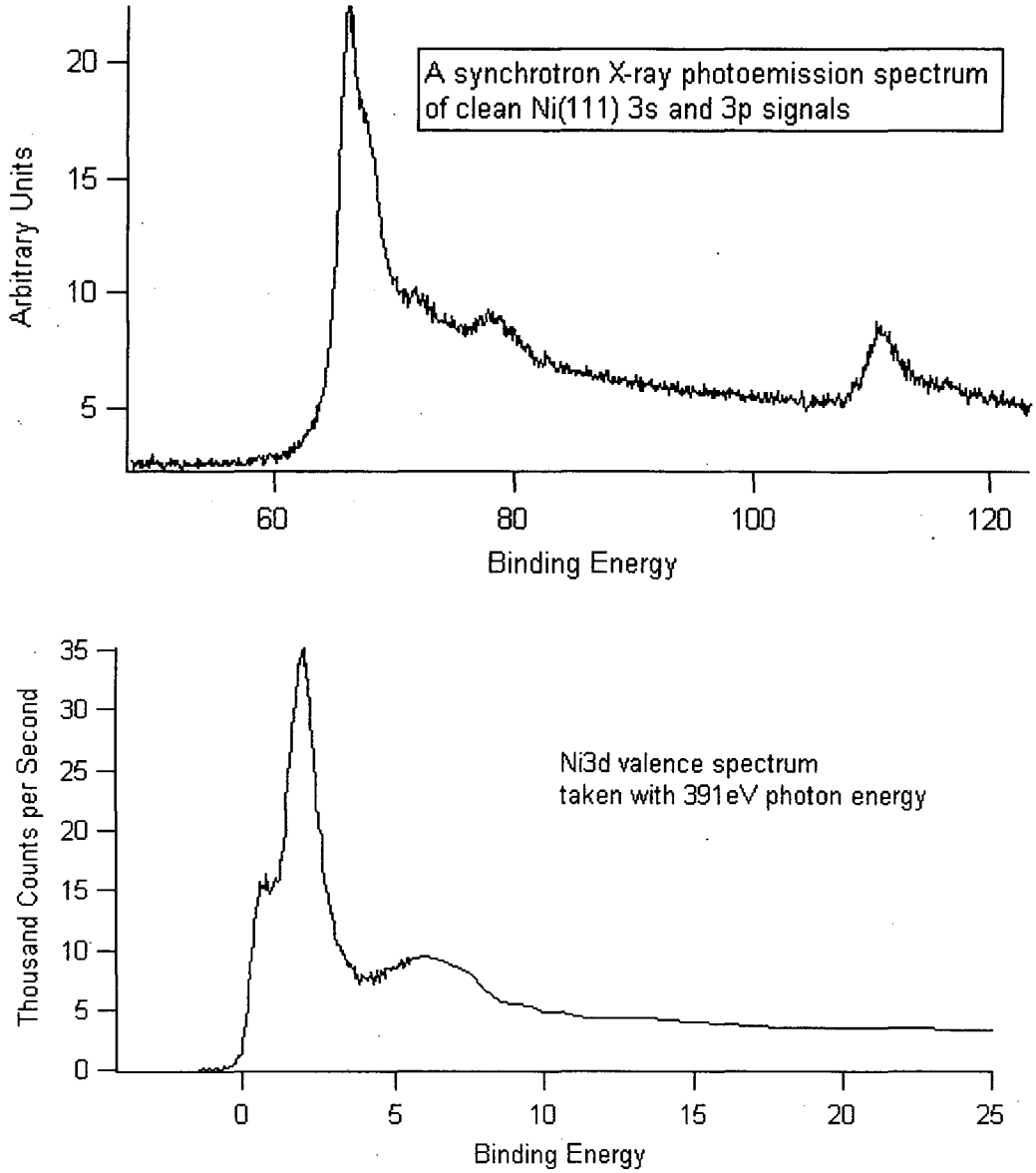

FIG. 3.3 Top panel shows a synchrotron X-ray photoemission spectrum of Ni 3s and 3p peaks and satellites. Bottom panel shows Ni3d band and satellite.

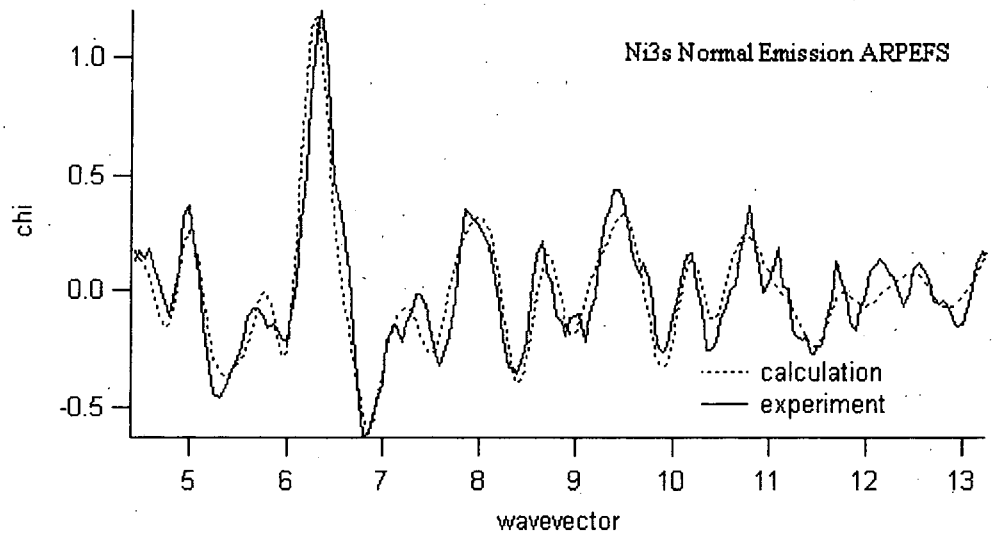

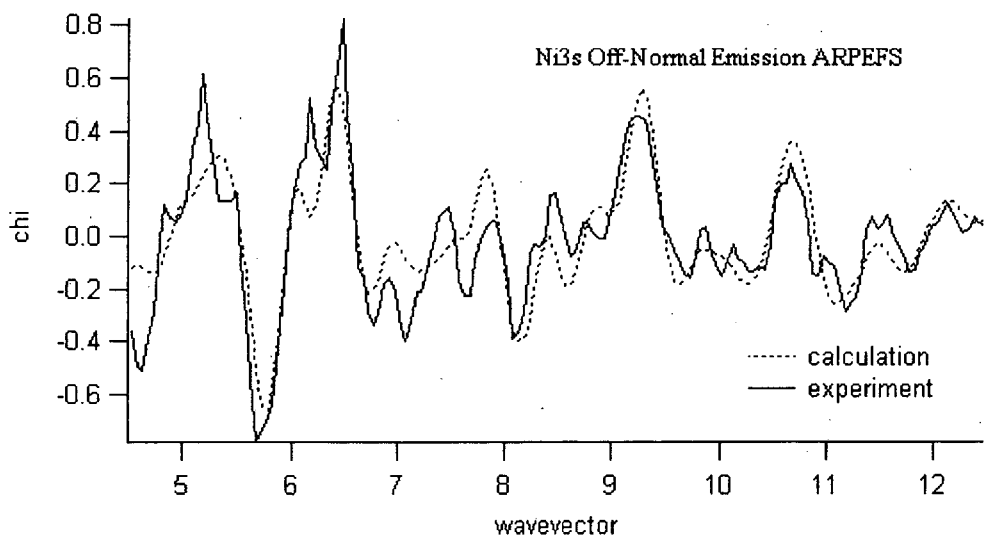

FIG. 3.4 Ni 3s ARPEFS in normal and off-normal emission geometries with best fits.

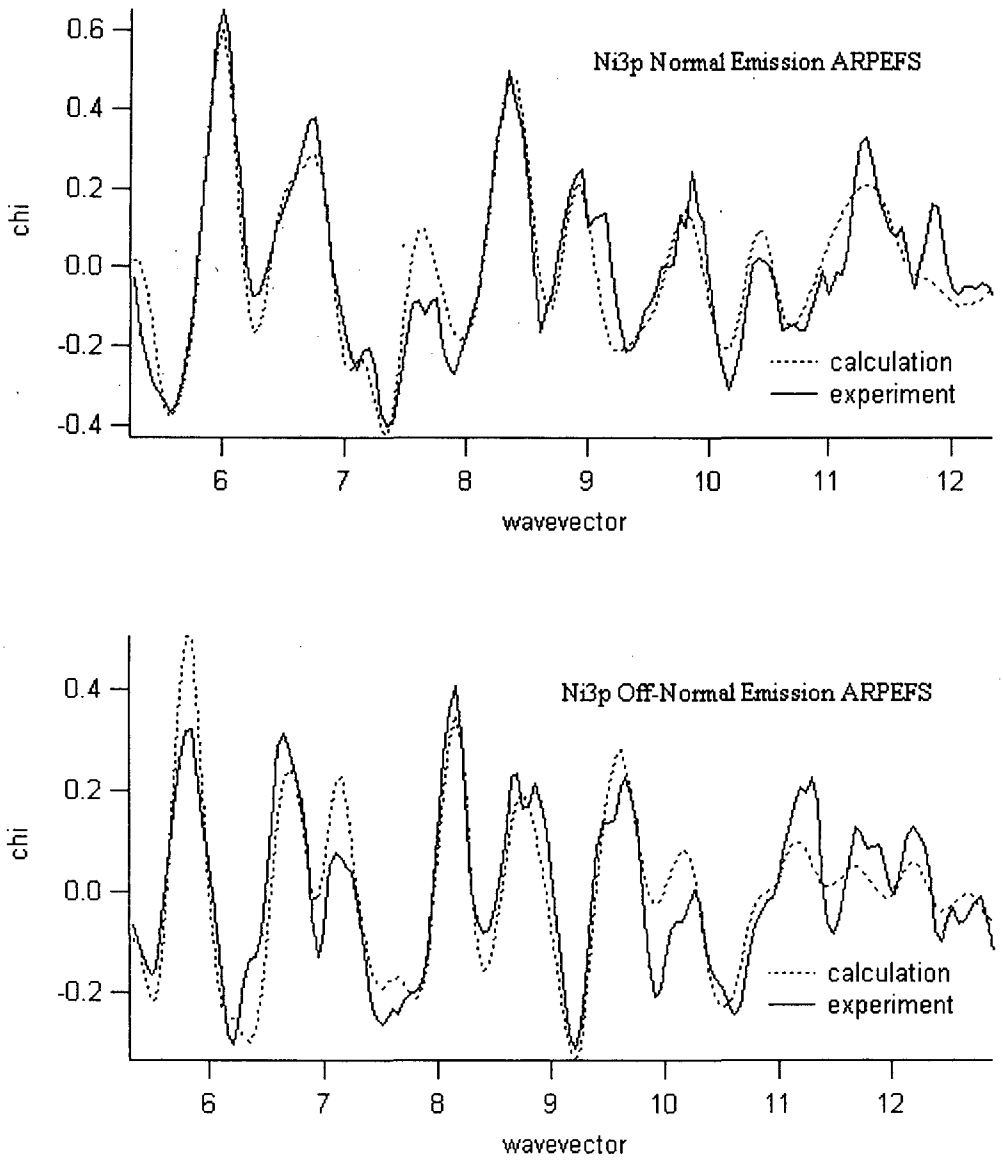

FIG. 3.5 Ni 3p ARPEFS in normal and off-normal emission geometries with best fits.

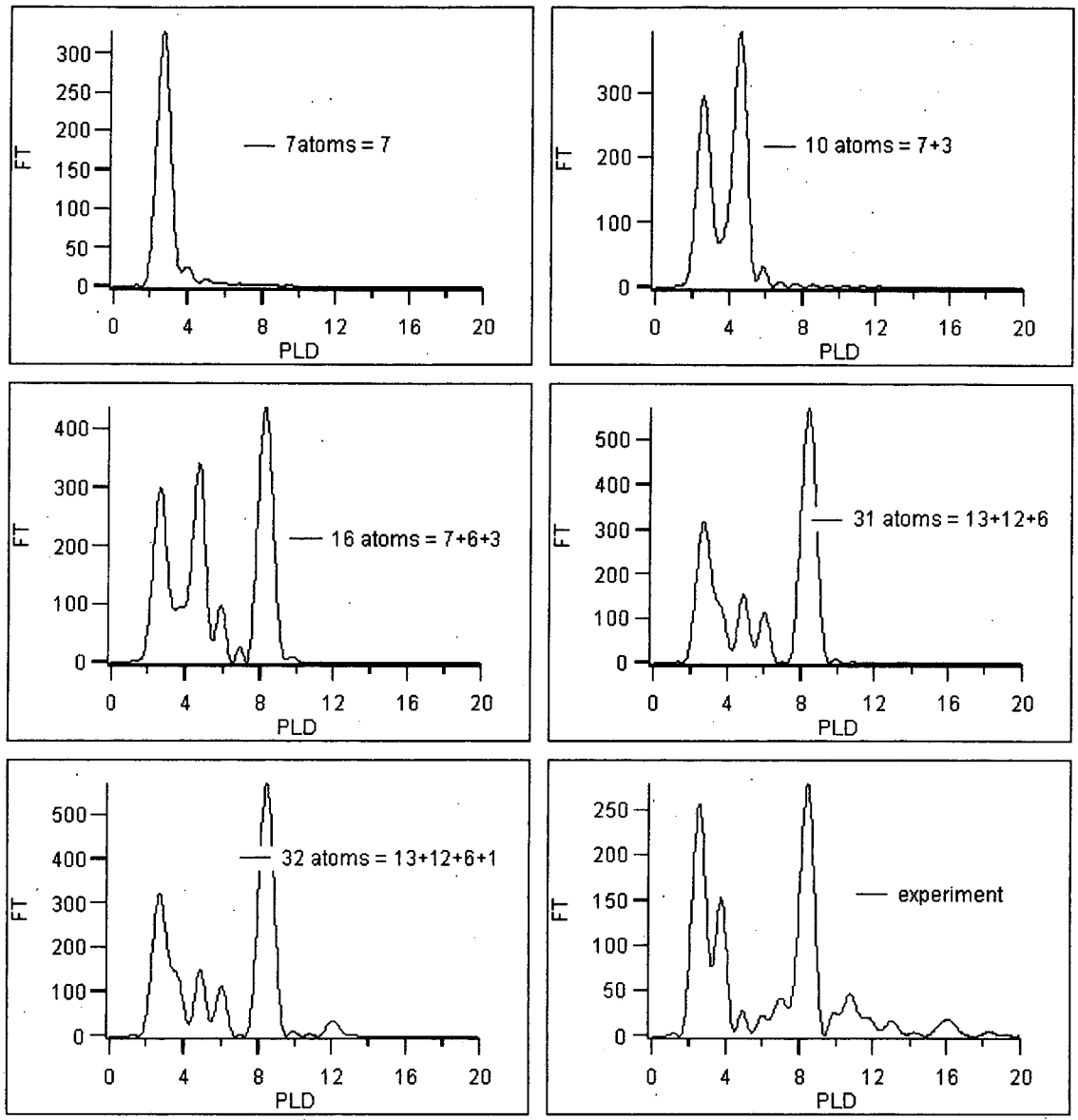

FIG. 3.6 FT of Ni 3p normal emission χ curves calculated with model clusters of increasing sizes. Only top layer atoms are emitters, and only single scattering is considered, except that the last panel shows the FT of the experimental data.

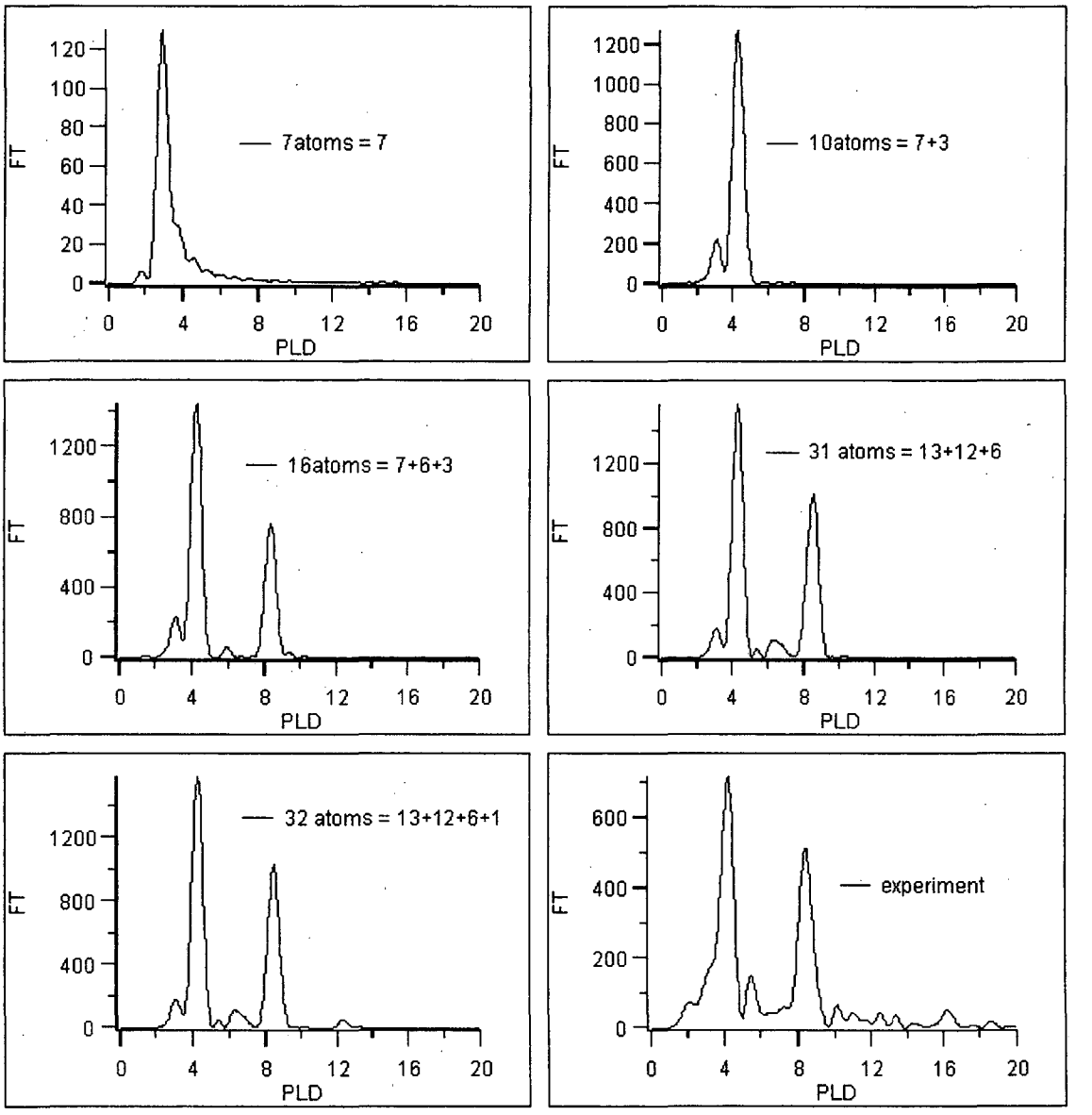

FIG. 3.7 FT of Ni 3s normal emission χ curves calculated with model clusters of increasing sizes, as in Fig. 3.6.

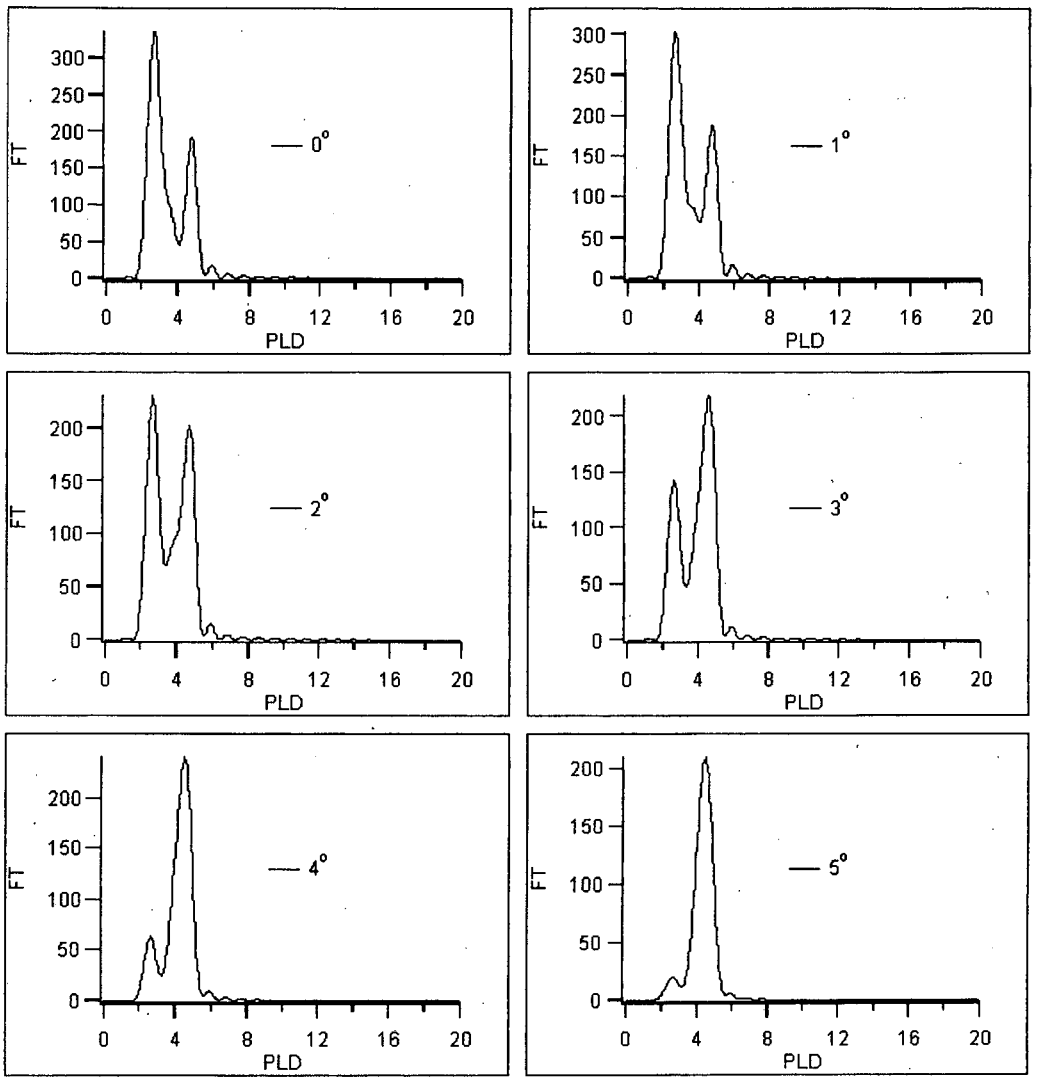

FIG. 3.8 FT of Ni 3p χ curves calculated with increasing emission angles. The model cluster consists of (13+3) atoms, ie. 13 atoms on the top layer and 3 atoms on the second layer of the [111] surface.

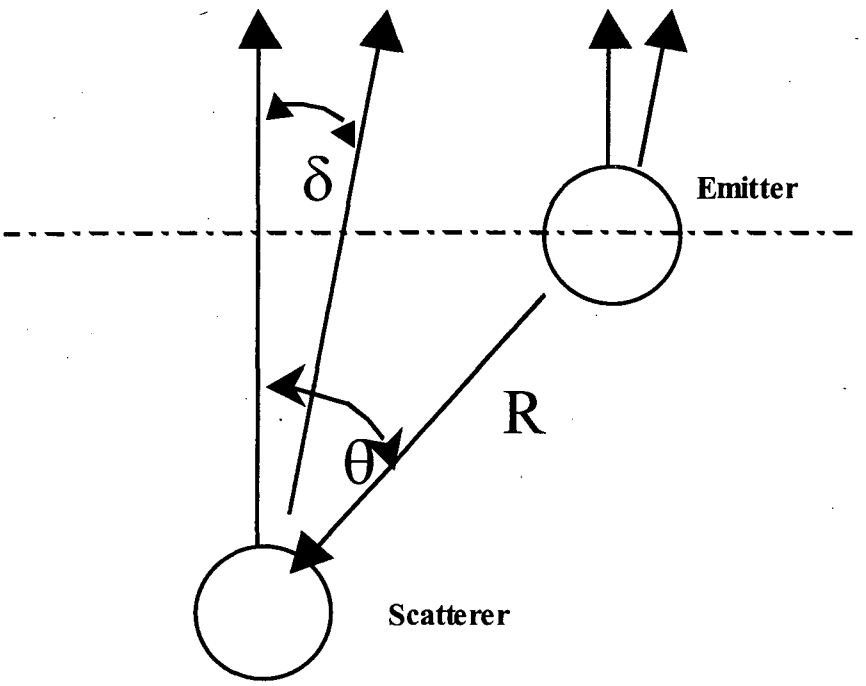

FIG. 3.9 Simplified geometry for our model calculation in Fig. 3.8, where δ is the varied angle from 0° to 5°, and θ the fixed angle between the surface normal direction and a certain scatterer-emitter direction.

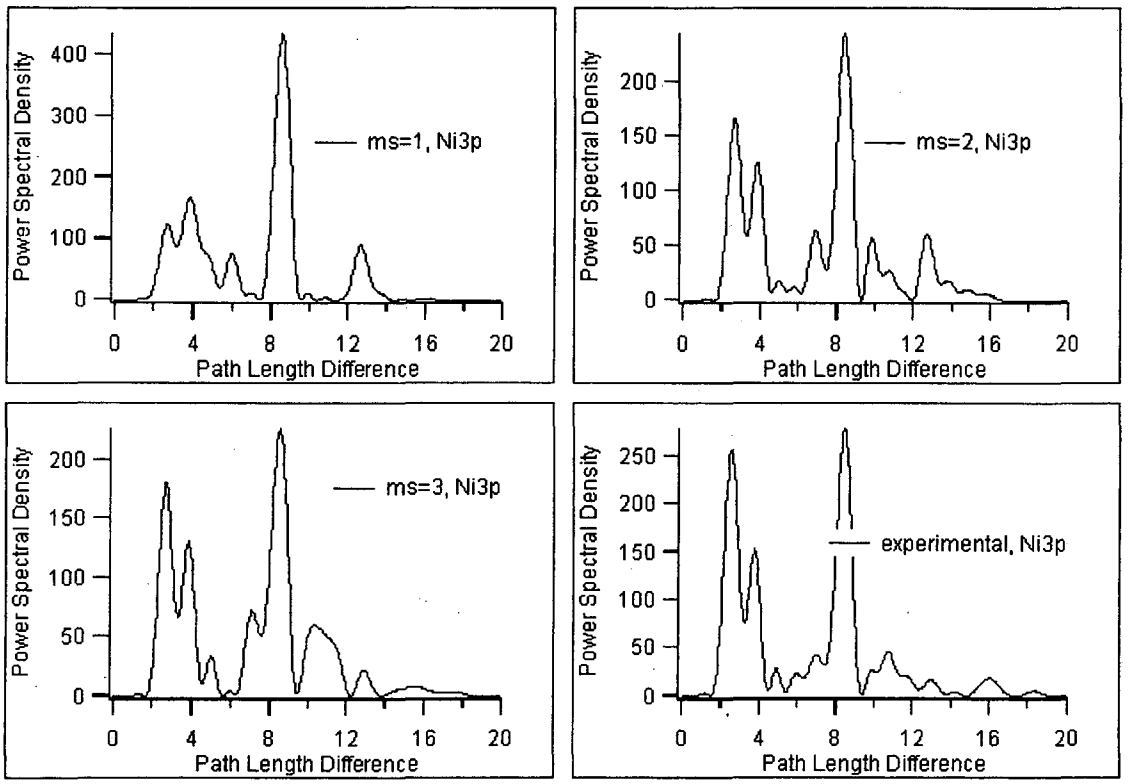

FIG. 3.10 Double scattering reduces the peak around 8.2Å. The cluster used here has 104 atoms in 5 layers.

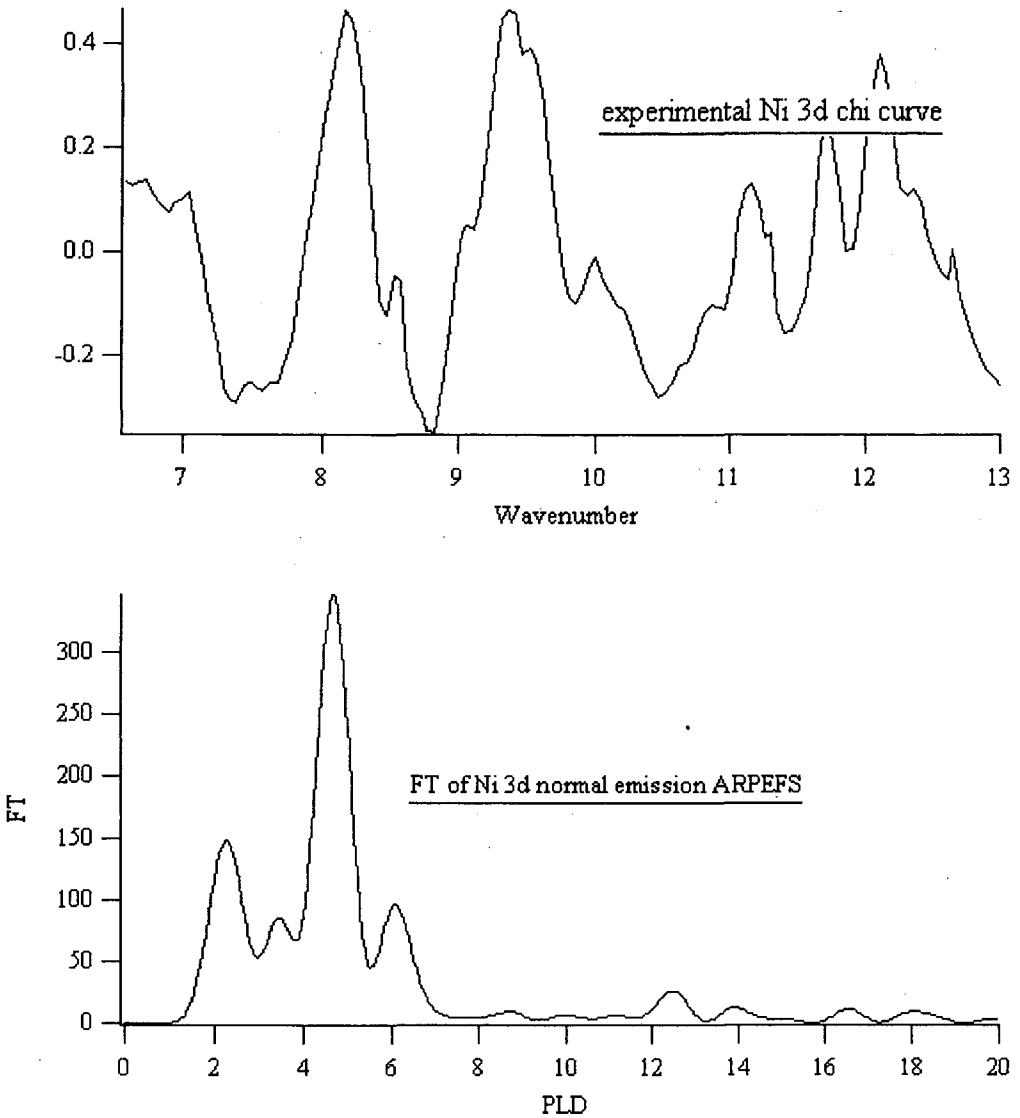

FIG. 3.11 Ni3d valence band normal emission ARPEFS and FT.

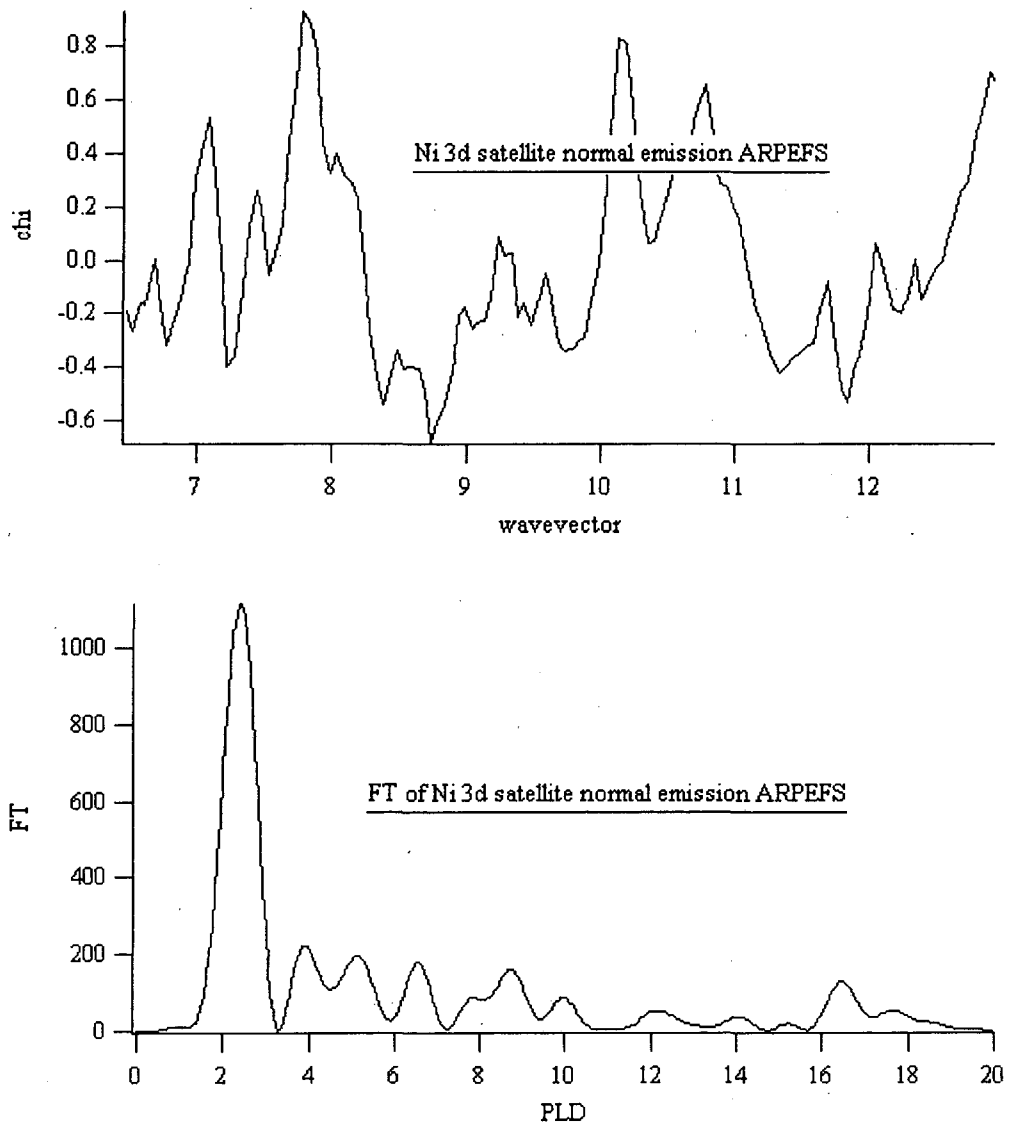

FIG. 3.12 Ni3d satellite normal emission ARPEFS and FT.

Chapter 4. Modern Spectral Analysis of Angle-Resolved Photoemission Extended Fine Structure

ABSTRACT

Modern spectral analysis methods have been widely used in areas involving limited-length evenly-spaced data sequences in place of the traditional direct Fourier Transforms to enhance spectral resolution and signal detectability. We introduce some of these contemporary spectral analysis techniques into Angle-Resolved Photoemission Extended Fine Structure (ARPEFS), and show that they can be a powerful tool in understanding surface structures.

I. INTRODUCTION

Since it was discovered that the Fourier transform (FT) of energy-scan photoelectron diffraction data yields meaningful peaks, people have tried to devise alternative ways to the taper-and-transform approach in the hope of finding better-looking spectra. The direct FT always produces sidelobes besides the main peaks due to the finite data length. If a window function is imposed on the raw data, the sidelobes can be suppressed at the expense of broadening the main peaks. No matter what window function we choose, the resulted spectral function is always a convolution of the FTs of the underlying signals and the imposed window. However, we usually know to some extent what we are looking for

before we actually perform the transform, and the prudent use of this a priori knowledge can reduce the influence of the windowing process while maintaining the reliability of our spectral analysis. Instead of performing FT on the raw data, we look for a set of parameters that describe the data sequence. The spectral function is mathematically linked to the parameters. Therefore, the task is changed into finding the correct parameters. Since the number of parameters is always much smaller than the number of raw data points, the indirect, or parameterized, approach of spectral analysis has the potential of greatly enhancing the spectral resolution, the signal detectability, and the noise suppression. A word of caution here is that any parameterized approach might cause instability in the result, thus great care must be taken in the process.

II. BASIC CONCEPTS AND RELATIONS IN MODERN SPECTRAL ANALYSIS

For notational convenience, our discussion in this section will be formulated in the time and frequency domain, instead of in the momentum and real space. Following the conventions of Marple [5], for a sequence of (M+1) data points, x_0, x_1, x_M, we define the data vector **x** as

$$\mathbf{x} = \begin{pmatrix} x[0] \\ x[1] \\ \vdots \\ x[M] \end{pmatrix},$$

and the complex sinusoid vector $\mathbf{e}_M(f)$ at frequency f as

$$\mathbf{e}_M(f) = \begin{pmatrix} 1 \\ \exp(i2\pi fT) \\ \vdots \\ \exp(i2\pi fMT) \end{pmatrix}.$$

Here x[m] is the $(m+1)_{th}$ data point x_m, where m is an integer. Both f and T are real numbers. T is the constant time lapse between two adjacent data points, therefore it can be thought of as the unit of time in our discussion. Now the discreet Fourier Transform X(f) for this (M+1)-point data train x[n] can be succinctly expressed as

$$X(f) = T\,\mathbf{e}_M^H(f)\mathbf{x}.$$

The autocorrelation sequence (ACS) $r_{xx}[m]$ of the original data x is

$$r_{xx}[m] = \mathcal{E}\{x[n+m]x^*[n]\},$$

where $\mathcal{E}$ means taking the expectation value by averaging over an ensemble. For an infinite data sequence, the ACS $r_{xx}[m]$ can be computed for an arbitrary m. Another useful concept is the autocorrelation matrix $\mathbf{R}_p$, defined as

$$\mathbf{R}_p = \begin{pmatrix} r_{xx}[0] & r_{xx}[-1] & \cdots & r_{xx}[-p] \\ r_{xx}[1] & r_{xx}[0] & \cdots & r_{xx}[-p+1] \\ \vdots & \vdots & \ddots & \vdots \\ r_{xx}[p] & r_{xx}[p-1] & \cdots & r_{xx}[0] \end{pmatrix}.$$

This autocorrelation matrix $\mathbf{R}_p$ is a Hermitian Toeplitz matrix, and it is positive semi-definite.

In a practical situation, the number of data is finite, and often we don't have the luxury of an ensemble of data sets, so we have to settle for a single train of experimental data points. When the calculation of r_{xx} calls for the value of an x[n] with n out of range, we assign zero to that x[n]. The biased autocorrelation estimate is thus obtained as

$$r_{xx}[m] = \frac{1}{M+1} \sum_{n=0}^{M-m} x[n+m]x^*[n], \forall m \geq 0;$$

$$r_{xx}[m] = r_{xx}^*[|m|]\}, \forall m < 0.$$

Therefore we have the largest number of terms in the summation when m=0. This biased estimate of the ACS will ensure the positive semi-definite property of the autocorrelation matrix $\mathbf{R}_p$.

The power spectral density (PSD) can be defined as the discreet Fourier Transform of the autocorrelation sequence

$$P_{xx}(f) = T \sum_{m=-\infty}^{\infty} r_{xx}[m] \exp(-i2\pi f m T).$$

When we use the biased estimate for r_{xx}, computed from $r_{xx}[0]$ up to $r_{xx}[p]$, with p much less than the number of data points M+1, the above expression becomes a Blackman-Tukey correlogram estimator of PSD

$$P_{xx}(f) = T \sum_{m=-p}^{p} r_{xx}[m] \exp(-i2\pi f m T).$$

If we let p = M, the correlogram estimator can be proven to be identical to the sample spectrum,

$$P_{xx}(f) = \frac{T}{M+1}\left|\sum_{m=0}^{M} x[m]\exp(-i2\pi fmT)\right|^2$$
$$= \frac{1}{(M+1)T}|X(f)|^2,$$

which is the familiar periodogram estimator of PSD.

Now suppose the data sequence x[m] consists of L sinusoidal signals and noise w[m], as in a realistic experimental situation,

$$x[m] = \sum_{l=1}^{L} A_l \exp(i2\pi f_l mT + i\theta_l) + w[m]$$

where for the convenience of presentation we are using complex sinusoids as signals. The ACS of this data sequence is computed to be

$$r_{xx}[m] = \sum_{l=1}^{L} A_l^2 \exp(i2\pi f_l mT) + v\delta[m],$$

where v is the variance of the noise w[m]. In practice, we compute r_{xx} from $r_{xx}[0]$ up to $r_{xx}[p]$, with p bigger than L but smaller than (M+1). Alternatively, in the matrix form,

$$\mathbf{R}_p = \sum_{l=1}^{L} A_l^2 \mathbf{e}_p(f_l)\mathbf{e}_p^H(f_l) + v\mathbf{I},$$

where $\mathbf{R}_p$ is the (p+1)-dimensional Toeplitz autocorrelation matrix defined earlier, and $\mathbf{I}$ is the (p+1)-dimensional identity matrix. The first term in $\mathbf{R}_p$, with a rank of L, can be eigendecomposed by its orthonormal eigenvectors $\mathbf{s}_i$ with the eigenvalues λ_i ordered in decreasing value $\lambda_1 \geq \lambda_2 \geq \ldots \geq \lambda_L$,

$$\begin{aligned}\mathbf{R}_p &= \sum_{i=1}^{L} \lambda_i \mathbf{s}_i \mathbf{s}_i^H + v\mathbf{I} \\ &= \sum_{i=1}^{L} \lambda_i \mathbf{s}_i \mathbf{s}_i^H + v \sum_{i=1}^{p+1} \mathbf{s}_i \mathbf{s}_i^H \\ &= \sum_{i=1}^{L} (\lambda_i + v) \mathbf{s}_i \mathbf{s}_i^H + v \sum_{i=L+1}^{p+1} \mathbf{s}_i \mathbf{s}_i^H .\end{aligned}$$

To distinguish between the signals and noise, we assume that all the eigenvalues λ_i which correspond to the real signals are much bigger than the noise level v. Therefore, after we form the autocorrelation matrix $\mathbf{R}_p$ from the raw data and perform the eigendecomposition on it, we can effectively separate the noise subspace from the signal subspace. As the vectors in the noise subspace are orthogonal to any vectors in the signal subspace, a function in the form of

$$P(f) = \frac{1}{\left|\mathbf{e}_p^H(f) \cdot noisevector\right|^2}$$

would have a vanishing denominator, thus a peak, for an f that makes $\mathbf{e}_p(f)$ a signal. In our autocorrelation eigenvector (ACE) approach, we follow Johnson and DeGraaf and choose the frequency estimator to be

$$P(f) = \frac{1}{\mathbf{e}_p^H(f)\left(\sum_{i=L+1}^{p+1} \frac{1}{\lambda_i} \mathbf{s}_i \mathbf{s}_i^H\right)\mathbf{e}_p(f)},$$

where $\mathbf{s}_i$ are the noise eigenvectors of $\mathbf{R}_p$ that have the (p-L+1) smallest eigenvalues $\lambda_{L+1} \geq \lambda_{L+2} \geq \ldots \geq \lambda_{p+1}$.

If the raw data sequence can be described as an autoregressive process of order p,

$$x[m] = -\sum_{k=1}^{p} a[k]x[m-k] + w[m],$$

where a[k] are the p autoregressive parameters, and w[m] is the noise sequence with variance v, the power spectral density P(f) can be proven to be

$$P(f) = \frac{Tv}{\mathbf{e}_p^H(f)\mathbf{a}\mathbf{a}^H\,\mathbf{e}_p(f)},$$

where **a** is the autoregressive parameter vector defined as

$$\mathbf{a} = \begin{pmatrix} 1 \\ a[1] \\ \vdots \\ a[p] \end{pmatrix}.$$

It is easy to see that the autocorrelation sequence $r_{xx}[m]$ satisfies similar relations as the raw data x[m],

$$\begin{aligned} r_{xx}[m] &= -\sum_{k=1}^{p} a[k]r_{xx}[m-k] && \text{for } m > 0 \\ r_{xx}[m] &= -\sum_{k=1}^{p} a[k]r_{xx}[-k] + v, && \text{for } m = 0 \\ r_{xx}[m] &= r_{xx}^{*}[-m] && \text{for } m < 0, \end{aligned}$$

which are called the Yule-Walker autoregression normal equations, when evaluated for p $\geq$ m $\geq$ 0. The matrix form is concisely written as

$$\mathbf{R}_p \cdot \mathbf{a} = \begin{pmatrix} v \\ 0 \\ \vdots \\ 0 \end{pmatrix}.$$

This forms the basis of our autocorrelation autoregression (ACAR) method of calculating the power spectral density. First, we compute the autocorrelation matrix $\mathbf{R}_p$ from the raw data. Second, we solve the Yule-Walker equations to obtain the autoregressive parameters a[k]. Finally, the power spectral density is computed directly from a[k].

Instead of using $\mathbf{R}_p$ as computed directly from the raw data, we can eigendecompose it to pick out the signal subspace and form a new matrix that could give us better spectral resolution due to the reduction in the noise content. Owsley [12] suggested applying this technique to the Minimum Variance (MV) method of spectral analysis, laid out here without proof as

$$P(f) = \frac{T}{\mathbf{e}_p^H(f)\left(\sum_{i=1}^{L} \frac{1}{\lambda_i} \mathbf{s}_i \mathbf{s}_i^H\right)\mathbf{e}_p(f)}.$$

III. COMPARISON OF IMPLEMENTED METHODS

Currently we have written computer programs for four different modern spectral analysis methods (Figure 4.1): AutoRegression-Linear Prediction (ARLP), AutoCorrelation-AutoRegression (ACAR), AutoCorrelation-Eigenvector analysis (ACE), and Minimum Variance (MV). Each method has its own idiosyncrasies that we have to be careful about when applying them to analyze real world data.

We use an example (Fig. 4.2) here to compare the merits of the aforementioned methods. The data are the Angle-Resolved Photoemission Extended Fine Structure (ARPEFS) of P 2s spectra from a $c(2\times2)$P/Fe(100) sample, with emission angle 45° off-normal along the [011] direction. In the single-scattering cluster approximation, ARPEFS can be written as

$$\chi(k) = \sum_j Aj(k)\cos[k(Rj - Rj\cos\theta j) + \phi j],$$

where A_j is a slow-varying function that considers photoemission cross section, thermal vibration, electron mean free path attenuation, and aperture averaging effects; R_j is the vector that starts at the emitter and ends at one of the scatters; θ_j is the scattering angle; ϕ_j is the overall scattering factor phase shift. When we apply the Fourier transform to the χ curve, we produce peaks at path length differences PLD = $(R_j - R_j\cos\theta_j)$, although small deviations are present due to the influence of A_j and ϕ_j. Accidentally, A_j can have a node in the midst of the χ curve, in which case we have the Generalized Ramsauer-Townsend effect, and a certain FT peak is split into two. Since we have this simple geometrical interpretation of ARPEFS-FT, we want to take advantage of the powerful modern spectral analysis methods introduced earlier.

According to the experimental geometry and our single scattering path length difference analysis, we expect to see PLD peaks in real space around 4.0Å, 7.6Å, 11.8Å, and 15.7Å. In Figure 4.2, we found that the direct FT gives us all the signal peaks plus some spurious ones. The spurious 8.5Å peak is even stronger than the real one near 15.7Å. We have no criteria to rule against the meaningfulness of the 8.5Å peak. After imposing the popular

Hanning window on the raw data, we successfully suppressed the 8.5Å peak and anything beyond 16Å. But it is still not clear whether we have anything solid around 15Å or 9Å. We also observe that the width of each peak is significantly bigger than its direct FT counterpart. Of course, we could choose any other window function, but the trade-off between sharpening signals and suppressing sidelobes always exists.

The minimum variance (MV) approach is a parameterized method that gives better resolution and less noise than direct FT. It needs as input from the human operator the number of lags p and the number of signals L in order to compute the autocorrelation matrix and then reduce its rank to the signal subspace. The calculation time is twice as long as that of the autocorrelation autoregression (ACAR) approach, and yet the resolution is worse than that of ACAR. We recommend using ACAR in most cases, as it needs as input only the number of lags p.

The ARLP approach was developed in our group in the early days to improve upon the direct FT. It is a hybrid method in that it uses the raw data to compute a covariance matrix, which is used subsequently to calculate the autoregressive parameters, which are then used to extrapolate the original data set in the left and right directions equally far, so as to create an extended data set, often three times as long as the raw data, and finally a windowed FT is performed on this extended data set. We can see from Figure 4.2 that ARLP produces quite sharp peaks, even sharper than ACAR; however, there are also many small bumps in the spectrum that defy explanation. The ARLP method requires as input the number of lags p for the covariance data matrix and the number of signals L which are used in the singular-value decomposition of the covariance data matrix. The

number of extrapolated data points and the specific window function are also inputs from the human operator, but the final spectrum is rather insensitive to them.

The autocorrelation eigenvector (ACE) approach has the best spectral resolution and signal detectability. It also needs two inputs: the number of lags p and the number of signals L.

In terms of the stability, or the sensitivity to human inputs, the direct FT is the most stable, as it really deals with the raw data only, and ARLP is the least stable, as it requires the most intervention. As we said earlier, while ensemble averaging is essential for the statistical stability of spectral analysis, we are often left with only one data set. Therefore the interactive use of the computer programs is absolutely necessary to simulate a pseudo-ensemble. In the traditional FT process, people would cut the one data train they have into small pieces of equal length, then average the FT results from the small pieces to improve the reliability of main peaks. Afterwards the number of pieces would be decreased and the FT peaks would become sharper and sharper. This so-called "window closing" procedure enables one to identify the true signals among the sidelobes and the noise peaks, and to pin down their positions later. In modern parameterized spectral analysis methods, e.g. in ACAR, we start from a small number of lags p, usually one quarter the number of data points, and keep increase p till all the main peaks are stable and sharpest in the spectrum, usually when p is around one half the number of the data points. This is the so-called "order-closing" procedure. Currently, we find ACAR to need the least human intervention and to be capable of producing the most reliable spectra,

although we cannot foresee or preclude any foolproof, hands-off algorithm of spectral analysis at this stage.

ACKNOWLEDGEMENTS

Thanks to W.R.A. Huff, S.A. Kellar, E.J. Moler, and Y. Zheng for their help in using the original ARLP program on a VAXstation 3100 machine.

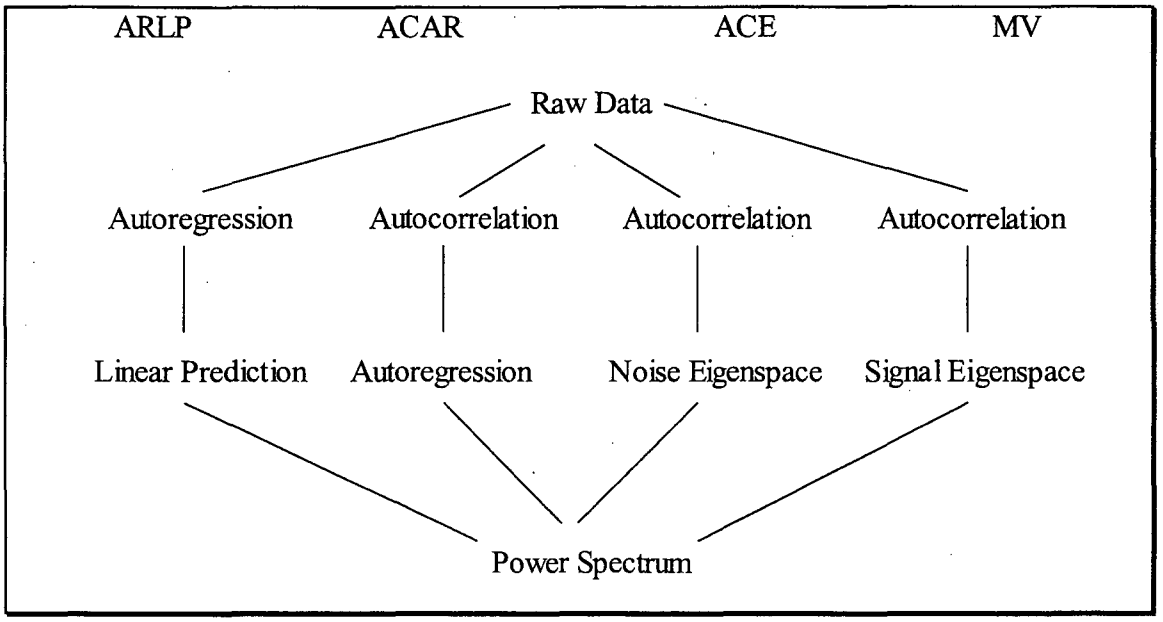

FIG. 4.1 Flow Chart comparing four modern spectral analysis methods.

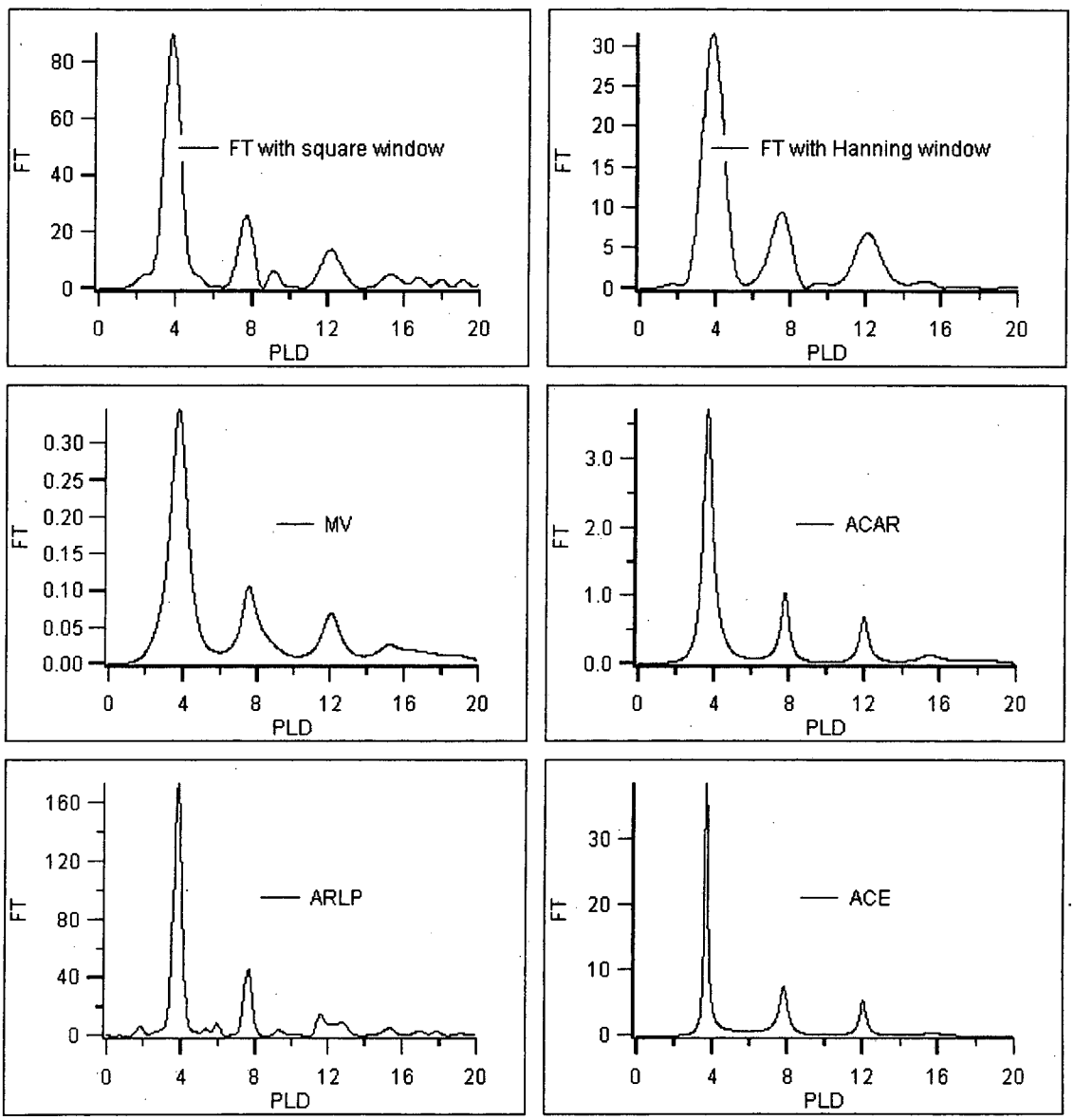

FIG. 4.2 Power spectral density functions of P 2s ARPEFS. The sample is *c*(2×2)P/Fe(100), with emission angle 45° off-normal along the [011] direction. The various spectral analysis methods show varying degrees of resolution. The x-axis is Path Length Difference (PLD) in Å.

REFERENCES

15. E. Matthias and D.A. Shirley, Nucl. Instr. **45**, 309 (1966).

16. S. Koicki, T.A. Koster, R. Pollak, D. Quitmann, and D.A. Shirley, Phys. Lett. **32**B, 351 (1970).

17. Z. Hussain, D.A. Shirley, C.H. Li, and S.Y. Tong, Proc. Natl. Acad. Sci. USA **78,** 5293 (1981).

18. S.M. Kay and S.L. Marple Jr., Proc. IEEE **69**, 1380 (1981).

19. S.L. Marple Jr., *Digital Spectral Analysis with Applications* (Prentice-Hall, Englewood Cliffs, 1987).

20. S.M. Kay, *Modern Spectral Estimation* (Prentice-Hall, Englewood Cliffs, 1987).

21. S. Haykin, Editor, *Nonlinear Methods of Spectral Analysis*, 2nd Edition (Springer, Berlin, 1983).

22. J. Barton and D.A. Shirley, Lawrence Berkeley National Laboratory Report No. LBL-14758 Rev., 1985 (unpublished).

23. J.N. Kapur, *Maximum Entropy Models in Science and Engineering*, Revised Edition (Wiley, New Dehli, 1993), Chap. 16.

24. W.T. Shaw and J. Tigg, *Applied Mathematica: Getting Started, Getting It Done* (Addison-Wesley, Reading, 1994), Chap. 20.

25. D.H. Johnson and S.R. DeGraaf, IEEE Trans., ASSP-30, 638 (1982).

26. N.L. Owsley, in *VLSI and Modern Signal Processing*, edited by S.Y. Kung, H.J. Whitehouse, and T. Kailath (Prentice-Hall, Englewood Cliffs, 1985), chapter 4.

Chapter 5. Simple Surface Structure Determination by Angle-Resolved Photoemission Extended Fine Structure - Fourier Transform Using Modern Spectral Analysis Techniques

I. INTRODUCTION

X-ray photoelectron diffraction (XPD) as a probe of surface structure was originally proposed by Liebsch, and was demonstrated independently by three groups in different experimental settings [1 - 5]. In our group, the scanned-energy mode of XPD has been applied extensively on various adsorbate systems. Initially, the data were measured only along the surface normal over a limited energy range and fitted with a multiple-scattering theory to determine structures [6 - 9]. Realizing that the scanned-energy data could be reduced to the wavevector-dependent χ curve whose Fourier transform yields peaks at path length differences related to inter-atomic distances, our group recognized the similarities between the scanned-energy XPD and extended x-ray absorption fine structure (EXAFS), as both could be explained quite successfully in the framework of the single-scattering cluster (SSC) [10 - 13]. Later, an improved version of scanned-energy XPD, angle-resolved photoemission extended fine structure (ARPEFS), was developed, in which core-level photoemission data were measured along the surface normal or an off-normal direction over a wide energy range and Fourier-analyzed to obtain qualitative structural information while the quantitative structural parameters were determined by

computer simulation based on the multiple scattering spherical wave (MSSW) theory [13]. In the past few years, ARPEFS has been successfully used to study the structures of atomically and molecularly adsorbed metal and semiconductor surfaces and provided information about the adsorption sites, bond lengths, bond angles, and the relaxation of the surface layers [14 - 30].

The FT analysis is very useful in ARPEFS studies in several ways. For example, ARPEFS-FTs of two adsorbed surfaces should look similar if the adsorption sites and the substrate bulk structures are similar. Some of the above ARPEFS studies have exploited this characteristic of ARPEFS-FT to determine the adsorption sites directly, by comparing the ARPEFS-FTs of adsorbed surfaces of unknown structure with those of well-studied systems of similar substrate bulk structure.

With the introduction of the autocorrelation autoregression (ACAR) and autocorrelation eigenvector (ACE) techniques in the spectral analysis, the ARPEFS-FT analysis has become more powerful. The ACAR or ACE approach improves the real-space resolution and helps identify the true PLD peaks by suppressing the sidelobes. Except in some occasions when a FT peak is split into two components by the generalized Ramsauer-Townsend (GRT) effect, we can now interpret ARPEFS-FTs in a more quantitative fashion.

Inspired by the work of Szöke, FT analysis has more recently been applied to obtain the real-space atomic images of sample surfaces from two-dimensional angle-scan photoelectron diffraction data [31 - 40]. This photoelectron holography method can

directly determine the adsorption site geometry with some confidence. Recently, three-dimensional data sets have also been taken, with the electron wavevector being the third dimension, to suppress the twin images.

Based on the finding that the positions of strong peaks in the ARPEFS-FTs of experimental data from adsorbed surfaces can be predicted with good accuracy based on the geometry alone, by using the SSC model together with the concept of strong backscattering from atoms located within a cone around 180° from the emission direction, we propose a method here which is much simpler than holography, for determining the local structures of adsorbed surfaces simply from ARPEFS-FTs. This FT method can easily be used to determine the adsorption sites of adsorbates and the bond lengths to the nearby atoms around adsorbates with an accuracy of about ±0.1-0.2Å, using a combination of all the strong peaks from a single ARPEFS-FT spectrum. The accuracy can subsequently be improved by fitting the $\chi(k)$ data with MSSW theory.

II. THE PHYSICAL BASIS OF THE FT METHOD

The positions of the strong peaks in the ARPEFS-FTs of experimental data from adsorbed surfaces can be predicted by using the SSC model that utilizes the well-known strong backscattering by atoms located within a cone around 180° from the emission direction [41 - 43]. This characteristic of ARPEFS-FTs is determined mainly by the trend of the electron-atom scattering factor in the ARPEFS energy range, where the electron-atom scattering is largely dominated by the backward and forward scattering. In this section, we shall examine this finding in detail, with both experimental off-normal and

normal-emission ARPEFS data from five previously studied adsorbed surfaces: c(2×2)S/Ni(001), p(2×2)S/Cu(001), c(2×2)Cl/Cu(001), c(2×2)P/Fe(001), and c(2×2)S/Cr(001).

A Off-normal emission

Using the 1s core levels of the adsorbates, the experiments measured off-normal emission ARPEFS data along or nearly along the [011] direction with the photon polarization vector essentially collinear with the emission direction, and measured normal emission data along the surface normal with the photon polarization vector oriented 30-35° away from the surface normal toward the [011] direction. The two Cu surfaces were held at a temperature of 110K while the Ni, Cr and Fe surfaces were held at the ambient temperature of about 300K. All the experimental off-normal and normal emission ARPEFS data were Fourier transformed based on the ACAR or ACE algorithm. The single-scattering path length differences (SS-PLDs) were calculated according to the formula:

$$PLDj = Rj - Rj\cos\theta j,$$

where R_j is the bond length of a scattering atom j, and θ is the scattering angle of the photoelectron. In the following, we shall show respectively the results of the examinations on the off-normal and normal emission ARPEFS-FTs.

Figs. 1-5 illustrate respectively the results of the examinations on the off-normal emission ARPEFS-FTs for c(2×2)S/Ni(001) [14], p(2×2)S/Cu(001) [25], c(2×2)Cl/Cu(001) [23],

c(2×2)P/Fe(001) [21], and c(2×2)S/Cr(001) [18]. The SS-PLDs for each adsorbed surface were calculated using the structural parameters from previous ARPEFS studies, as listed in Table 3. Table 1 summarizes the results of the examinations for the five adsorbed surfaces, in which the positions of all the strong FT peaks of the experimental off-normal emission ARPEFS data are compared with the calculated SS-PLDs up to 15.0Å. The agreement is remarkable: always within about ±0.5Å, with an rms deviation of 0.2Å for all the strong peaks. The 5.2Å peak in Fig. 1 is unlisted in Table 1, while it can be accounted by the scatterer labeled 2*. The 2* scatterer is located 3.14Å directly beneath the S emitter, resulting in a geometric SS-PLD of 5.4Å.

B Normal emission

The analyses on the normal emission ARPEFS-FTs are not so simple as in the above off-normal case because of the GRT effect. In normal emission ARPEFS-FTs, it becomes serious sometimes as it can induce peak splitting. This will affect the FT method.

The GRT effect is the accidental vanishing of the electron-atom scattering factor at some special angles and energies. When the GRT effect occurs, because the scattering factor goes through zero in the complex plane, we encounter a zero in the magnitude and a jump in the phase of the scattering factor, and there appears to be a resonance in the oscillating ARPEFS χ curve. The top panel of Fig.6 shows the GRT resonance in the experimental normal emission ARPEFS data of c(2×2)S/Ni(001). The bottom panel shows the FT of the experimental normal emission ARPEFS data of c(2×2)S/Ni(001), which was obtained

using the ACAR method. In the ARPEFS-FTs, the first two peaks at 2.5Å and 4.3Å do not correspond to real PLDs, instead, they manifest the GRT-induced peak-splitting of a peak at about 3.5Å, which corresponds to the PLD of the four nearest Ni atoms around the S atom.

Figs.7-11 illustrate respectively the results of our analysis of the normal emission ARPEFS-FTs for c(2×2)S/Ni(001) [14], p(2×2)S/Cu(001) [25], c(2×2)Cl/Cu(001) [23], c(2×2)P/Fe(001) [21], and c(2×2)S/Cr(001) [18], using ACAR or ACE. The SS-PLDs for each adsorbed surface were calculated using the structural parameters from previous ARPEFS studies. Table 2 summarizes the results of our analysis for the five adsorbed surfaces, in which the positions of all the strong peaks in the ARPEFS-FTs of the experimental normal emission data are compared with the calculated SS-PLDs up to 15.0Å. The geometric parameters in Table 3 are used for calculating the SS-PLDs in Table 2. The agreement is very good: always within about ±0.5Å, with an rms deviation of 0.2Å for all the strong peaks. The 8.5Å peak in Fig. 9 is unlisted in Table 2, while it can be accounted for by the scatterer labeled 2* with a geometric SS-PLD of 8.4Å. The contribution from the 2* atom is enhanced by another Cu atom which is almost collinear with the Cl emitter and the 2* atom. The other four cases do not involve this accidental forward focusing geometry.

III. THE PROCEDURE OF APPYING THE FT METHOD

Based on the above finding, we propose the FT method for determining the local structure of adsorbed surfaces simply from ARPEFS-FTs. For an adsorbed surface, one

first measures its ARPEFS data along the surface normal or off normal and then obtains its ARPEFS-FTs using the ACAR technique. Starting from the ARPEFS-FT, one first assumes that the adsorbate-induced substrate relaxation is small, and calculates the SS-PLDs for the nearest atoms and atoms located within a backscattering cone aligned along the emission direction for all the plausible adsorption sites on the unreconstructed substrate, if necessary varying the parameters through plausible ranges of adsorbate-substrate interlayer spacing. Typically, only one site will give ARPEFS-FT peak positions that agree even qualitatively with experiment. If two or more are close, a second ARPEFS-FT in another direction may be needed. If none fit, reconstructed surfaces should next be considered, and the algorithm is repeated. After the adsorption site is determined, the local structure around the adsorbate atom can then be refined by adjusting the interlayer spacing between the adsorbate layer and the first substrate layer to achieve good agreement between calculated and experimental positions of all the strong peaks in the ARPEFS-FT. The agreement can be quantified by the positional R-factor defined as

$$R = \sum_j \left(Pc[j] - Pe[j]\right)^2,$$

where P_c and P_e designate respectively the calculated and the experimental positions of strong peaks in the ARPEFS-FT. This approach will yield a reasonably accurate structure quickly. A full multiple-scattering spherical-wave (MSSW) fit of the ARPEFS data or its FT is still required to obtain a very high accuracy fit that considers subtle lattice reconstruction, etc.

To illustrate this method, we take p(2×2)S/Cu(001) as an example. Fig.2 shows that there are six strong peaks, at 3.2Å, 4.3Å, 7.6Å, 9.5Å, 12.2Å and 14.6Å in the off-normal emission ARPEFS-FT of p(2×2)S/Cu(001). For symmetry reasons, there are three plausible adsorption sites for the S adsorbate atom on the Cu(001) surface: the top site, the bridge site, and the fourfold hollow site. Adjusting the S-Cu interlayer spacing for all the three sites to produce a dominant peak at the observed position of 4.3Å, the SS-PLDs for the nearest atoms and atoms located within the backscattering cone aligned along the emission direction were then calculated up to 15.0Å, for the three hypothetical sites. There are six strong peaks at 4.4Å, 6.6Å, 8.6Å, 9.1Å, 11.5Å, and 14.2Å for the atop site, six strong peaks at 3.2Å, 4.4Å, 6.7Å, 9.3Å, 11.7Å, and 14.4Å for the bridge site, and six strong peaks at 3.3Å, 4.4Å, 7.5Å, 9.4Å, 12.4Å, and 14.6Å for the fourfold hollow site. It is obvious by visual inspection that only the fourfold hollow site gives acceptable agreement. Quantitatively, the top site, the bridge site, and the fourfold hollow site give the R-factors or 13.1, 1.1, and 0.1, respectively.

IV. DISCUSSION AND CONCLUSIONS

We have shown that in both the off-normal and normal emission cases, the positions of all the strong peaks in the FTs of ARPEFS data from adsorbed surfaces can be predicted with fairly good accuracy based on geometry alone, by using the SSC model together with the concept of strong backscattering from atoms located within a cone around 180° from the emission direction. We have also found by calculations that the accuracy of the

SSC model in the prediction of the strong peaks in ARPEFS-FTs is largely determined by the effect of the electron-atom scattering factors, often referred to as the phase shifts.

We have shown that the FT method can determine the local structures of absorbed surfaces from both the off-normal and normal emission ARPEFS-FTs with good accuracy. We have also shown that the procedure of applying the FT method is simple. The FT method, however, implicitly rather than explicitly in its algorithm, requires trial-and-error intelligence. The extent to which it can be automated and subsequently turned into a foolproof structural analysis tool remains to be seen. We are optimistic that this is feasible, especially if ARPEFS data from two or three directions are combined.

In summary, we have given a detailed description of the FT method involving both the off-normal and normal emission ARPEFS data.

ACKNOWLEDGEMENTS

This work was supported by the Director, Office of Energy Research, Office of Basic Energy Sciences of the U.S. Department of Energy under Contract No. DE-AC03-76SF00098. The experiments were performed at the Stanford Synchrotron Radiation Laboratory and the Brookhaven National Light Source, which are supported by the U.S. Department of Energy's Office of Basic Energy Sciences.

REFERENCES

1. Liebsch, Phys. Rev. Lett. **32**, 1203 (1974).
2. Liebsch, Phys. Rev. B **13**, 544 (1976).
3. S. Kono, C. S. Fadley, N. F. T. Hall, and Z. Hussain, Phys. Rev. Lett. **41**, 117 (178).
4. P. Woodruff, D. Norman, B.W. Holland, N.V. smith, H. Farrel, and M. M. Traum, Phys. Rev. Lett. **41**, 1130 (1978).
5. S. D. Kevan, D. H. Rosenblatt, D. Denley, B. C. Lu, and D.A. Shirley, Phys. Rev. Lett **41**, 1565 (1978).
6. S. D. Kevan, D.H. Rosenblatt, D. Denley, B. C. Lu, and D.A. Shirley, Phys. Rev. B **20**, 4133 (1979).
7. H. Rosenblatt, J. G. Tobin, M. G. Mason, R. F. Davis, S. D. Kevan, and D. A. Shirley, Phys. Rev. B **23**, 3828 (1981).
8. S. D. Kevan, R.F. Davis, D.H. Rosenblatt, J. G. Tobin, M.G. Mason, D.A. Shirley, C.H. Li, and S.Y. Tong, Phys. Rev. Lett **46**, 1629 (1981).
9. D.H. Rosenblatt, S. D. Kevan, J. G. Tobin, R.F. Davis, M.G. Mason, D. Denley, D.A. Shirley, C.H. Li, and S.Y. Tong, Phys. Rev. B **26**, 1812 (1982).
10. Z. Hussain, D.A. Shirley, C.H. Li, and S.Y. Tong, Proc. Natl. Acad. Sci. USA **78**, 5293 (1981).
11. M. Sagurton, E.L. Bullock, and C.S. Fadley, Phys. Rev. B **30**, 7332 (1984).
12. P.A. Lee, P.H. Citrin, P. Eisenberger, and B.M. Kincaid, Rev. Mod. Phys. **53**, 769 (1981).

13. J.J. Barton, C.C. Bahr, Z. Hussain, S.W. Robey, J.G. Tobin, L.E. Klebanoff, and D.A. Shirley, Phys. Rev. Lett. **51**, 272 (1983).

14. J.J. Barton, C.C. Bahr, S.W. Robey, Z. Hussain, E. Umbach, and D.A. Shirley, Phys. Rev. B **34**, 3807 (1986).

15. S.W. Robey, J.J. Barton, C.C. Bahr, G. Liu, and D.A. Shirley, Phys. Rev. B **35**, 1108 (1987).

16. C.C. Bahr, J.J. Barton, Z. Hussain, S.W. Robey, J.G. Tobin, and D.A. Shirley, Phys. Rev. B **35**, 3773 (1987).

17. S.W. Robey, C.C. Bahr, Z. Hussain, J.J. Barton, K.T. Leung, and D.A. Shirley, Phys. Rev. B **35**, 5657 (1987).

18. L.J. Terminello, X.S. Zhang, Z.Q. Huang, S. Kim, A.E. Schach von Wittenau, K.T. Leung, and D.A. Shirley, Phys. Rev. B **38**, 3879 (1988).

19. K.T. Leung, L.J. Terminello, Z. Hussain, X.S. Zhang, T. Hayashi, and D.A. Shirley, Phys. Rev. B **38**, 8241 (1988).

20. X.S. Zhang, L.J. Terminello, S. Kim, Z.Q. Huang, A.E. Schach von Wittenau, and D.A. Shirley, J. Chem. Phys. **89**, 6538 (1988).

21. W.R.A. Huff, Y. Chen, X.S. Zhang, L.J. Terminello, F.M. Tao, Y.K. Pan, S.A. Kellar, E.J. Moler, Z. Hussain, H. Wu, Y. Zheng, X. Zhou, A.E. Schach von Wittenau, S. Kim, Z.Q. Huang, Z.Z Yang, and D.A. Shirley, Phys. Rev. B **55** 10830 (1997).

22. L.J. Terminello, K.T. Leung, Z. Hussain, T. Hayashi, X.S. Zhang, and D.A. Shirley, Phys. Rev. B **41**, 12787 (1990).

23. L.Q. Wang, A.E. Schach von Wittenau, Z.G. Ji, L.S. Wang, Z.Q. Huang, and D.A. Shirley, Phys. Rev. B **44**, 1292 (1991).

24. L.Q. Wang, Z. Hussain, Z.Q. Huang, A.E. Schach von Wittenau, D.W. Lindle, and D.A. Shirley, Phys. Rev. B **44**, 13711 (1991).

25. A.E. Schach von Wittenau, Z. Hussain, L.Q. Wang, Z.Q. Huang, Z.G. Ji, and D.A. Shirley, Phys. Rev. B **45**, 13614 (1992).

26. Z.Q. Huang, L.Q. Wang, A.E. Schach von Wittenau, Z. Hussain, and D.A. Shirley, Phys. Rev. B **47**, 13626 (1993).

27. Z.Q. Huang, Z. Hussain, W.R.A. Huff, E.J. Moler, and D.A. Shirley, Phys. Rev. B **48**, 1696 (1993).

28. Y. Zheng, E.J. Moler, E. Hudson, Z. Hussain, and D.A. Shirley, Phys. Rev. B **48**, 4760 (1993).

29. Y. Zheng, and D.A. Shirley, Chem. Phys. Lett. **203**, 114 (1993).

30. Y. Zheng, Z. Hussain, and D.A. Shirley, Chem. Phys. Lett. **206**, 161 (1993).

31. Szöke, in *Short Wavelength Coherent Radiation: Generation and Application*, edited by D.T. Attwood and J. Boker, AIP Conf. Proc. No. 147 (American Institute of Physics, New York, 1986).

32. J.J. Barton, Phys. Rev. Lett. **61**, 1356 (1988).

33. C.M. Wei, T.C. Zhao, and S.Y. Tong, Phys. Rev. Lett. **65**, 2278 (1990).

34. G.R. Harp, D.K. Saldin, and B.P. Tonner, Phys. Rev. B **42**, 9199 (1990).

35. S. Thevuthasan, G.S. Herman, A.P. Kaduwela, R.S. Saiki, Y.J. Kim, W. Niemczura, M. Burger, and C.S. Fadley, Phys. Rev. Lett. **70**, 595 (1993).

36. S.Y. Tong, H. Huang, and C.M. Wei, Phys. Rev. B **46**, 2452 (1992).

37. Fritzsche and D.P. Woodruff, Phys. Rev. B **46**, 16128 (1992).

38. J.G. Tobin, G.D. Waddill, H. Li, and S.Y. Tong, Phys. Rev. Lett. **70**, 4150 (1993).

39. H. Wu, G.J. Lapeyre, H. Huang, and S.Y. Tong, Phys. Rev. Lett. **71**, 251 (1993).

40. K.M. Schindle, Ph. Hofmann, V. Fritzsche, S. Bao, S. Kulkarni, A.M. Bradshaw, and D.P. Woodruff, Phys. Rev. Lett. **71**, 2054 (1993).

41. J.J. Barton, Ph.D. thesis, University of California, Berkeley, 1985.

42. J.J. Barton and D.A. Shirley, Phys. Rev. B **35**, 933 (1987).

43. J.J. Barton and D.A. Shirley, Phys. Rev. B **34**, 778 (1986).

Table 5.1 Experimental and calculated PLDs in the off-normal emission ARPEFS-FTs.

Surface systems		P_1(Å)	P_2(Å)	P_3(Å)	P_4(Å)	P_5(Å)	P_6(Å)
c(2×2)S/Ni(001)	exp	3.0	4.1	7.2	9.0	13.0	14.7
	cal	3.1	4.4	7.5	9.4	12.2	14.4
p(2×2)S/Cu(001)	exp	3.2	4.3	7.6	9.5	12.2	14.6
	cal	3.3	4.4	7.5	9.4	12.4	14.6
c(2×2)Cl/Cu(001)	exp	3.2	4.9	7.2	10.3	13.7	
	cal	3.6	4.8	8.0	9.9	12.9	
c(2×2)P/Fe(001)	exp	3.6	7.8	11.9	15.5		
	cal	4.0	7.6	11.8	15.7		
c(2×2)S/Cr(001)	exp	4.0	7.7	12.4	15.8		
	cal	4.2	7.5	11.9	15.8		

Table 5.2 Experimental and calculated PLDs in the normal emission ARPEFS-FTs

Surface systems		P_1(Å)	P_2(Å)	P_3(Å)	P_4(Å)	P_5(Å)
c(2×2)S/Ni(001)	exp	3.8	6.5	9.9	13.8	16.8
	cal	3.5	6.3	10.1	13.3	17.0
p(2×2)S/Cu(001)	exp	3.9	6.4	10.2	13.0	16.2
	cal	3.6	6.4	10.1	13.3	17.2
c(2×2)Cl/Cu(001)	exp	3.9	7.0	10.4	14.5	
	cal	4.0	6.9	10.7	14.0	
c(2×2)P/Fe(001)	exp	3.2	4.8	8.3	11.1	14.0
	cal	3.3	4.9	8.3	10.6	13.8
c(2×2)S/Cr(001)	exp	3.7	4.8	8.6	10.7	
	cal	3.5	5.0	8.4	10.8	

Table 5.3 Interplanar distances between the adsorbate layer and the substrate layers

Surface systems	Lattice constant of the substrate crystal	d_1(Å)	d_2(Å)	d_3(Å)	d_4(Å)	d_5(Å)
c(2×2)S/Ni(001)	3.52 Å, fcc	1.31	3.14	4.90	6.66	8.42
p(2×2)S/Cu(001)	3.615 Å, fcc	1.32	3.18	4.90	6.70	8.51
c(2×2)Cl/Cu(001)	3.615 Å, fcc	1.604	3.432	5.222	7.023	8.833
c(2×2)P/Fe(001)	2.866 Å, bcc	1.02	2.45	3.88	5.32	6.75
c(2×2)S/Cr(001)	2.91 Å, bcc	1.17	2.48	3.93	5.39	6.84

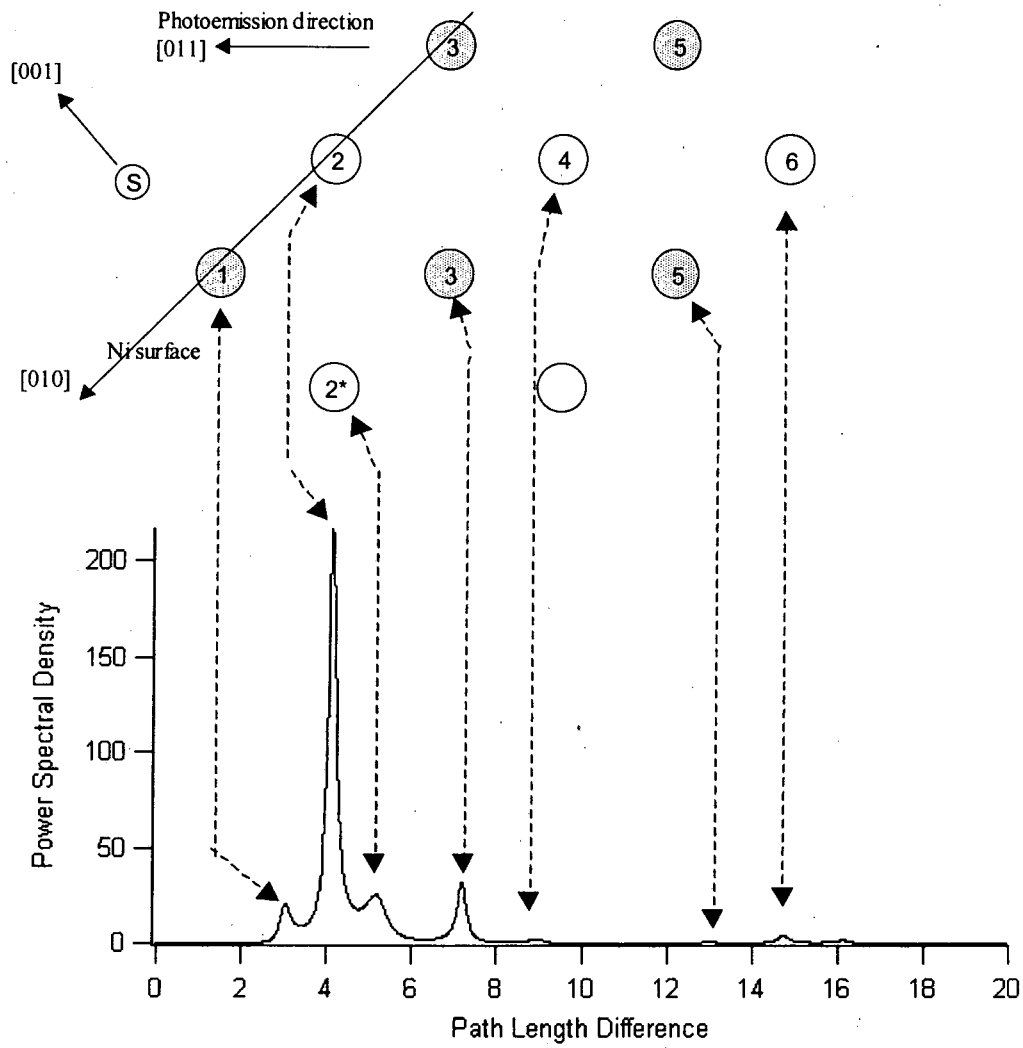

FIG. 5.1 c(2×2)S/Ni(001) off-normal emission ARPEFS-FT.

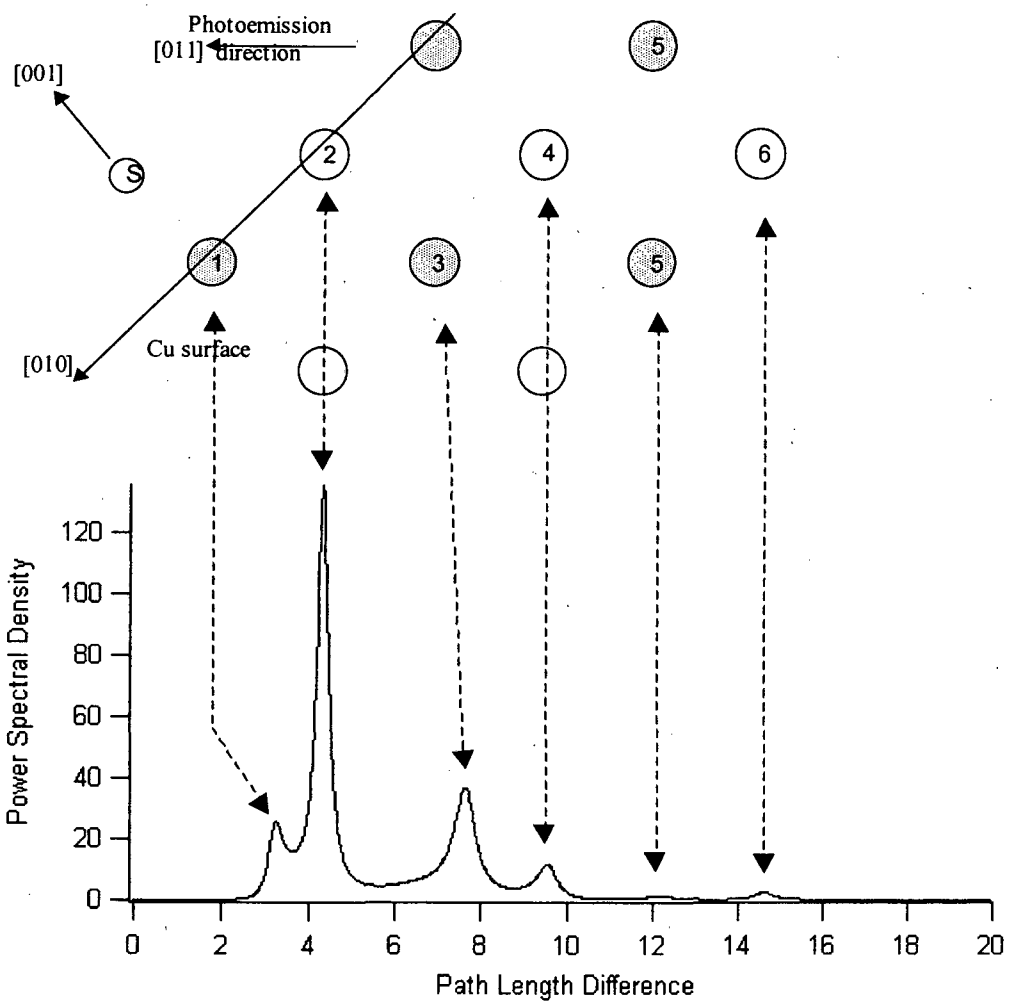

FIG. 5.2 p(2×2)S/Cu(001) off-normal emission ARPEFS-FT.

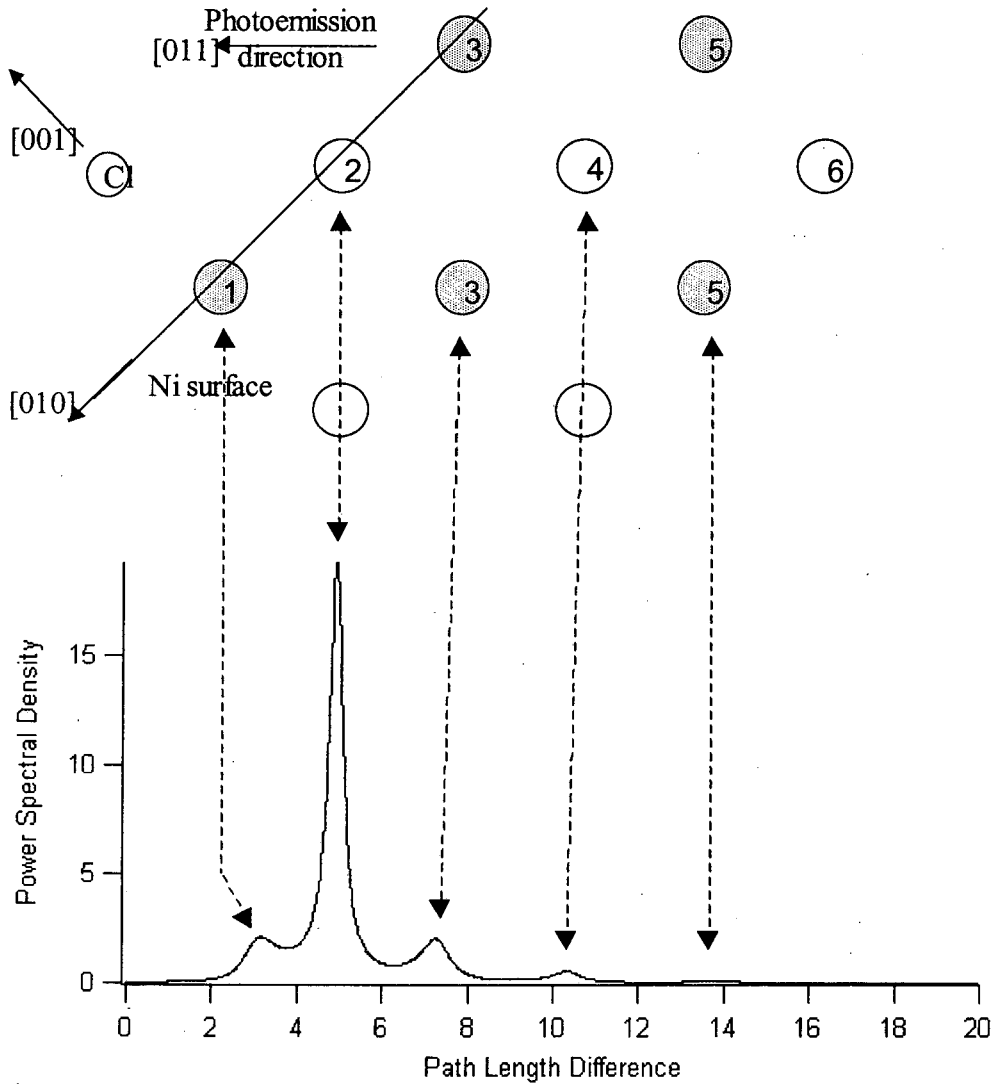

FIG. 5.3 c(2×2)Cl/Cu(001) off-normal emission ARPEFS-FT.

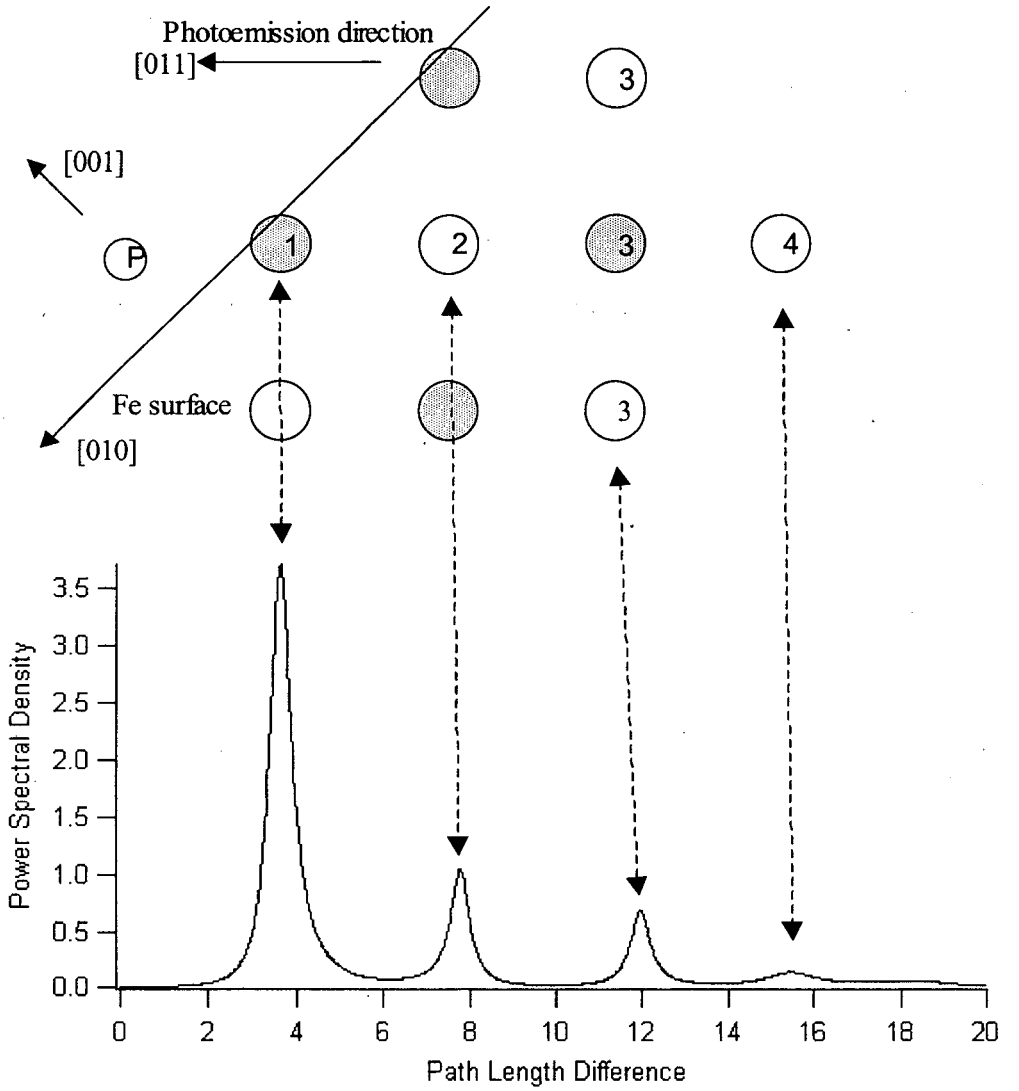

FIG. 5.4 c(2×2)P/Fe(001) off-normal emission ARPEFS-FT.

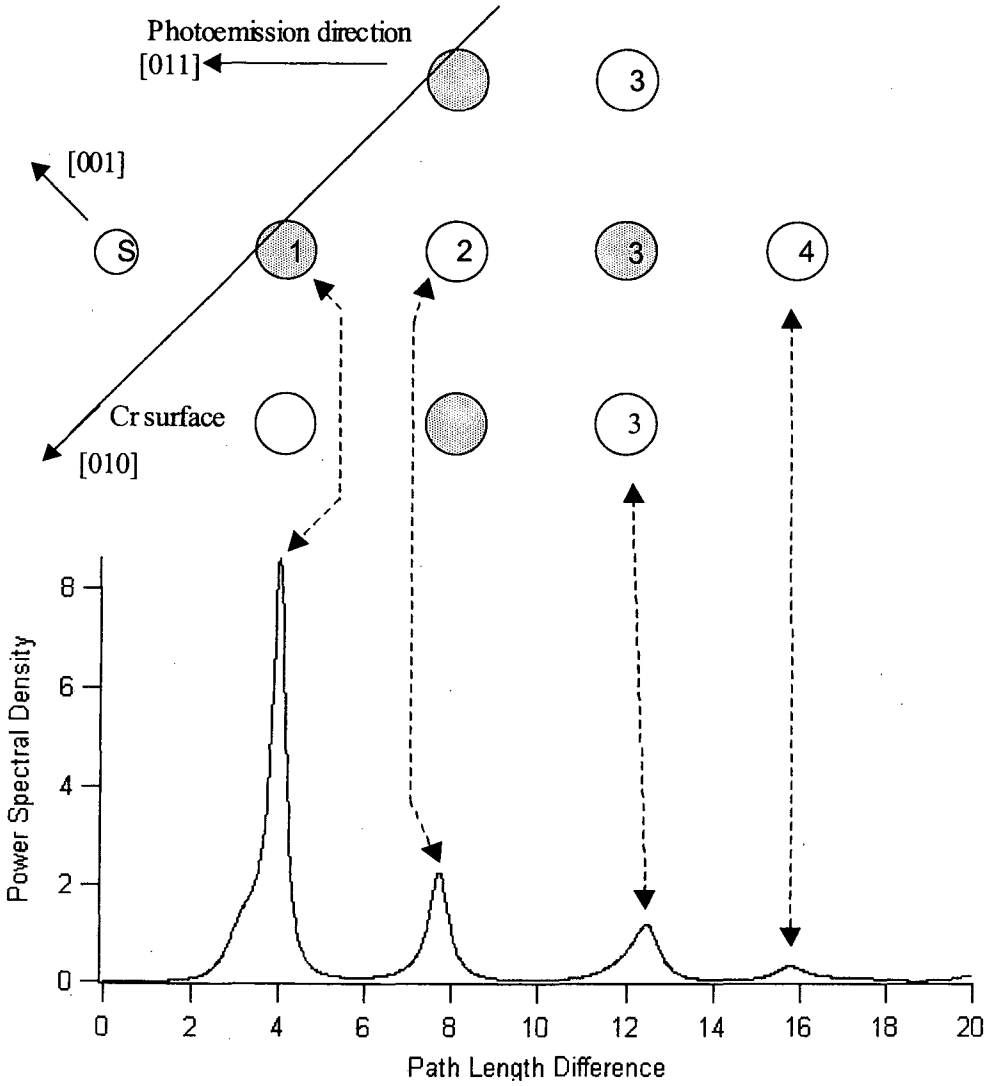

FIG. 5.5 c(2×2)S/Cr(001) off-normal emission ARPEFS-FT.

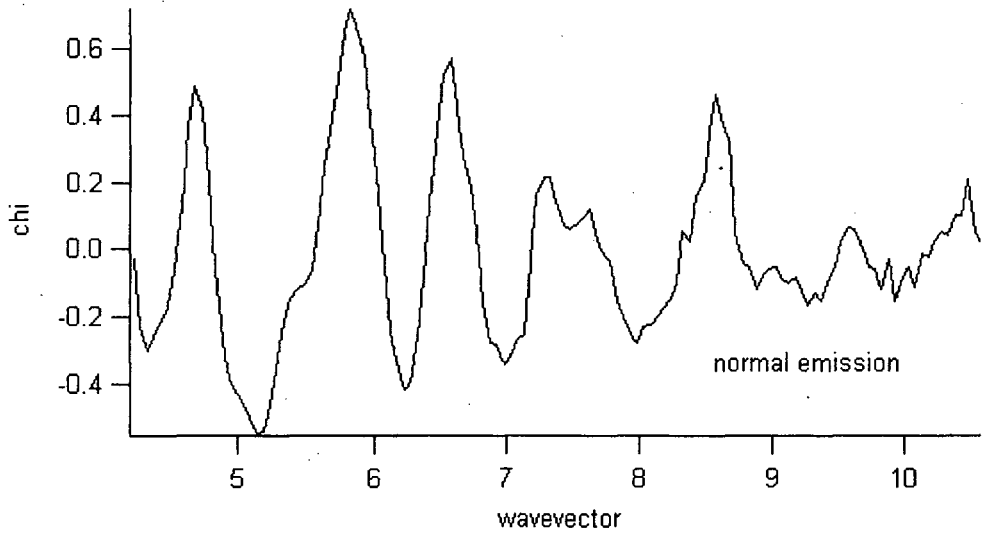

FIG. 5.6 Normal emission ARPEFS of c(2×2)S/Ni(001).

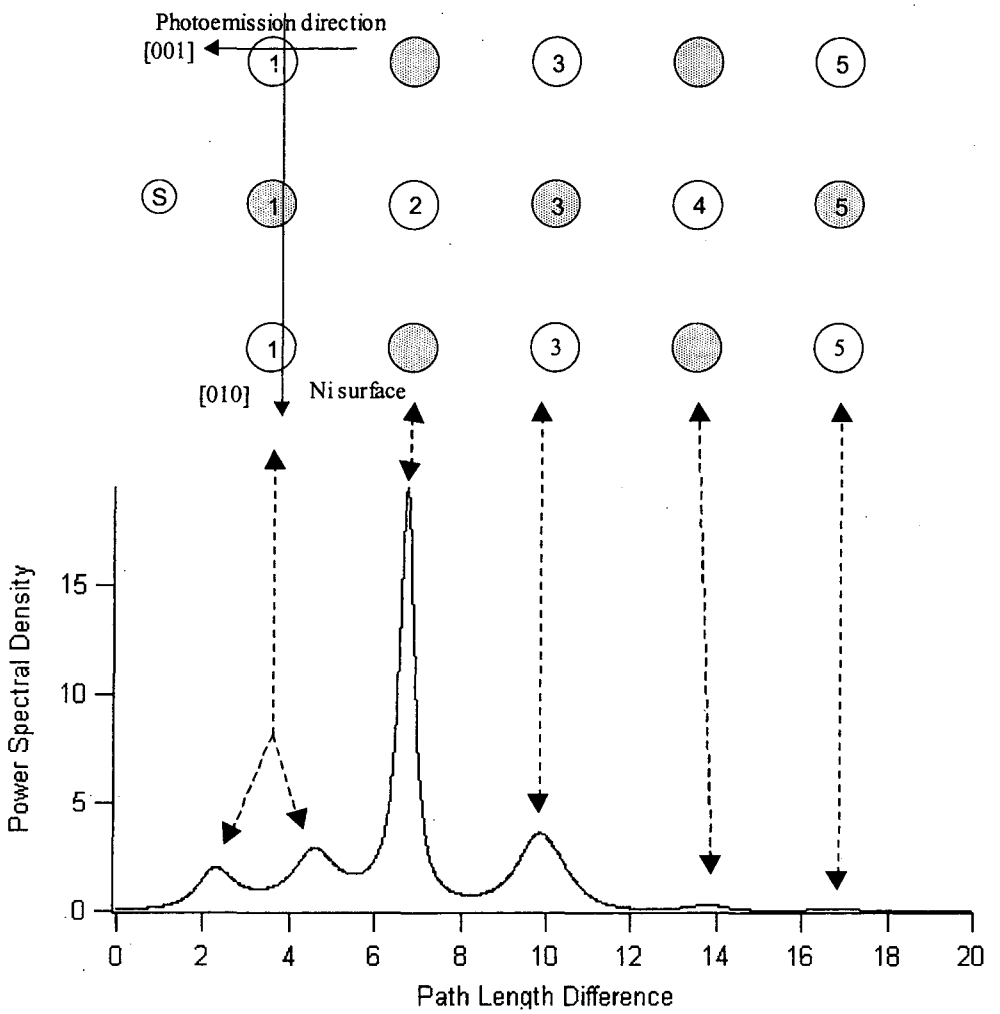

FIG. 5.7 c(2×2)S/Ni(001) normal emission ARPEFS-FT.

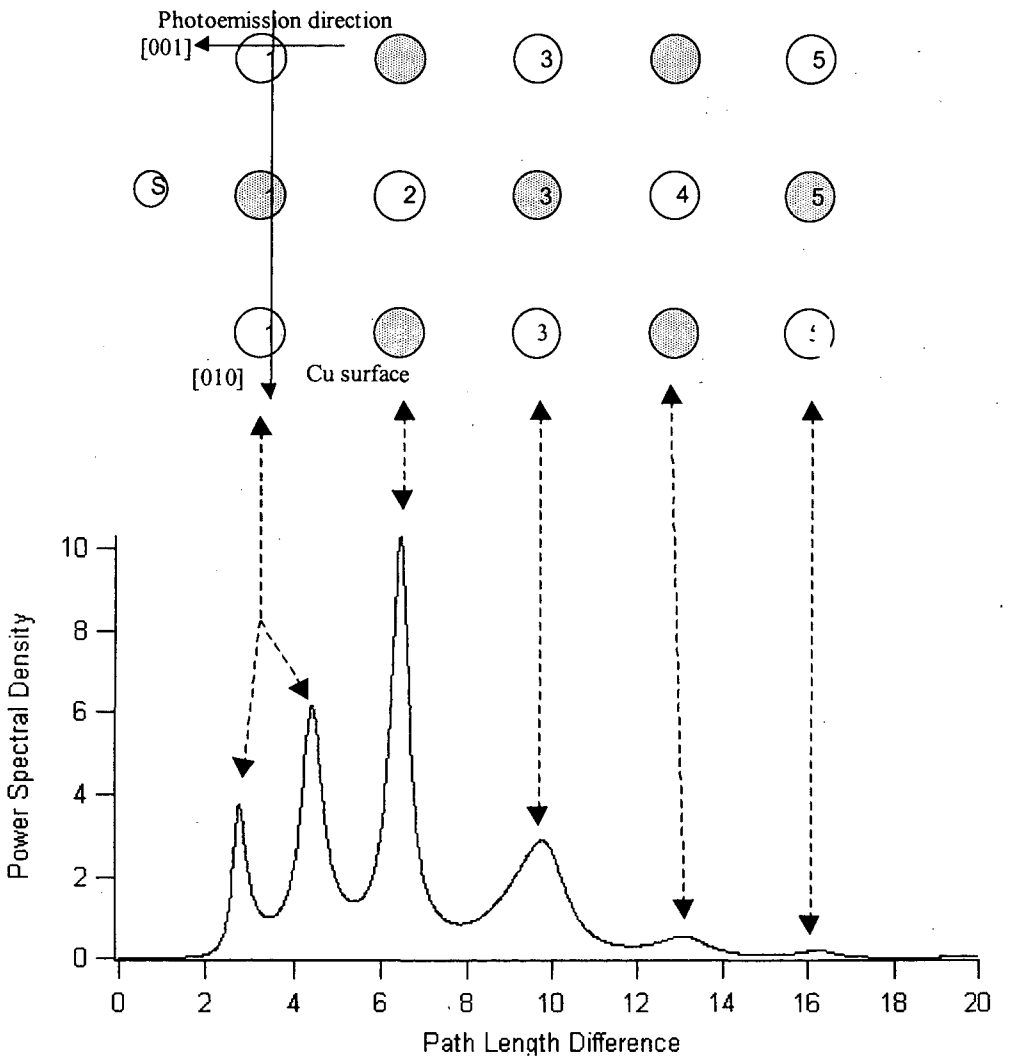

FIG. 5.8 p(2×2)S/Cu(001) normal emission ARPEFS-FT.

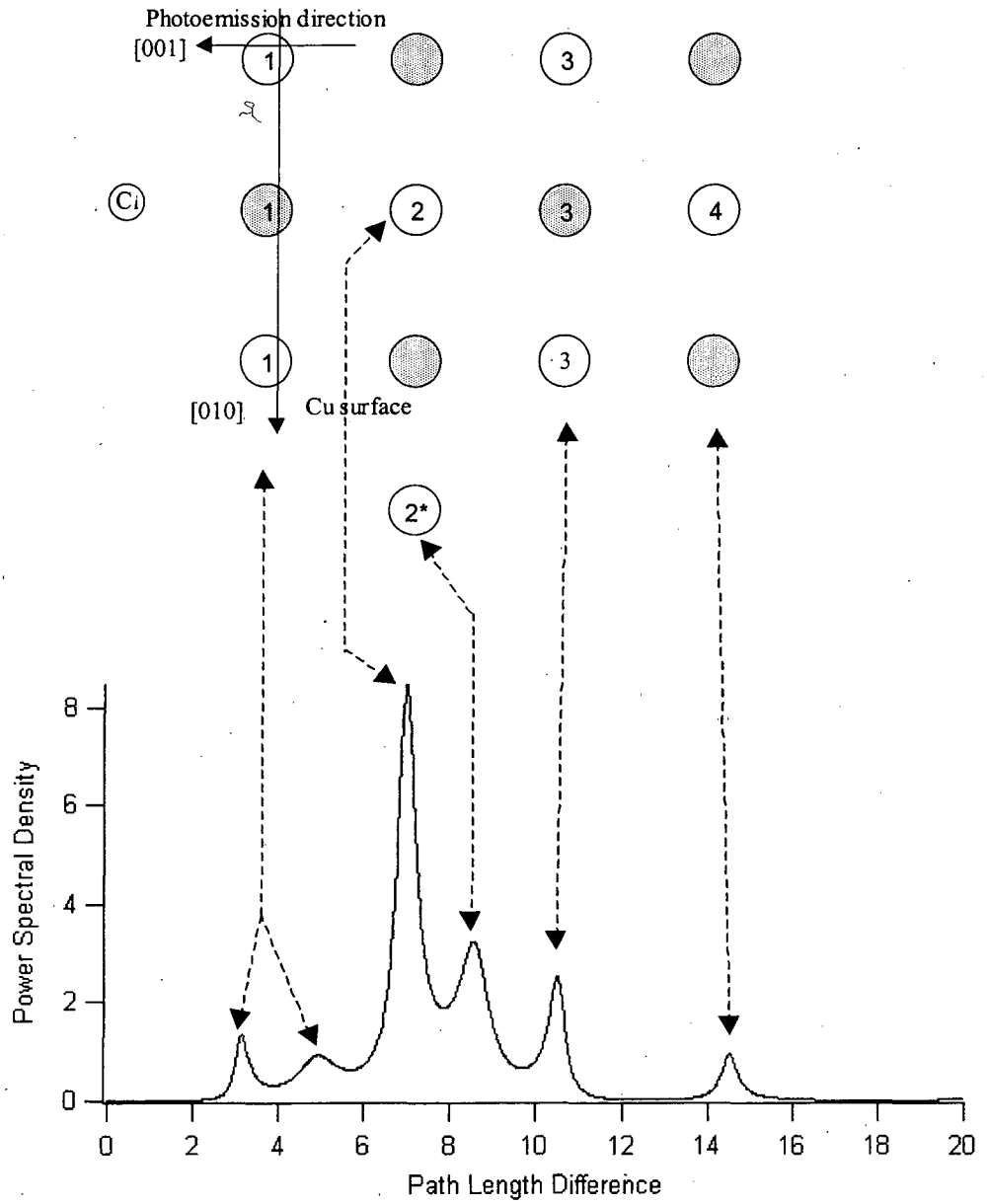

FIG. 5.9 c(2×2)Cl/Cu(001) normal emission ARPEFS-FT.

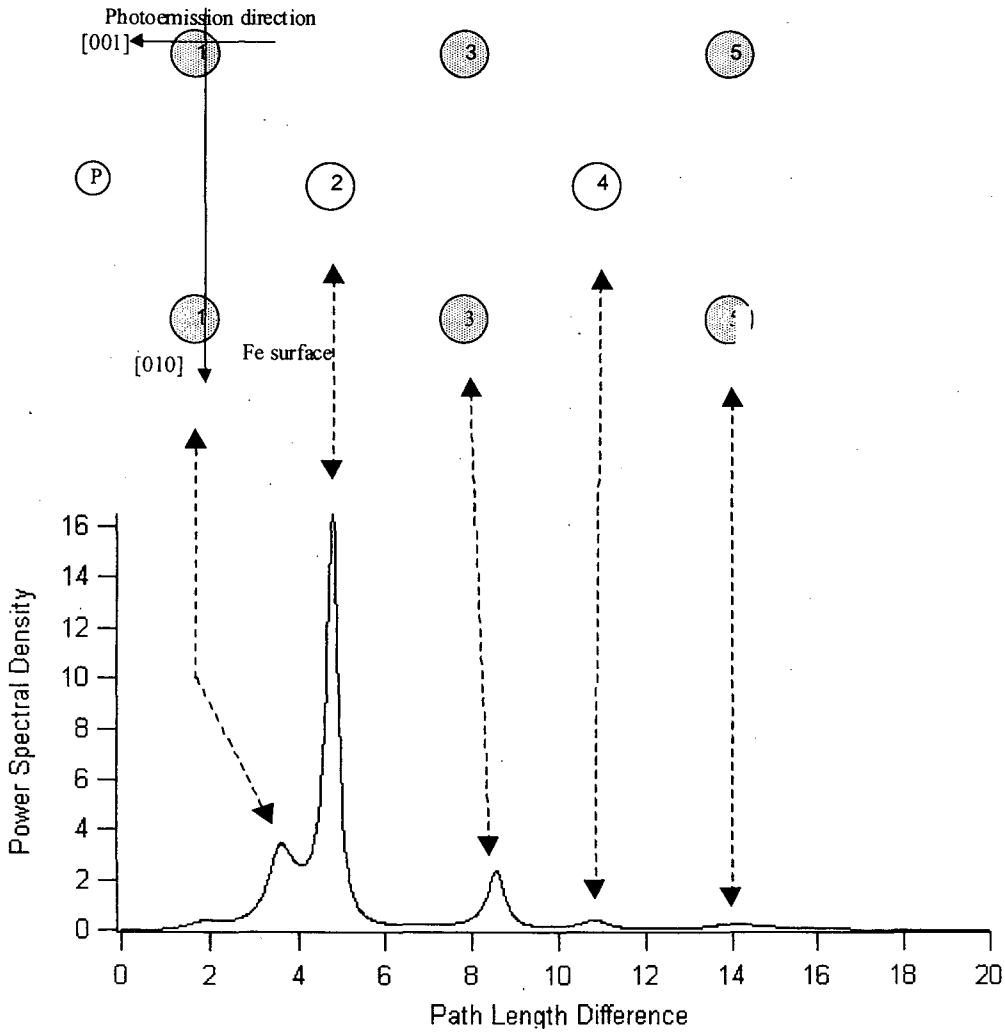

FIG. 5.10 c(2×2)P/Fe(001) normal emission ARPEFS-FT.

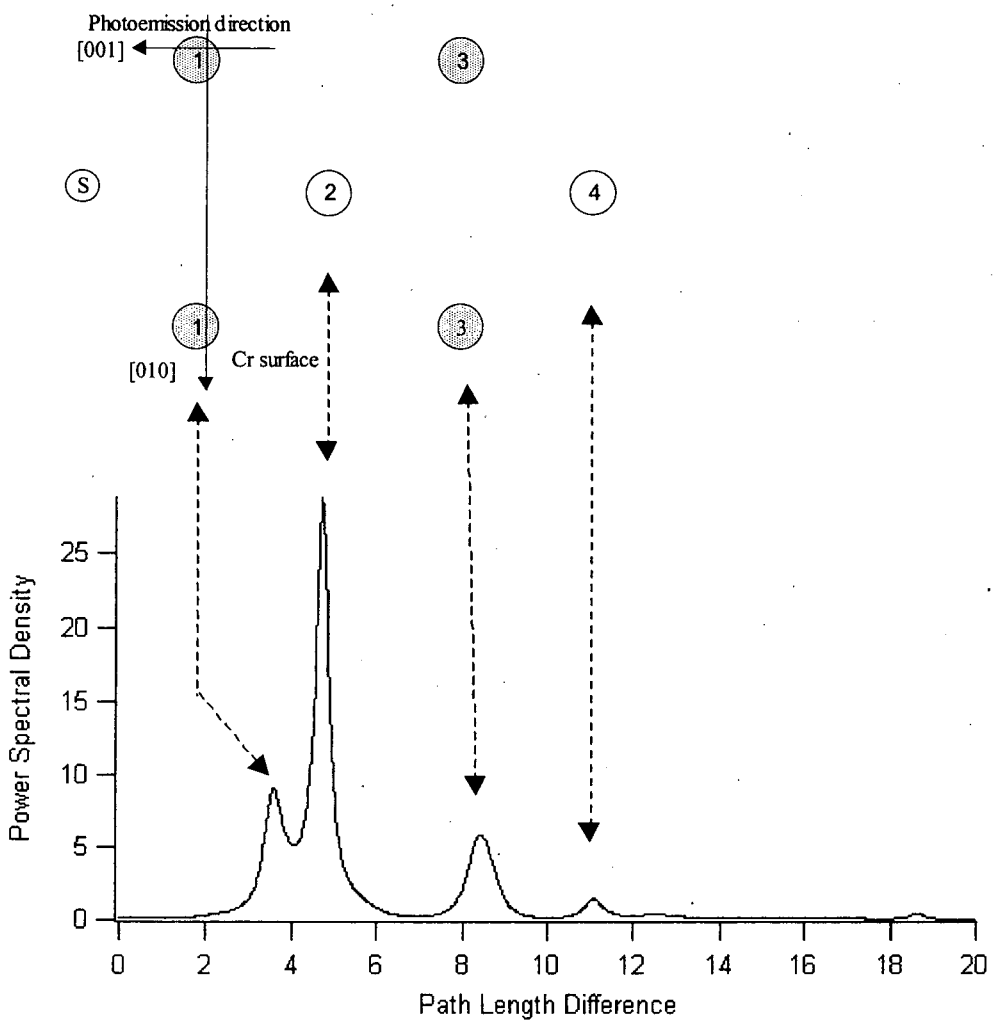

FIG. 5.11 c(2×2)S/Cr(001) normal emission ARPEFS-FT.

Chapter 6. Conclusions

I have applied photoelectron diffraction, in the form of angle-resolved photoemission extended fine structure (ARPEFS) in new ways to several surface systems, with emphasis on Fourier transform analysis. I have introduced and implemented several parameterized FT methods, most notably ACAR and ACE, which enable the detailed and credible interpretation of the power spectra of ARPEFS χ curves.

Very few techniques exist for studying the surface chemical bond. CO adsorbed on Pt(111) surface was studied as an example showing how photoelectron diffraction can be a direct probe. I have measured the photoemission peaks from the molecular orbitals over a wide photon energy range and have analyzed the data in the same fashion as we usually treat the χ curve from a core level. The C 1s ARPEFS data were used to determine the CO adsorption geometry as half top, half bridge-site adsorption, with C-Pt interplanar distances of 1.83Å on the top site and 1.45Å on the bridge site. The C 1s χ curve was Fourier transformed to compare with the ARPEFS-FTs of the MOs to reveal differences in the effective mean value of the electron density distribution along the Pt-C-O direction. The 4σ MO was found to be concentrated between the C and O atoms and the 5σ MO between the C atom and the Pt surface, consistent with the Blyholder chemisorption model. This opens the possibility of using ARPEFS to distinguish chemisorption from physisorption, since the two bonding mechanisms would have given different electron density distributions.

By studying the clean Ni(111) surface, I have shed light on the dilemma that multiple scattering is needed to correctly model a χ curve, while single scattering is sufficient for understanding the off-normal emission ARPEFS-FTs. The key is symmetry, as in the case of normal emission the path length differences (PLD) from single-scattering and multiple-scattering events have a lot more chances to be equal or close to each other, while in the lower symmetry off-normal case this degeneracy is lifted. Two different scattering events that have similar PLDs can cancel each other or enhance that particular FT peak depending on the details in the scattering factor. In the normal-emission case, many different combinations of scattering events have the same PLD, and this compensates the weak contribution from each path. When modeling the Ni normal emission ARPEFS curves, I have found that up to third-order multiple scattering is needed to capture all the major features in the FT spectra. In the off-normal emission case, different scattering paths usually have different PLDs. Higher multiple-scattering orders involving no forward scattering contribute much smaller intensities for two reasons: the small scattering factor is multiplied more times, and the total path length is bigger by at least one nearest neighbor distance. Hence single scattering events explain well the positions of strong peaks in the FT, and multiple scattering events modify their strength, and sometimes produce small peaks themselves in the normal emission case.

To improve the spectral resolution in the ARPEFS-FT analysis, I have introduced new spectral analysis methods. Previously autoregression linear prediction (ARLP) was used in our group to sharpen the FT peaks, but it is a very unstable technique. A slight change in the autoregressive order, or in the number of singular values in the data matrix, can

produce a huge change in the outcome of the FT. With autocorrelation autoregression (ACAR) and autocorrelation eigenvector (ACE), we can produce a reliable power spectrum by following the order-closing procedure. The use of autocorrelation as the first step reduces the influence of rogue data points. The parameterized approach eliminates the sidelobes entailed by the window function in direct "taper-and-transform" FT methods. The best spectra are usually obtained when the autocorrelation sequence is computed with lags near half the data points.

I have applied the new FT technique to ten ARPEFS data sets and proposed a simple way of determining surface adsorption sites. First I use a single scattering cluster for possible adsorption sites to construct the geometrical PLDs from the strong backscattering events, and then I compare these PLDs with those obtained from the ARPEFS-FT analysis of the experimental data. Once the preferred adsorption site is determined, I can fine tune the interlayer distances according to the positional R-factor. This method is far simpler than the purportedly direct visualization by photoelectron holography. However, in the normal emission situation, the ARPEFS-FT spectra could be complicated by the generalized Ramsauer-Townsend (GRT) effect, and detailed knowledge of the scattering factor is needed to understand the FT features.

From the experience that I have gained during collecting and analyzing ARPEFS data, I think that a single good monochromator grating with a suitable wide photon energy range is most helpful for a successful photoelectron diffraction experiment. Connecting data segments from two gratings is a nightmare that I would always like to avoid. The current grating technology that produces good soft x-ray dispersion in a medium energy range is

actually compatible with the current theory. The state-of-the-art theory for simulating photoelectron diffraction is based on electron multiple scattering by a muffin-tin potential lattice. The theory would fail beyond the medium range of the electron wavevector k, approximately 3-15$Å^{-1}$. The problem lies with the partial wave formalism of the scattering factor. The expansion diverges for small k values and the number of non-zero partial waves diverges for large k values. Hence within this framework one could only improve the ARPEFS experiment by taking denser data points. However, the Nyquist theorem sets a limit on how many data points are actually needed to fully determine a sinusoidal signal before extra data become redundant. My experience suggests that 0.05$Å^{-1}$ to 0.1$Å^{-1}$ is the suitable step size in k, also because the reasonable duration in time of taking data is limited by the sample lifetime and the synchrotron beam time allocation with today's technology. Further advancement in the energy-scan photoelectron diffraction theory must overcome the aforementioned limits and expand into new subject matter. For example, new theory must be able to treat valence electrons in solids and molecular orbitals in adsorbate systems. I have tried to use the currently available core level photoelectron diffraction theory to model the ARPEFS of MO in a LCAO scheme, but a breakthrough would come if the theory could model the MO directly.

Appendix A. Applied Materials Chamber

On the bending magnet beamline 9.3.2 [1] at the ALS is installed an ultrahigh vacuum Applied Materials Chamber (AMC) designed for Angle-Resolved X-ray Photoemission Spectroscopy and X-ray Absorption Spectroscopy, coupled with the circularly polarized light capability of the beamline. Since its commissioning, many outside users [2,3,4] and Berkeley Lab scientists [5] have come to utilize this system's unique versatility to achieve their diverse scientific goals.

The Applied Materials Chamber (AMC) as shown in Fig. 1 is equipped with a Physical Electronics, Inc. (PHI) Spherical Capacitor Electron Energy Analyzer with an angle-resolving Omni V lens system, variable apertures, a high-speed 16-element multi-channel detector and a high-resolution power supply. The 5-degrees-of-freedom (X, Y, Z, continuous θ and continuous ϕ) sample movements are facilitated by a state-of-the-art manipulator, which is able to cool the sample surface to 110K by liquid nitrogen and easily heat it up to well over 2000K by electron bombardment. The chamber also has a PHI dual-anode X-ray tube for off-line XPS work, a reverse-view linear-travel LEED system for sample characterization, a PHI ion gun for sample cleaning, an Omicron Evaporator and Quartz Crystal micro Balance (QCB) for sample preparation. For absorption type experiments, we have an angle-integrated electron Partial Yield Detector (PYD) and a shielded-wire sample current collector. Recently, we have installed a differentially pumped sample transfer stage that can move samples from atmosphere into

UHV on a short notice. Users routinely reconfigure some ports on the chamber to suit their different needs, e.g. add cleavers or scrapers for studies of high-Tc samples.

REFERENCES

1. Z. Hussain, W.R.A. Huff, S.A. Kellar, E.J. Moler, P.A. Heimann, W. McKinney, H.A. Padmore, C.S. Fadley, and D.A. Shirley, J. Elec. Spec. and Rel. Phen. **80**, 401 (1996).
2. F. Gozzo, A. Cossy-Favre, B. Triplett, H. Fujimoto, and H.A. Padmore, ALS Compendium 1993-1996, 107, (1997).
3. T. Saitoh, P.M.Villella, D.S. Dessau, Y. Moritomo, Y. Tokura, X. Zhou, E.J. Moler, and Z. Hussain, ALS Compendium 1993-1996, 406 (1997).
4. M.A. Brewer, H.L. Ju, K.M. Krishnan, A.T. Young, V. Martynov, E.J. Moler, X. Zhou, S.A. Kellar, and Z. Hussain, ALS Compendium 1993-1996, 409 (1997).
5. X. Zhou, E.J. Moler, Y.-F. Chen, Z. Hussain, and D.A. Shirley, ALS Compendium 1997, ALS Compendium 1997 (1998).

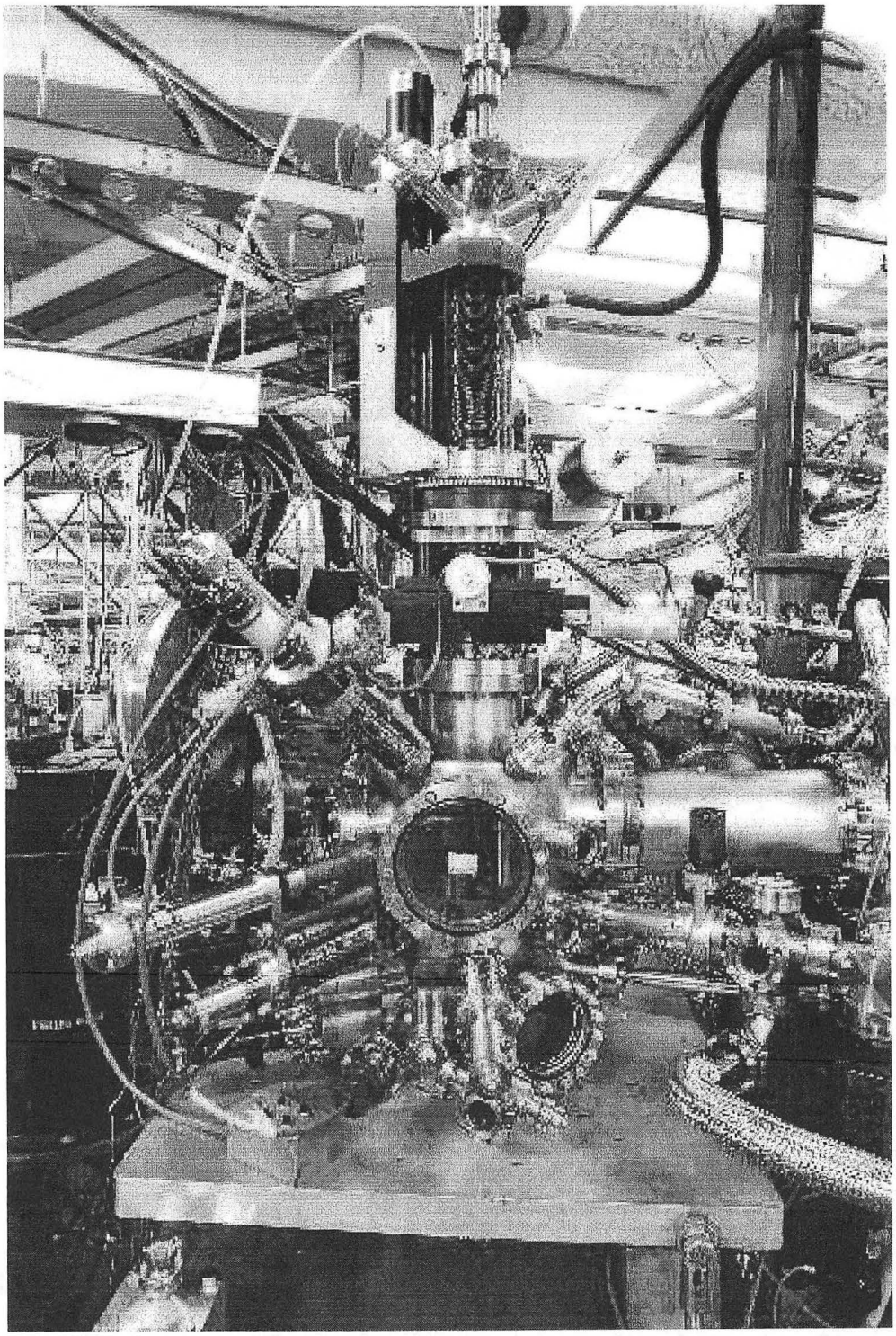

FIG. A.1 Applied Materials Chamber.

Appendix B. Source Code for Calculating the Voigt Function and the Shirley Background

I. INTRODUCTION

This C++ code was compiled on a Windows95 computer with Visual C++ 5.0 to generate a library function that can be conveniently called by other programs, e.g. LabVIEW. The advantage of this code over the more commonly found commercial implementations of the Voigt function is that it approximates Voigt with rational functions, which not only ensure much faster computation, but also enable easy integration. The original C code was written by Prof. A. McLean [1] of Queen's University, Canada. I streamlined it and added the Shirley background capability.

II. VOIGT.H

```
BOOL WINAPI DllMain(HINSTANCE hinstDLL,DWORD,LPVOID);
double voigt(double,double*,double*);
```

III. VOIGT.CPP

```
//Modified from Prof McLean's VS function
//Zhou, Xin
```

```
//LBNL, Dec,1997
#include <windows.h>
#include <math.h>
#include "voigt.h"
BOOL WINAPI DllMain (HANDLE hModule,DWORD dwFunction,LPVOID lpNot){
        return TRUE;
}

double voigt(double x,double* a,double* dyda){
// x is input value, y is output value,
// a[0] is scalar for V(X,Y) = sqrt(Pi)*WG*Voigt(x)
// a[1] is peak position,
// a[2] is Lorentzian width WL in Lorentzian(x) = WL/Pi/(WL^2+x^2) with area = 1
// a[3] is Gaussian width WG in Gaussian(x) = 1/WG/sqrt(Pi)/exp(-x^2/WG^2) with area
= 1
// a[4] is scalar for Shirleyian(x) = Intergrate(Voight) from -infinity to x
// In total, one peak needs 5 parameters

        const double sqrtpi=1.772453851;
        const double start=-50.0;
        double A[4],B[4],C[4],D[4];
        A[0]=-1.2150; B[0]= 1.2359; C[0]=-0.3085; D[0]= 0.0210;
```

```
    A[1]=-1.3509; B[1]= 0.3786; C[1]= 0.5906; D[1]=-1.1858;
    A[2]=-1.2150; B[2]=-1.2359; C[2]=-0.3085; D[2]=-0.0210;
    A[3]=-1.3509; B[3]=-0.3786; C[3]= 0.5906; D[3]= 1.1858;

double X=(x-a[1])/a[3];
    double X0=start/a[3];
double Y=a[2]/a[3];
    double alpha, beta, beta0,YA,XB,X0B;
    double dVdX=0.0,dVdY=0.0,V=0.0,S=0.0,y=0.0,dSdY=0.0;

for(int j=0;j<4;j++)
{
 XB=X-B[j];
      X0B=X0-B[j];
      YA=Y-A[j];
      alpha=C[j]*YA+D[j]*XB;
 beta=pow(YA,2)+pow(XB,2);
      beta0=pow(YA,2)+pow(X0B,2);
 V+=alpha/beta;
      S+=C[j]*atan(XB/YA)-C[j]*atan(X0B/YA)+D[j]*0.5*log(beta/beta0);
 dVdX+=D[j]/beta-2.0*XB*alpha/pow(beta,2);
 dVdY+=C[j]/beta-2.0*YA*alpha/pow(beta,2);
```

```
        dSdY+=(D[j]*YA-C[j]*XB)/beta-(D[j]*YA-C[j]*X0B)/beta0;
    }

    y=a[0]*V+a[4]*S;
    dyda[0]=V;
    dyda[1]=-a[0]*dVdX/a[3]-a[4]*V/a[3];
    dyda[2]=a[0]*dVdY/a[3]+a[4]*dSdY/a[3];
    dyda[3]=dyda[1]*X-dyda[2]*Y;
        dyda[4]=S;
        return y;
}
```

REFERENCES

1 A.B. McLean, C.E.J. Mitchell, D.M. Swanston, J. Elec. Spec. and Rel. Phen. **69**, 125 (1994).

Vita

Xin Zhou

Xin Zhou has been doing surface science research as a senior research associate at the Advanced Light Source in the Ernest Orlando Lawrence Berkeley National Laboratory for the last two years, while he is also a Ph.D. student of Professor David A. Shirley at the Department of Physics in the Pennsylvania State University. From July 1995 to December 1996, he was doing experiments at the Berkeley Lab as a research assistant of PennState. From August 1993 to June 1995, he was a teaching assistant at the University Park campus. In 1991 he received his B.S. in Physics from Fudan University, China, and continued graduate work there for two years before he came to PennState. He is a member of the American Physical Society and the Materials Research Society.

Ernest Orlando Lawrence Berkeley National Laboratory
One Cyclotron Road | Berkeley, California 94720

Prepared for the U.S. Department of Energy under Contract No. DE-AC03-76SF00098